AN ABSTRACT OF THE DISSERTATION OF

Christopher Jones for the degree of Doctor of Philosophy in Physics presented on
June 9, 2017.

Title: Mechanics of Three-Dimensional Microenvironments of Cells

Abstract approved: _____

Bo Sun

The structure and mechanics of tissues affect many important cellular functions
such as migration, differentiation, and growth. Mechanical interactions between
cells and the extracellular matrix (ECM), as well as ECM-mediated mechanical
communication between cells, plays a part in coordinating collective cellular dy-
namics during critical processes such as morphogenesis, tissue regeneration, and
immune response. Mechanical coupling and collective cell migration is particularly
important to the study of cancer progression. Collagen gels are widely used as an
in vitro model for ECM because they mimic the extracellular matrix in physi-
ological conditions. Type I collagen abounds in mammalian extracellular matrix
(ECM) and is crucial to many biophysical processes. We report experimental tech-
niques to study the structure and mechanical properties of collagen-based ECM at
the microscopic scale. We also present computational models that provide insight
into how ECM structure and mechanics depend on environmental factors and cell

activity.

While previous studies have mostly focused on bulk averaged properties, here we provide a comprehensive and quantitative spatial-temporal characterization of the microstructure of type I collagen-based ECM as the gelation temperature varies. The structural characteristics including the density and nematic correlation functions are obtained by analyzing confocal images of collagen gels prepared at a wide range of gelation temperatures. As temperature increases, the gel microstructure varies from a bundled network with strong orientational correlation between the fibers to an isotropic homogeneous network with no significant orientational correlation, as manifested by the decaying of length scales in the correlation functions. We develop a kinetic Monte-Carlo collagen growth model to better understand how ECM microstructure depends on various environmental or kinetic factors. We show that the nucleation rate, growth rate, and an effective hydrodynamic alignment of collagen fibers fully determines the spatiotemporal fluctuations of the density and orientational order of collagen gel microstructure.

Collagen gels are often characterized by their bulk rheology; however, variations in the collagen fiber microstructure and cell adhesion forces cause the mechanical properties to be inhomogeneous at the cellular scale. We study the mechanics of type I collagen on the scale of tens to hundreds of microns by using holographic optical tweezers (HOT) to apply pN forces to microparticles embedded in the collagen fiber network. We find that in response to optical forces particle displacements are inhomogeneous, anisotropic and asymmetric. Gels prepared at 21°C and 37°C show qualitative difference in their micromechanical characteris-

tics. We also demonstrate that contracting cells remodel the micromechanics of their surrounding extracellular matrix in a strain- and distance-dependent manner. To further understand the micromechanics of cellularized extracellular matrix, we have constructed a computational model which reproduces the main experiment findings.

Interactions between cells and the ECM are a dynamic process, in which the cells actively deform and remodel their surroundings. We show that 3D collagen gels are significantly and irreversibly remodeled by cellular traction forces. In addition we find that plasticity of collagen gels can be described in mechanical terms, even when no cells are present. This is shown by irreversible deformation in collagen gels due to macroscopic strain. We present a computational model that describes collagen plasticity in terms of the sliding and merging of ECM fibers. We have confirmed the model predictions agree with experimental results. These results suggest that cell-induced remodeling of the ECM may enhance mechanical coupling between cells and have a dramatic effect on cell-cell communications in 3D fibrous matrices. This could have important implications for the study of tissue development and cancer progression.

Mechanics of Three-Dimensional Microenvironments of Cells

by

Christopher Jones

A DISSERTATION

submitted to

Oregon State University

in partial fulfillment of
the requirements for the
degree of

Doctor of Philosophy

Presented June 9, 2017
Commencement June 2017

Doctor of Philosophy dissertation of Christopher Jones presented on
June 9, 2017.

APPROVED:

_____

Major Professor, representing Physics

_____

Chair of the Department of Physics

_____

Dean of the Graduate School

I understand that my dissertation will become part of the permanent collection
of Oregon State University libraries. My signature below authorizes release of my
dissertation to any reader upon request.

_____

Christopher Jones, Author

TABLE OF CONTENTS

TABLE OF CONTENTS (Continued)

LIST OF FIGURES

LIST OF FIGURES (Continued)

<p align="center">LIST OF FIGURES (Continued)</p>

LIST OF FIGURES (Continued)

Mechanics of Three-Dimensional Microenvironments of Cells

1   Introduction

1.1   Overview

Mechanical interactions between the cell and the extracellular matrix play a critical role in cell biology. The extracellular matrix (ECM) is an interconnected network of biopolymers that provides structural support for cells and allows the diffusion of biochemicals within tissues. The most abundant component of ECM is type I collagen, a fibrous protein responsible for giving the ECM its material stiffness [1]. Cells attach and move through the ECM using protein complexes that link the ECM to the force-generating cell cytoskeleton [2]. However, these cell-ECM adhesions also act as sensors, sending information to the cell about the structure and mechanical properties of the surrounding matrix [1] and helping to regulate cell behavior such as motility, morphology, and differentiation [3, 4, 5]. The stiffness and the relative alignment of fibers in the network are particularly important to cell function. For example, dense and rigid collagen gel can promote growth and progression of cancer cells and tumors [6, 7]. Other important examples are durotaxis in which cells tend move in the direction of increasing matrix stiffness [8], and contact guidance in which cells tend to align and move in the direction of fiber alignment [9, 10].

Cell-ECM interaction is a dynamic process in which the cell actively remodels

the network [11] and these effects can propogate over long distances. Specifically, tension exerted by the cells can align the fibers in the network leading to long range force transmission [12]. Stresses transmitted by the network fibers can trigger mechano-sensitive pathways of distant cells affecting behaviors such as force generation [13] and cell-ECM adhesion [14]. These mechanical interactions between cells provides a means for communication and plays an important role in regulating and coordinating collective cellular dynamics in a wide range of biophysical processes, such as morphogenesis, tissue regeneration, and cancer progression [15].

Due to their effect on cell behavior and communication, a significant amount of work has been carried out to characterize the structural and mechanical properties of biopolymer networks. Traditional models have quantified network structure using morphological descriptors such as the distribution of fiber length [16], pore-size [17], and turbidity [18]. In addition, many studies have shown that fiber structure influences transport properties of the network such as macromolecular diffusivity [19], and mechanical properties such as elastic moduli and stress distribution [20, 21]. Studying these physical properties of biopolymer networks is essential for understanding how they affect chemical and mechanical signaling between cells.

Previous studies of collagen network structure have mostly focused on bulk averaged properties. In Chapter 2, we provide a comprehensive and quantitative spatial-temporal characterization of the microstructure of type I collagen-based ECM as the gelation temperature varies. Confocal reflection microscopy is used to image the collagen network during growth and at a range of temperatures. The

network structure, including the density and alignment of fibers, is characterized by calculating the density correlations and nematic order correlations from the confocal images. These functions provide information about higher order fluctuations in the network structure that are overlooked by most previous studies. We find that as temperature increases, the gel microstructure varies from a bundled network with strong orientational correlation between the fibers to an isotropic homogeneous network with no significant orientational correlation, as manifested by the decaying of length scales in the correlation functions. We have also developed a kinetic Monte-Carlo collagen growth model to better understand how ECM microstructure depends on the temperature and collagen concentration. We show that the nucleation rate, growth rate, and an effective hydrodynamic alignment of collagen fibers fully determines the spatiotemporal fluctuations of the density and orientational order of collagen gel microstructure.

Mechanical properties of collagen gel is often characterized by bulk rheology; however, variations in the collagen fiber microstructure, such as those characterized in Chapter 2, and cell adhesion forces cause the mechanical properties to be inhomogeneous at the cellular scale. In Chapter 3 we present experimental techniques for studying the mechanics of type I collagen on the scale of tens to hundreds of microns by using holographic optical tweezers (HOT) to apply pN forces to microparticles embedded in the collagen fiber network. The mechanics at this microscopic scale are more directly relevant to individual cell behavior than bulk averaged properties. We find rich mechanical behavior at the microscopic scale, due the discrete nature of the collagen fiber network. In response to op-

tical forces particle displacements are generally inhomogeneous, anisotropic, and asymmetric. Consistent with the results of Chapter 2 which showed structural differences between gels prepared at different temperatures, gels prepared at 21°C and 37°C show qualitative differences in their micromechanical characteristics as well. We also demonstrate that contracting cells remodel the micromechanics of their surrounding extracellular matrix in a strain-dependent and distance-dependent manner. To further understand the micromechanics of cellularized extracellular matrix, we have constructed a computational model which simulates the collagen network using a 2D triangular lattice. The model reproduces the main experimental findings including the variations in micromechanical properties and alteration of these properties due to active cell traction forces.

Interactions between cells and the ECM are a dynamic process, in which the cells actively deform and remodel their surroundings. In Chapter 4 we show that 3D collagen gels are significantly and irreversibly remodeled by cellular traction forces. In addition we find that plasticity of collagen gels can be described in mechanical terms. We use a parallel plate rheometer to apply a macroscopic shear strain to collagen and find that mechanical strains can lead to irreversible deformation of the network, even without the presence of cells. In addition, bulk relaxation kinetics are history-dependent, with the rate of relaxation and the residual strain depending on the magnitude and duration of the applied shear strain. We also use our technique for micromechanical characterization using optical tweezers (presented in Chapter 3) to show that microscopic remodeling leads to permanent changes in the micromechanics of collagen ECM. To understand this ECM plas-

ticity, we present a computational model that takes into account the sliding and merging of ECM fibers. The model is able to confirm the experimental results for cell-induced remodeling and macroscopic shear rheology. These results suggest that cell-induced remodeling of the ECM may lead to structures that enhance mechanical coupling between cells and have a dramatic effect on cell-cell communications in 3D fibrous matrices. Mechanical plasticity of collagen gels may have important implications for the study of tissue development and cancer progression.

The remainder of this introduction will provide additional information on cells and the extracellular matrix, as well as previous experimental and theoretical work on the structure and mechanics of biopolymer networks.

1.2   Cell and Extracellular Matrix Mechanics

1.2.1   Extracellular Matrix Structure

The tissues in our bodies are groups of cells that act together for specific functions. One major type of tissue, and the one most relevant to the research presented in this thesis, is connective tissue. Stiffer connective tissues (like bone) provide a structural framework for the body and softer connective tissues wrap around organs and blood vessels, protecting and supporting them [22]. Figure 1.1 shows a simple illustration depicting connective tissue in relation to organs and blood vessels. We also see the epithelium, a layer of closely packed cells that line the outer surfaces of organs and cavities within our bodies. Similarly, the endothelium
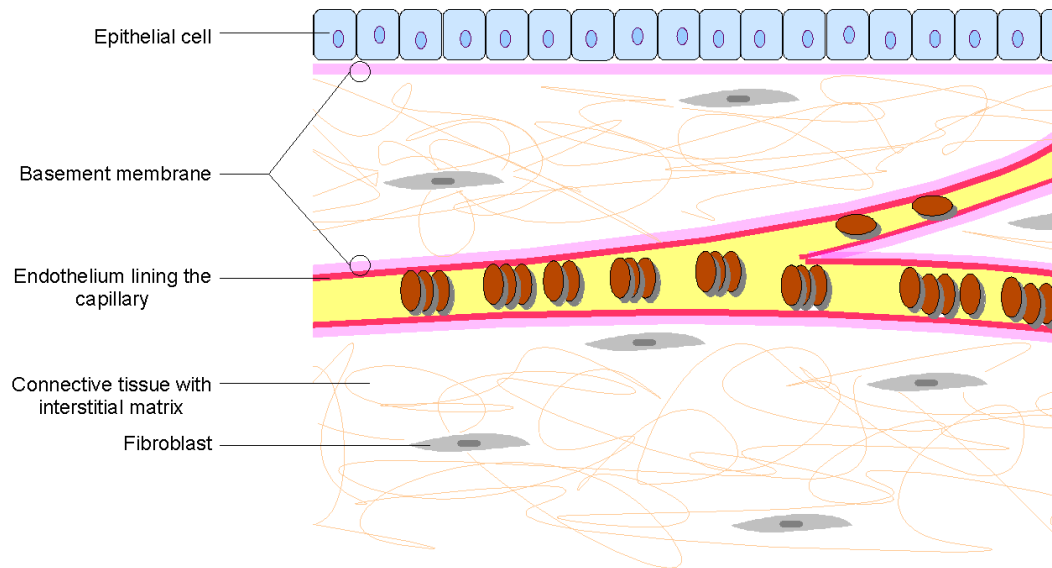
Figure 1.1: Illustration depicting extracellular matrix in relation to epithelium, endothelium, and connective tissues. (Image from Boundless Anatomy and Physiology, boundless.com)

lines the blood vessels. Both epithelial and endothelial cells are attached to a basement mebrane which separates them from the interstitial matrix.

Connective tissue mainly consists of the extracellular matrix (ECM) which is made up of a network of biopolymers. The majority component of the ECM is collagen, the most abundant protein in the human body. There are many types of collagen, but the most common are the fibrillar types I and III. Collagen fibers endow connective tissues with its material stiffness and are the structural scaffold for cells living in connective tissue [1].

The most common type of cell in connective tissue are fibroblast cells, which are responsible for building and maintaining the ECM. Fibroblasts are continuously synthesizing new collagen fibers [23] and can also break them down through the

elastin   fibroblast   collagen   fibroblast   fibroblast   collagen
fiber   cell   fiber   nucleus   cells   fibers

A   B
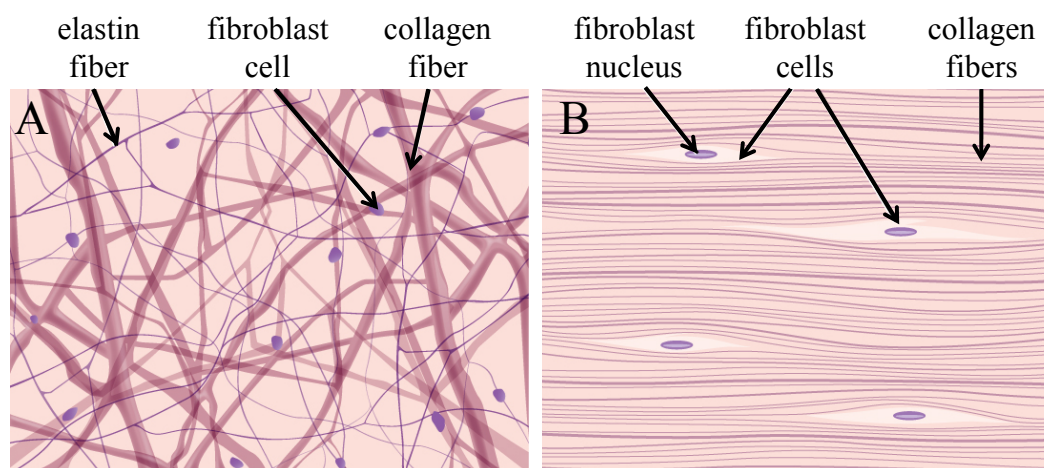
Figure 1.2: Illustration showing both loose (A) and fibrous (B) connective tissue. (Images adapted from Boundless Anatomy and Physiology, boundless.com)

secretion of certain proteases [24]. In addition to collagen, there are many other fibers and proteins present in the ECM such as elastic fibers, made up of a core of elastin surrounded by microfibrils. These allow tissues to extend upon loading and recoil upon unloading [1]. As with collagen, fibroblast cells are responsible for secreting elastin fibers to maintain the elastic properties of the ECM.

There are many types of connective tissue within the body such as loose and fibrous connective tissue. Figure 1.2 shows an illustration of both these types of connective tissue. In loose connective tissue (Figure 1.2A), there is much more space between the fibers of the ECM and there are also more cells. This tissue is flexible yet strong and is the kind that wraps around vessels and organs to protect and support them. In fibrous connective tissue (Figure 1.2B), there are fewer cells and the ECM fibers are very tightly packed together. The aligned fibers shown in the figure are typical of tendons or ligaments, whereas other tissues which need to

withstand compression from different directions (such as bone) have more random fiber orientations. The collagen gel microenvironments discussed in the rest of this thesis are most similar to loose extracellular matrix, although without the additional biopolymers and proteins present *in vivo*.

1.2.2 Cell Adhesion and Migration

Cells anchor themselves and apply forces by forming adhesion sites which link the cell cytoskeleton to the ECM. The cytoskeleton is a biopolymer network within the cell that maintains its shape and also carries out many intracellular processes [2]. The cytoskeleton is made up of different biopolymers such as microtubules, intermediate filaments, and actin filaments. The main cytoskeletal component we are concerned with is the actin microfilament network because it is the component of the ECM responsible for exerting traction forces on the ECM. The motor protein myosin is able to slide along the actin filaments, contracting the cytoskelton and allowing the cell to apply contractile forces. Figure 1.3A-B show an image of a cell stained for actin (magenta) and adhered to a collagen-based ECM. Figure 1.3C illustrates a simple model of a contractile cell ahdered to an elastic ECM. The cell applies a contractive force until it reaches equilibrium with the elastic forces resulting from stretching the collagen fibers in the ECM. In addition to contraction, polymerization of the actin network can create cell protrusions and exert pushing forces on the ECM.

Actin polymerization and actin-myosin contraction is also crucial for cell motil-
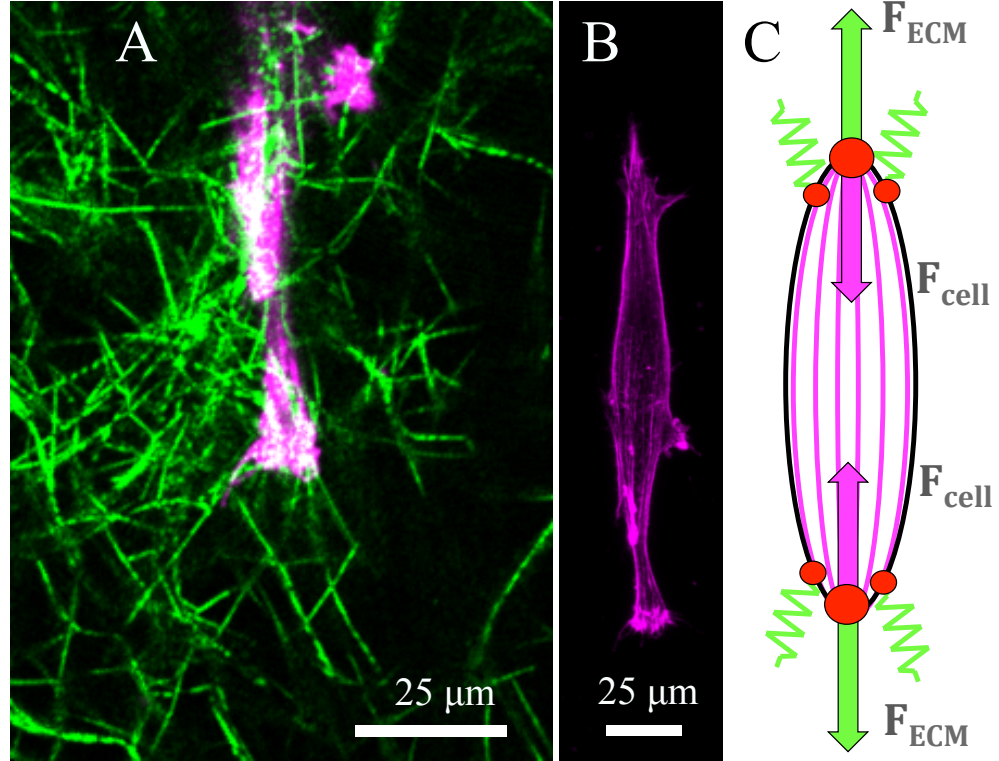
Figure 1.3: Actin cell cytoskeleton and cell contraction. (A) Zoomed in image of the cell (actin stained magenta) adhesion to the collagen ECM (green). (B) Image of the same cell stained with actin (magenta). (C) Simplified model of a contracting cell in the elastic ECM. Cell adhesion sites represented by red circles.

ity. One method by which cells migrate through the ECM is by first sending out actin protrusions which adhere to the ECM. The rear of the cell then releases its adhesions and the actin network contracts to pull the cell body forward [25]. Other modes of migration are possible, such as lobopodia based migration in which a large protrusion is created by intracellular pressure rather than actin polymerization [26]. The mode of cell migration in 3D matrices is strongly dependent on the structural and mechanical properties of its microenvironment through mechanisms

which will be discussed in Section 1.2.3.

1.2.3   Mechanotransduction Regulates Cell Behavior

In addition to anchoring the cell to the ECM, adhesion sites also act as force sensors capable of detecting mechanical cues from the environment through a process called mechanotransduction. Figure 1.4 shows an example of a fibroblast cell attached to the ECM. The zoomed in image shows a typical adhesion site where the ECM is linked to the interior actin cytoskeleton by the integrin protein complexes. In addition to physically linking the active cell cytoskelton to the ECM, the integrin complexes also include force-sensitive linker proteins which can release signaling molecules to the cell cytoplasm [1]. These can trigger signalling pathways, such as RHO and ROCK [10, 14], which control cell activity. For example, external tension can increase actin-myosin activity which in turn increases cell contractility and tension [27]. This creates a positive feedback loop and leads to growth and stability of the actin network.

Positive and negative feedback due to mechanotransduction regulates many different cell behaviors. The morphology of cells, including the structure of the cytoskeleton and cell-ECM adhesions, are strongly dependent on the stiffness of the cell substrate. Cells grown on stiffer substrates can form large focal adhesions and develop large aligned actin fibers, or stress fibers, within the cytoskeleton [4]. Matrix stiffness can also affect the differentiation of cells. Stem cells have been shown to be extremely sensitivite to tissue-level elasticity, and will specify lineage
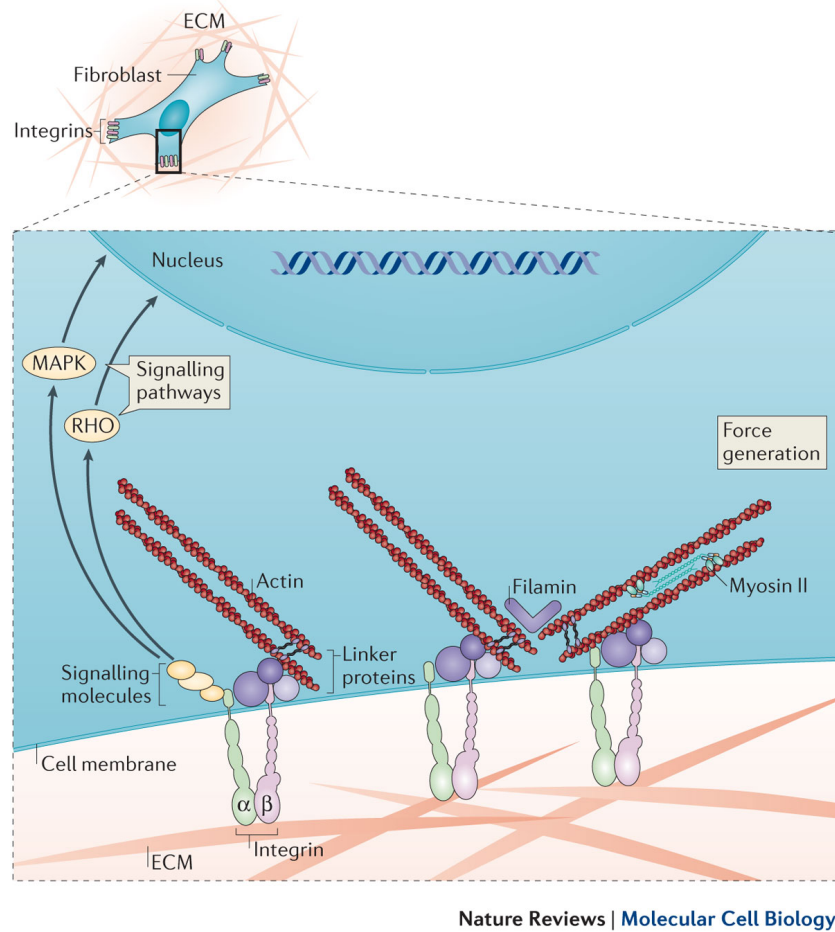
Figure 1.4: Cell-ECM adhesions and mechanotransduction (from Ref. [1]).

and commit to different phenotypes based on the stiffness of their environment [5]. These effects mean that mechanical forces due to the ECM are extremely important during morphogenesis in young embryos and throughout tissue development [28].

Cell migration can also be guided by the local ECM fiber network. It has been shown that cells probe their environment with small protrusions, called filopodia, before moving to occupy an area [29]. Cells have a higher tendency to move in

the direction of larger substrate stiffness. This tendency of cells to move in the direction of the stiffness gradient is called durotaxis, and has been demonstated in 3D collagen matrix [8]. In addition to stiffness, cells are also sensitive the alignment of fibers in the ECM. Through contact guidance, cells tend to elongate and migrate in the direction of local fiber alignment [9, 10].

Mechanotransduction regulates many vital cell behaviors, but defects in these mechanisms can contribute to many different diseases, such as cancer [30]. Although genetic changes initiate the beginning of cancer, biomechanical cues from the ECM have a large impact on the behavior of tumor cells. Typical hallmarks of cancer include unsuppressed growth, death resistance, and invasion into surrounding tissues [31]. Tumors are stiffer than normal tissue because increased cytoskeletal tension stimulates integrin signaling, increases cell-ECM adhesions, and increases cell contractility. It has been shown that stiffer ECM can stimulate cell growth and decreases the adhesion of cells to their neighboring cells, making them more likely to transition to a malignant phenotype [7, 32]. Thus a deeper understanding of how mechanical cues from the ECM influence tumor cells is critical to the study of cancer malignancy.

Mechanotrasduction provides a regulatory system of positive and negative feedbacks that uses integrin complexes to sense physical cues from the ECM and triggers molecular pathways that control cell growth and behavior. This sensitivity of cells to the local mechanical properties of their environment is the reason why it is so important to better understand the mechanics of cellular environments on the microscopic scale.

1.2.4 Cell-Cell Interactions and Collective Cell Behavior

Collective cell behavior is necessary for many biological functions. For example, collective cell migration is required for wound healing and also cancer invasion. In collective migration, individual cells still rely on the same actin mediated protrusions and mechanical cues from the ECM; however, they also need some means of coordinating their behavior with other cells. One means of communication during cell migration is the formation of direct cell-cell adhesions which mechanically link the cells and provide junctions through which the cells can communicate biochemically [15]. However, cells can also interact mechanically through forces transmitted by the ECM.

The ability of cells to transmit stresses through the ECM is highly dependent on the fiber network geometry of the collagen matrix. Mechanical tension between cells can lead to alignment of fibers and create fibers that carry large amounts of stress [33]. These high stress fibers can connect distant cells and can provide a means of mechanical communications. The stresses in fibrous ECM networks can propogate relatively long distances ($\sim 10\mu$m or 10 cell diameters), longer distances than they would be transmitted in a homogeneous material [12].

Recent experiments have shown that mammary acini (clusters of cells) seeded in collagen matrix can interconnect by forming long lines of fibers between clusters [34]. Over time, the acini disorganize as cells transition to an invasive phenotype and break off from the cluster. Clusters that interacted with one another through lines of collagen fibers broke up more rapidly, showing that the interactions between

distant clusters could be stimulating cells to differentiate more rapidly. This is further evidence that mechanical interactions are critical for cancer metastasis.

1.2.5   Cell Remodelling of the Extracellular Matrix

Cells are continually remodelling the ECM to maintain healthy tissue and organ function. To maintain tissue homeostasis, cells move through the ECM, breaking down old fibers and laying down new ones [1]. Over time, aging decreases the ability of tissues to regenerate and maintain healthy function. One reason for this is a decrease in stem cells within tissue; however, changes in ECM structure also contribute to decreased tissue function [35]. The proper structure of the ECM degrades, leading to an environment less hospitable to new cells, and in turn, fewer healthy cells to repair the matrix. This degradation is apparent in the loss of skin elasticity over time (wrinkles) and loss of muscle and bone mass. Although cell regulation of the ECM naturally decreases over the span of a person's life, serious diseases, like fibrosis and cancer, can arise when cells are unable to regulate the proper structure and stiffness of the ECM [11, 36].

Fibrotic diseases, such as pulmonary fibrosis, systemic sclerosis, and cardiovascular disease, account for over 45% of deaths in the developed world [36]. Fibrosis is the result of cells responding abnormally to some organ injury or tissue inflamation. It is characterized by increased proliferation of fibroblasts, which differentiate into myofibroblasts and synthesize excessive amounts of ECM [37]. This high density ECM dramatically alters the mechanical properties, such as tissue stiffness,

and further hinders organ function. In the extreme, this can lead to the formation of scar tissue within organs such as the lungs, liver, and heart.

As mentioned above, mechanical cues from the ECM can also influence cancer progression. Local increases in collagen density and alignment can affect cancer cell migration and the ability of immune cells to interact with the cancer cells [11]. Remodeling of the surrounding ECM increases tissue stiffness around tumors and further stimulates tumor growth and malignancy.

1.3 Characterization of Biopolymer Network Mechanics

1.3.1 Structural Characterization using Confocal Microscopy

Confocal microscopy is a technique commonly used for imaging the microscopic structures of biopolymer networks. Confocal microscopy is a technique capable of taking high-resolution 2D images deep inside a sample. Two pinholes in the optical path remove out-of-focus light, providing excellent contrast and resolution. In addition, blocking the out-of-focus light means only a thin region, or slice, of the sample near the focal plane will be imaged. This allows one to take many slices at different depths and combine them to form a 3D image of the sample, also known as an image stack or z-stack.

A laser scanning confocal microscope (LSCM) illuminates and observes a single spot at a time by using mirrors to scan a focused laser spot across the sample. Detectors then collect the light which is transmitted through, reflected back, or

fluorescently emitted from the sample. This allows researchers to stain a single sample with multiple fluorescent dyes or labels and then image them all in sequence using different filters or channels.

Confocal reflection microscopy (in which reflected light from the sample is collected) has been used to study the self-assembly of collagen-based extracellular matrix. These studies quantified the growth rate of the collagen network using turbidity (total image intensity) versus time and explored the effects of collagen concentration [18] and the inclusion of additional ECM biopolymers [38] on the final collagen network structure.

Confocal reflection microscopy has also been used to characterize the strain-induced alignment of collagen fibers [39]. It is shown that both colonies of cells and purely mechanical strain of the collagen network can lead to fiber alignment, and that this fiber alignment may be partially irreversible.

The pore size of a biopolymer network is the size of the open gaps between discrete fibers, in which there is only the liquid solvent. One can imagine the pore size as the diameter of the largest sphere which can fit into the network without intersecting any fibers. Pore size has been shown to affect the molecular transport properties of biopolymer networks [19], the ability of cells to attach and adhere to collagen matrix [40], and the inasiveness of cells in collagen gels [17]. Confocal microscopy has been used to quantify the pore size of biopolymer networks using various image analysis techniques [41, 42, 43].

Computational reconstructions of real collagen networks have quantified several key parameters for characterizing network geometry in addition to fiber density

and pore size [16]. One is the distribution of fiber lengths within the network, and another is the relative alignment of nearby fibers. The third, which will be discussed further in Section 1.4.2, is the connectivity, or coordination number Z. This quantifies the number of fibers meeting at any node in the network, and for collagen is typically $Z \approx 3.4$ [16].

1.3.2 Bulk Rheology

Many of the previous mechanical characterizations of biopolymer gels, especially collagen, have been done by measuring the bulk rheology of the gel. Rheology describes the mechanical response of the material under deformation and in terms of the elastic moduli. Two of the elastic moduli for homogeneous isotropic materials are the Young's modulus E and the shear modulus G. The Young's modulus quantifies the stiffness of the material under axial compression or expansion (Figure 1.5A) and the shear modulus gives the stiffness of the material under shear deformation (Figure 1.5B). In both cases, the moduli relate the stress σ on the surfaces to the strain ε by

$$\sigma = E\varepsilon \quad , \quad \sigma = G\varepsilon \tag{1.1}$$

where the stress is defined as the force per unit area

$$\sigma = F/A. \tag{1.2}$$
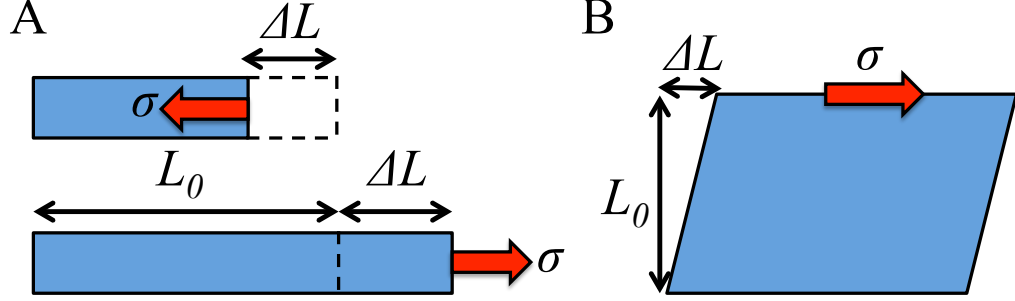
Figure 1.5: Diagram of simple axial compression or expansion (A) and shear deformation (B). The red arrows represent the stress σ applied to the surfaces.

The strain is a dimensionless ratio of the deformation ΔL to L_0, the length (for stretch or compression, Figure 1.5A) or thickness (for shear, Figure 1.5B) of the unstrained material.

$$\varepsilon = \Delta L / L_0 \tag{1.3}$$

Previous work has been able to predict bulk elastic moduli, like the Young's modulus, from the network structure by analyzing microscopy images of collagen networks [44].

Most studies of biopolymer rheology use continuous shear deformation using a parallel plate rheometer. In these experiments, the sample is placed between the two circular parallel plates of the rheometer. The plates are rotated relative to one another to apply a rotational shear stress or strain to the sample. If the applied strain is oscillatory, then the response of the gel can be quantified by the dynamic shear modulus

$$G^* = G' + iG'' \tag{1.4}$$
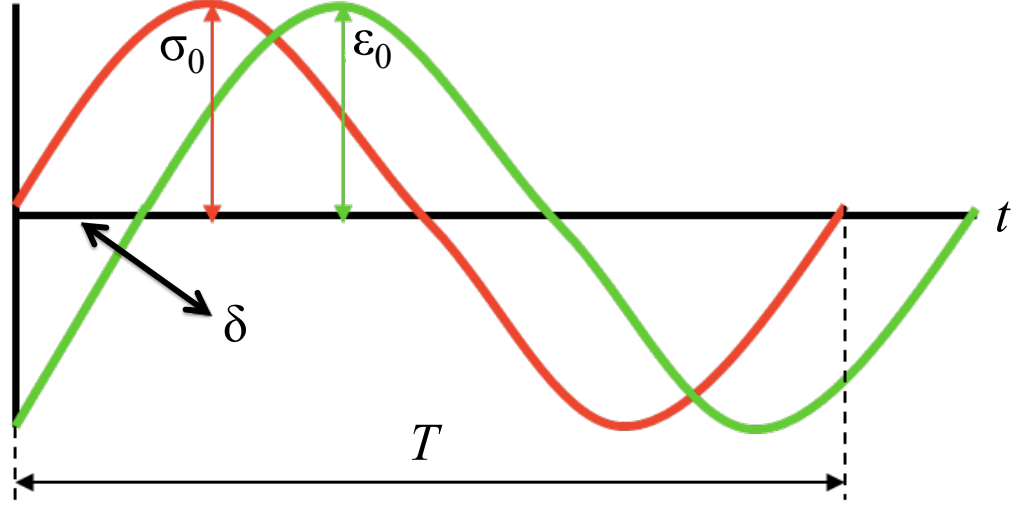
Figure 1.6: Example plot of a sinusoidal applied strain ε (green) and the resulting stress σ (red) versus time showing the relative phase δ.

where G' is the storage modulus and G'' is the loss modulus. G' characterizes elastic response of the gel and leads to stress in phase with the applied strain. G'' characterizes viscous response and leads to stress out of phase with the applied strain. The relative phase δ between the strain and stress is shown in Figure 1.6 and is given by $\delta = tan^{-1}(G''/G')$. Both the storage and loss moduli are generally dependent on the frequency and magnitude of the oscillatory strain.

Measurement of the dynamic modulus has been used to characterize the self-assembly of collagen as the storage modulus grows throughout polymerization [45]. Previous works has also been able to use structural data from confocal microscopy to predict the dynamic shear response of collagen gel [20].

A major goal for rheological studies on collagen has been to study the nonlinear elasticity of the networks. Collagen exhibits strain stiffening, meaning that the

stiffness of the network increases as the strain amplitude increases. In fact, it has been shown that nonlinear stiffening can occur as low as 10% strain and that the storage modulus can increase by more than an order of magnitude before network failure [46]. In addition, the nonlinear stress response of collagen is also history-dependent, meaning that repeatedly stressing and straining the gel will alter the mechanical properties. It has been shown that repeated straining leads to a shift of the characteristic nonlinear stress-strain relationship to higher strains, thus delaying the onset of strain stiffening [47].

While the above results used oscillatory shear deformations, this is not necessary to characterize the nonlinear elasticity of biopolymer networks. For example, strain stiffening can be measured by increasing the magnitude of shear strain at a constant rate in a single direction [48]. In addition, it has been shown that holding biopolymer gels at a fixed strain within the nonlinear regime will lead to relaxation of stress over time [49]. In other words, the longer you hold the biopolymer gel at a fixed strain, the easier it gets to hold it there. This result, along with the history-dependence shown with oscillatory strain, suggests that the structure and mechanics of collagen gel are dynamic and can adapt to external stresses and strains. This change in mechanical properties is fundamentally dependent on the fiber network microstructure of biopolymer gels in which individual bonds within the network can dynamically break, rearrange, and reform into more favorable configurations. The plasticity of collagen based ECM is discussed further in Chapter 4.

Studies on the nonlinear properties of collagen are important because the non-

linearity is thought to have an important effect on cell-ECM interactions. Highly contractile cells can deform the surrounding network into the nonlinear regime and this leads to different stress distributions when compared to linear deformations. Probing this stress distribution is necessary for cells to detect the position and orientation of neighboring cells and may be aided by the nonlinear properties of the matrix [50].

1.3.3 Microrheology

The mechanical properties of materials can also be measured on the microscopic scale using microrheology. Microrheology refers to techniques in which small probe particles are embedded in samples and then the motion of these particles is observed to extract the local viscous and elastic properties. In passive microrheology, the particle motion is due only to thermal fluctuations. In one method, the particle is tracked by using a low power laser, which is focused on the particle and then directed onto a quadrant photodiode (QPD). Deviations of the particle from the center of the beam will change the intensity readings on the QPD, which reveals the particle trajectory [51]. The elastic moduli can then be calculated from the particle trajectory using a frequency-dependent Stokes-Einstein equation. In another method, laser interferometry microscopy is used to measure the thermal motion and the moduli are calculated from the power spectrum of the thermal fluctuations [52].

In addition to passive microrheology, active microrheology refers to techniques

in which the probe particles are actively manipulated by some controlled force, usually optical tweezers. One method for active microrheology measures the response of micron-sized particles to an oscillating optical trapping force. Combining this with the data from thermal motion of the same particle, they can measure both the mechanical properties and identify nonequilibrium forces in the material [53].

One major advantage of microrheology over conventional bulk rheology is that the small size of the probe particles means that one can measure the elastic properties of very small sample volumes. This is particularly relevant when studying mechanics on the microscopic scale of cells and the ECM. Active microrheology has been used to measure the elastic modulus around individual cells embedded within fibrin gels [54]. They report heterogeneity in the local mechanical properties near the cell, but only for a very small number of cells and particles. In Chapter 3 we use a new active microrheology technique, using holographic optical tweezers and video microscopy, to study heterogeneity in the micromechanical properties of collagen-based ECM.

1.4   Semiflexible Polymer Networks

Biopolymers that make up the the ECM and the cytoskeleton tend to have very different mechanical properties than synthetic polymers. For one, they tend to bind together more weakly than most synthetic polymers. They also tend to be much more rigid to bending than synthetic polymers [55]. This leads to biopolymer net-

works having interesting mechanical properties, such as the nonlinear strain stiffen-ing mentioned in Section 1.3.2. One characterization of the stiffness of biopolymers is their persistence length L_p, which is the contour length at which significant bend-ing will occur due to thermal fluctuations. Biopolymers are considered semiflexible because their persistence length tends to be much longer than the single molecules or proteins of which they are made. For this reason, semiflexible biopolymers can be modeled as elastic rods which resist both bending and stretching. These individ-ual elastic fibers can then be combined into networks to simulate bulk mechanical properties.

1.4.1   Worm-Like Chain Model

The worm-like chain model treats individual biopolymer fibers as elastic rods which resist both bending and stretching. When including stretching, it is typically referred to as the extensible worm-like chain model. As shown in Figure 1.7, the rod is modelled to have radius a, the length s defines the position along the axis of the fiber, and the unit tangent vector $\vec{t}(s)$ defines the local orientation of the fiber at position s [55].

The resistance of the fiber to bending can be described by the bending energy

$$H_{bend} = \frac{\kappa}{2} \int ds \left| \frac{d\vec{t}(s)}{ds} \right|^2 \tag{1.5}$$
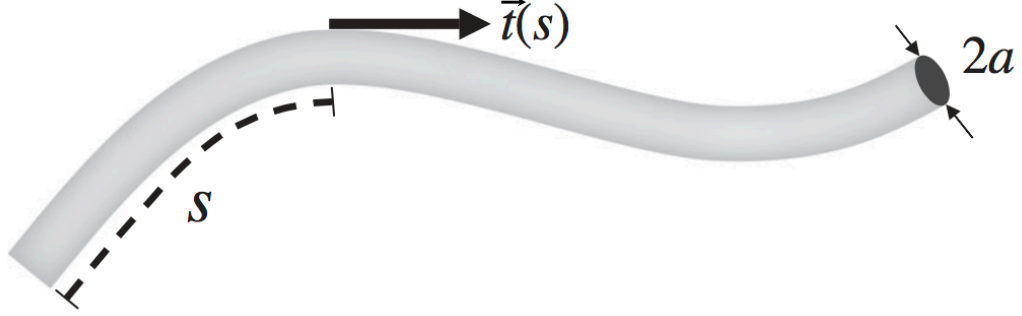
Figure 1.7: Diagram of biopolymer fiber modelled as an elastic rod with radius a. The position along the axis of the fiber is s and $\vec{t}(s)$ is the local unit tangent vector. (From Ref. [55]).

where κ is the bending modulus of the fiber. The unit tangent vector is given by

$$\vec{t}(s) = \frac{d\vec{r}(s)}{ds} \qquad (1.6)$$

where $\vec{r}(s)$ is the position of the filament relative to some arbitrary origin. For a homogeneous rod of diameter $2a$ consisting of a homogeneous material, the bending modulus should be proportional to the materials Youngs modulus E. In the case of an elastic rod with circular cross section, the bending modulus is

$$\kappa = \frac{\pi}{4}Ea^4. \qquad (1.7)$$

Using the equipartition theorem, one can use the above bending energy to show that the persistence length for the fiber will be

$$L_p = \frac{\kappa}{k_B T} \qquad (1.8)$$

where T is the temperature and k_B is Boltzmann's constant.

In addition to bending, the fiber will also have a stretching energy given by

$$H_{stretch} = \frac{\mu}{2} \int ds \left(\frac{dl(s)}{ds} \right)^2. \tag{1.9}$$

The term dl/ds represents the relative change in length along the filament and the stretch modulus is

$$\mu = \pi E a^2. \tag{1.10}$$

The total elastic energy of the fiber is then the sum of the bending and stretching energies integrated along the entire length s of the fiber.

1.4.2   Elastic Fiber Networks

To simulate the bulk mechanics of biopolymer gels, one can create a network of fibers, each of which can be modelled as an elastic rod as described above. These networks are contructed on a discrete lattice, usually a triangular or Mikado lattice (intersecting straight lines) [48]. The total elastic energy H is calculated by summing the bending and stretching energies of every fiber in the network

$$H = \sum_f \left(H_{bend_f} + H_{stretch_f} \right). \tag{1.11}$$

Some strain can be imposed on the network using fixed boundary conditions and then finding the fiber structure which minimizes the total elastic energy. The

stress is then calculated by varying the applied strain and finding the the resulting change in the total energy of the network. The stress is defined as

$$\sigma = \frac{1}{V}\frac{\partial H}{\partial \varepsilon}.$$ (1.12)

The resulting relationship between stress and strain give the elastic moduli for the simulated network. Although these simulations can be run on either 2D or 3D lattices, the 2D simulations are usually sufficient to capture the mechanical properties observed experimentally.

One important parameter when forming these fiber lattices is the connectivity, or coordination number z. This number represents average the number of fiber segments which meet at any given junction. The connectivity has a large effect on the resulting mechanics of the fiber network. For collagen matrix, a typical connectivity is $z \approx 3.4$ [16], which is important because it is below the "isostatic" or critical connectivity. This means that the network would not be mechanically stable if there were only spring-like stretching energies ($\kappa = 0$) [56]. The consequence of the low connectivity is that collagen matrix mechanics is dominated by the bending energy at low stesses and strains. At higher strains, the stretching energies start to play a role and contribute to the nonlinear strain stiffening of collagen gel. Recent simulations based on elastic fiber networks have been able to reproduce the nonlinear elasticity seen experimentally in bulk rheology [48, 56]. In Chapters 3 and 4 we present lattice based models to better understand the micromechanics and plasticity of collagen-based ECM.

2 The Spatial-Temporal Characteristics of Collagen Extracellular Matrix

In this chapter we provide a quantitative characterization of the microstructure of type I collagen-based ECM for a range of gelation temperatures. We have also developed a kinetic Monte-Carlo collagen growth model to better understand how ECM microstructure depends on the temperature and collagen concentration. We show that the nucleation rate, growth rate, and an effective hydrodynamic alignment of collagen fibers fully determines the spatiotemporal fluctuations of the density and orientational order of collagen gel microstructure.

The results of this work were published in the journal *Soft Matter* [57]. Christopher Jones was in charge of all sample preparation, confocal imaging and data collection. The data analysis code for calculating nematic order was developed by Dan Lin. The simulation using the kinetic Monte-Carlo method was developed by our collaborators at Arizona State University, Long Liang and Professor Yang Jiao.

2.1 Introduction

As a major component of mammalian extracellular matrix (ECM) such as skin, tendon, and organs, collagen I makes up about 25% of the entire protein content

of the body [58]. Physiologically, collagen I molecules are synthesized by stromal cells, such as fibroblasts in order to maintain the integrity of extracellular matrix. When such functions are compromised, the human body develops several fatal diseases, such as Ehlers-Danlos syndrom and Infantile Cortical Hyperostosis [59].

Collagen I has been widely used in tissue engineering as a scaffold protein [60, 61] because it naturally forms gels of hierarchical structure that are friendly to cells and growth factors [62]. Monomeric collagen I can self-assemble into fibrils that are approximately 300 nm long and 1.5 nm in diameter. The fibrils further bundle together to form thick fibers that are more than 1 μm long and 100 nm in diameter. These fibers dominate the mechanical and transport properties of collagen I gel [16, 19] and they can be directly visualized without tagging probes using phase contrast [45, 63], confocal reflection [38, 39, 64] , or second harmonic generation microscopy [65, 66].

The fiber networks of collagen gel natively support the adhesion of many types of cells. As a result, it has been adapted as a popular model ECM for 2D and and 3D cell culture. Many studies have shown that cells cultured in collagen I gel are sensitive to the fiber matrix structure. For instance, dense and rigid gel promotes growth of cancer cells [6, 7]. Highly-aligned collagen fibers may induce malignant transition of mammary acini into invasive phenotypes [34]. The microstructural heterogeneity of collagen gel has also been shown to guide the cell migration through durotaxis [8] and contact alignment [9]. In addition, the physical properties of collagen ECM such as the effective diffusion coefficient [19, 67, 68] and stress distribution [69, 70, 12], which are respectively crucial to the chemical

and mechanical signaling between cells, are determined by the fiber network con-gigurations. These observations highlight the diverse mechanical cues generated by collagen ECM, and the importance of understanding the factors that determine the microstructures of collagen gel.

To date most structural characterization of collagen gel, such as porosity [17, 40], pore-size distribution [41, 42] and turbidity [18, 38], have been mainly focused on the bulk averaged properties. There is a lack of data to characterize the spatial heterogeneity of the fiber network [71], and how the matrix microstructure can be tuned. The spatial heterogeneity of collagen gel is closely related with the exis-tence of fiber clusters, bundles of fibers which are closely aligned. In this article, by employing sophisticated statistical morphological descriptors devised in condensed matter physics [72] and heterogeneous material theory [73], we provide a compre-hensive and quantitative spatial-temporal characterization of the microstructure of type I collagen-based ECM as the gelation temperature varies. In particular, we combine confocal microscopy and image correlation analysis to systematically study the fibrous configurations of collagen gel. We characterize the growth kinet-ics as well as the static microstructure of collagen gel by quantifying the spatial fluctuations in fiber density and orientation with the density and nematic correla-tion functions, respectively.

In order to better understand how collagen ECM microstructure depends on the environmental and kinetic factors, we have developed a kinetic Monte-Carlo model based on the experimental measurements to simulate the growth dynamics of a collagen gel at fixed gelation temperatures. Our model suggests that the static

structure of collagen gel is inherently connected with the growth kinetics. In particular, it shows that the nucleation rate, growth rate, and an effective hydrodynamic alignment of collagen fibers fully determines the spatiotemoral fluctuations of the density and orientational properties of collagen gel microstructure. Our model also enables us to determine the temperature dependence of the nucleation rate and growth rate, which are difficult to directly measure in experiments.

2.2   Results

2.2.1   Growth Dynamics of the Collagen Matrix

The spatial heterogeneity of collagen gel is closely related with the existence of fiber clusters, bundles of fibers that are aligned closely. Figure 2.1 shows typical confocal reflection images of collagen gel formed around room temperature, where fiber clusters can be easily identified visually. In order to quantify the structural evolution of collagen fibril network during gelation, we use reflection mode of laser scanning confocal microscope (LSCM, Leica SPE) to image a 2D slice of a thick collagen gel. Figure 2.2 demonstrate the micro-structural dynamics in a typical gelation process. The self-assembly of collagen matrix initiates immediately from time zero, when 2 mg/mL type I collagen in acetic acid is neutralized by NaOH and buffered by $10 \times$ PBS (phosphate buffered saline) at room temperature. A few isolated fibers start to appear at random locations at around 5 minutes and move diffusively. These initial fibers anchor the nucleation of more fibers to form clusters
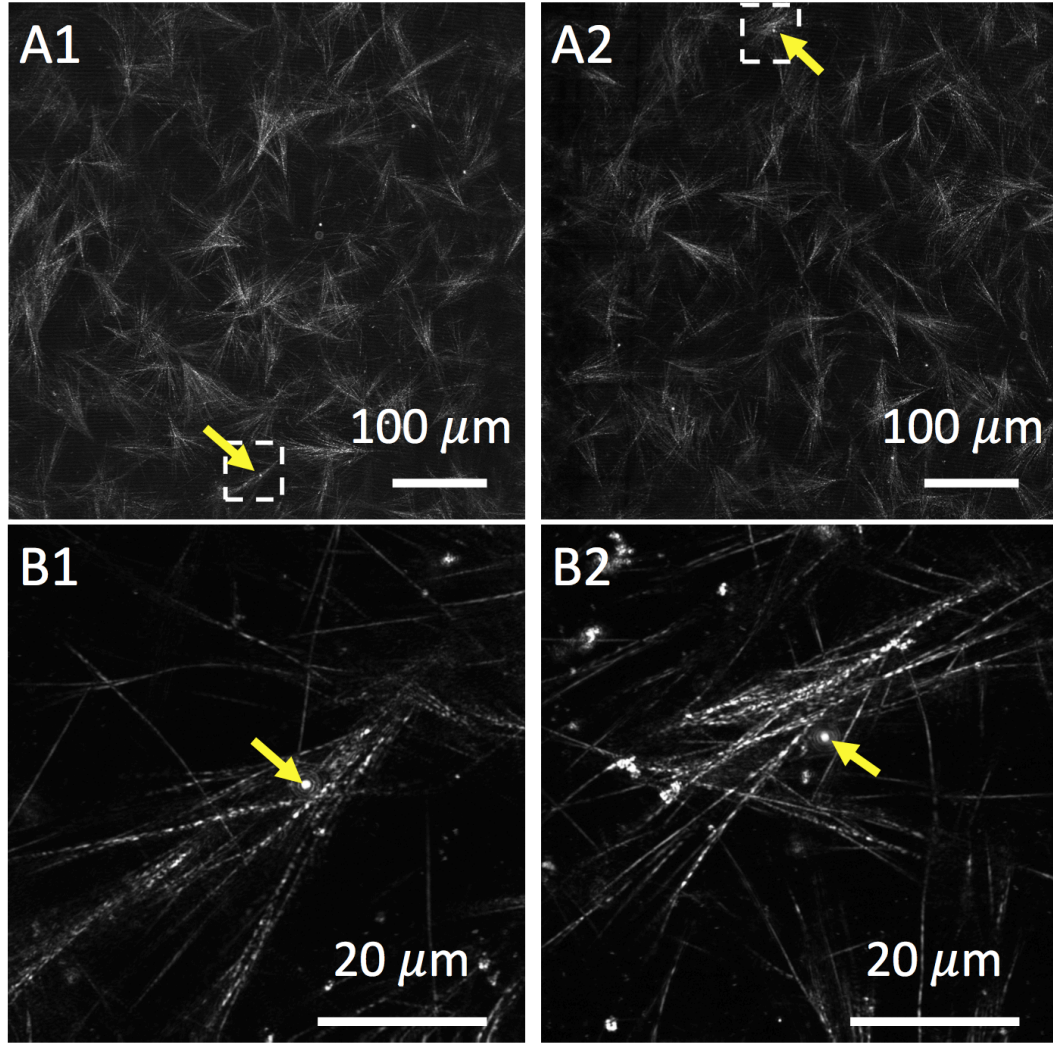
Figure 2.1: The presence of fiber clusters contributes to the structural heterogeneity of collagen gel. (A1-A2) Typical confocal reflection images of collagen gel showing many fiber clusters. Two specific clusters are highlighted by the white dashed box. (B1-B2) Zoomed in images of th collagen fiber clusters highlighted above. The images are taken using higher magnification and low density microparticles serve as markers (yellow arrow) to help find the same cluster and and focal plane.

each consisting of a few distinguishable fibers. As gelation proceeds, the viscosity and level of fiber entanglement increases. Finally, the fiber clusters are arrested and become the quenched structural heterogeneity after the gel is fully formed (Figure 2.2A). Using template-matching methods, we calculated the corresponding nematic field at different stages of gelation as shown in Figure 2.2B.

To characterize the spatial organization of the self-assembled fiber structure, we measure the two-point correlation of image intensity to approximate the spatial fluctuations in density of the gel matrix:

$$g(r) = \frac{1}{\sigma^2} < \tilde{I}(\mathbf{r_0})\tilde{I}(\mathbf{r_0} + \mathbf{r}) >_{\mathbf{r_0}}$$

$$\tilde{I} = I- < I > , \text{ and } \sigma^2 =< \tilde{I}^2 > \tag{2.1}$$

Where $I(\mathbf{r_0})$ is the 8-bit gray scale image intensity and $\tilde{I}$ is the image offset by its global average. The function $g(r)$ characterizes how likely it is that two points of distance r apart have the same intensity (Figure 2.2C). The decay of $g(r)$ slows down at later time, and plateaus at around 20 minutes, consistent with the growth dynamics of the fiber clusters. Density correlation follows a double exponential function as $g(r) = a_1 \exp(-l_1 r) + a_2 \exp(-l_2 r)$ with root mean square deviation (RMSD) less than 0.02 in all our data sets (Figure 2.2C inset). The two length scales l_1 and l_2 are well separated, typically differ by more than an order of magnitude, and are related with the thickness of each fiber and size of the fiber clusters respectively. In the beginning, when only a few fibers exist, the dominant fluc-

tuation is the fiber thickness l_1, hence $a_1 >> a_2$. At later time, the two weight coefficients become closer and the heterogeneous density of the self-assembled collagen fiber matrix can be characterized by the length scales l_1, l_2, which we will examine systematically at different gel conditions.

In addition to the density fluctuations of the collagen matrix, the fiber orientations can be characterized by 2-D nematic field $\mathbf{s}(\mathbf{r}) = \sum_n e^{2i\theta_n(\mathbf{r})}$ (Figure 2.2B), where $\theta_n(\mathbf{r})$ is the angle between a fiber at position $\mathbf{r}$ with respect to an arbitrary direction (which we choose to be the horizontal axis of the image), and the extra factor 2 makes the nematic field invariant under reflection.

To obtain the nematic field from confocal images, we have developed a template-matching algorithm (see Materials and Methods), which converts each raw confocal image (resolution 1024 x 1024 pixel resolution) into a 128 x 128 coarse-grained nematic field. The spatial organization of the fiber orientations can be evaluated by the two point correlation function of $\mathbf{s}$ defined as

$$\Theta(r) = |\frac{1}{< |\mathbf{s}|^2 >} < \mathbf{s}(\mathbf{r_0})\mathbf{s}^*(\mathbf{r_0} + \mathbf{r}) >_{\mathbf{r_0}} | \qquad (2.2)$$

where $\Theta(r)$ characterize how likely it is that two points of distance r apart have the same orientation. Notice that only points with $|s| > 0$ contribute to the correlation function. Because $\mathbf{s}(\mathbf{r})$ is intrinsically coarse-gained, $\Theta(r)$ does not depend on the fiber thickness. Instead, it measures the directional persistence along a fiber and co-alignment between nearby fibers. As the gel is forming, $\Theta(r)$ decays slower at later times, because fibers elongate and form aligned "bundles," or clusters (Figure
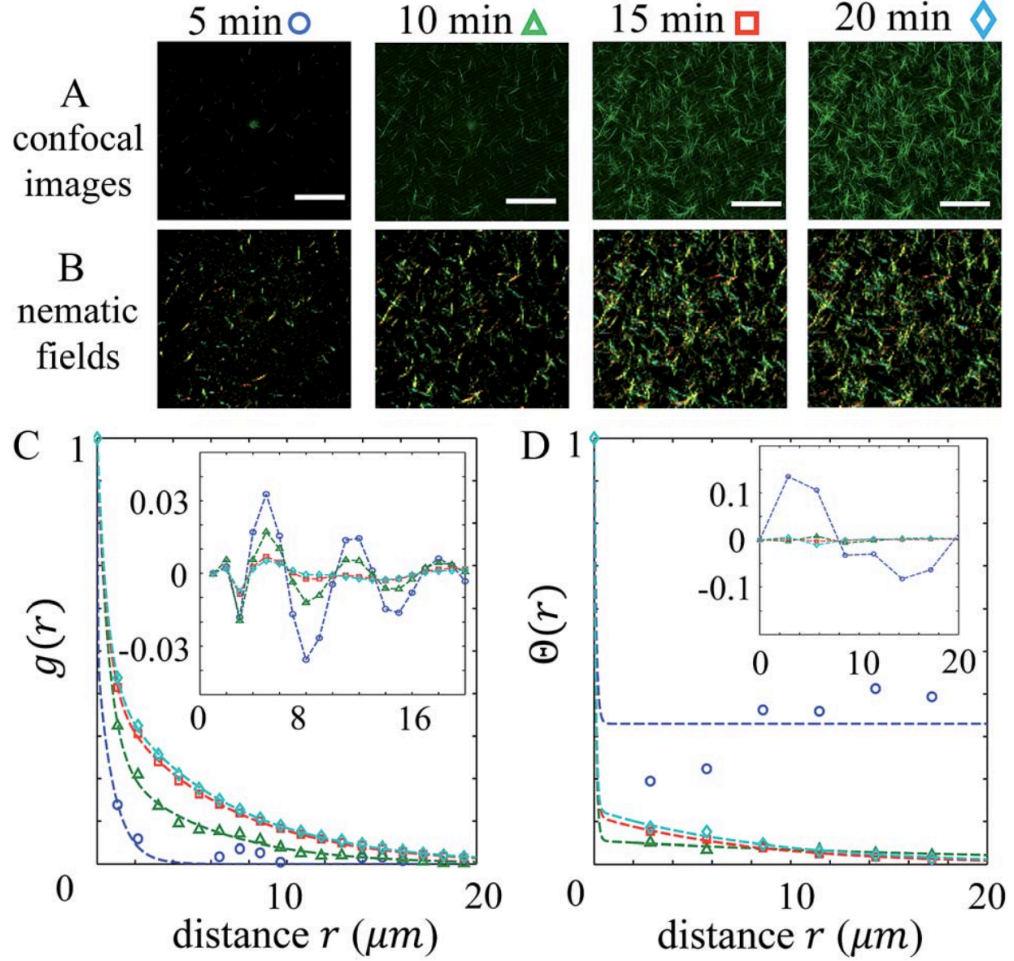
Figure 2.2: The correlation analysis reveals the typical growth dynamics of type I collagen gel. Time zero corresponds to the moment when 2 mg/mL collagen solution was neutralized and maintained in 23 ° C. (A) Time-lapse confocal images taken at 5, 10, 15, 20 minutes. Scale bars are 100 μm. (B) The corresponding nematic field obtained by template matching method. The nematic field **s** is color coded in the HSV space: the hue is proportional to the complex angle of **s** and the value is proportional to the magnitude $|\mathbf{s}|$. (C) The two-point intensity correlation function $g(r)$. Inset: the residual of fitting $g(r)$ with double exponential function. (D) The two-point nematic order correlation function, dashed lines represent double exponential fittings. Inset: the residual of double exponential fitting.

2.2D). $\Theta(r)$ can also be approximated with a double exponential function, although the geometric meaning is less obvious due to the coarse-graining.

2.2.2 Temperature Dependence of Collagen Matrix

After introducing the correlation functions to quantify the spatial fluctuation of density and nematic orders, we now study collagen gel formed at different environment temperatures T at a fixed concentration of 2 mg/mL. We made multiple gel samples for each temperature in glass bottom microwells. For each gel sample, we took a confocal z-stack starting from 10 μm above the glass bottom to avoid reflection of the glass and the z-step was set to equal the axial width of the point spread function (1.7 μm). In total for each gelation temperature we collected about 400 images in order to statistically characterize the microstructure of collagen gel.

Figure 2.3 demonstrates the density fluctuations using the 2-point correlation function $g(r)$. In Figure 2.3A, $g(r)$ curves for different temperatures are grouped by colors (blue-green-red in the order of increasing temperature) and data point markers (circle-triangle-square-diamond in the order of increasing temperature). As temperature increases, $g(r)$ decays faster, which is consistent with smaller pore sizes. Notice that the density fluctuation does not have any systematic dependence with respect to the position of focal plane, or the distance between the glass bottom and image plane, suggesting a weak boundary effect when forming the gel (Figure 2.3A, inset).

Figure 2.3B-C demonstrate the temperature dependence of the parameters a_1,
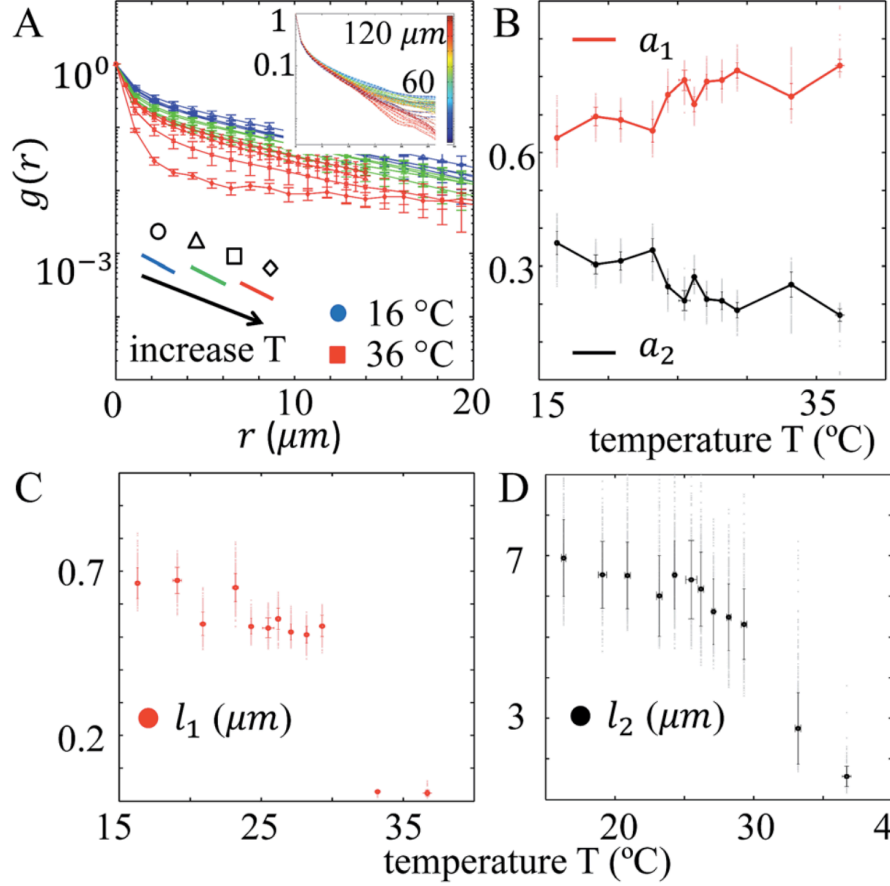
Figure 2.3: The temperature dependence of the collagen gel microstructure revealed by density correlation function $g(r)$. (A) (Log scale) Mean and standard deviation of $g(r)$ for gel formed at different temperatures and fixed concentration (2mg/mL). Each data point is calculated by sampling ~ 400 images from 6 gel samples made in the same condition. Blue circle, diamond, uptriangle.. 16.1 C. Green diamond......Inset: $g(r)$ for a typical gel sampled at different depth and plotted in the same scale of A. We take 2D slices of each gel from 10 μm to 130 μm away from the glass bottom in 1.7 μm steps (step size equals to the width of point spread function). Results for a typical sample are color coded by their relative distance from the glass bottom. (B-D) The double exponential fitting parameters a_1, a_2, l_1, l_2 for each image (dotted scattering plot), and their means and standard deviations (solid lines and error bars).

a_2, l_1, and l_2 from double exponential fitting. As temperature grows, there are more but shorter fibers, thus the weight $a_1 = 1 - a_2$ increases. The parameter l_1 slowly decreases, just above the diffraction limit ($\approx$0.4 μm) until gelation temperature is 30°C. Therefore, the faster decay of $g(r)$ at higher temperature is mainly due to the decrease of l_2. When $T > 30$°C, however, reduced fiber thickness and length, together with the increased gel turbidity lower image signal to noise ratio and greatly suppress the length scale l_1. In addition, we also find the length scale l_2 becomes less sensitive to temperature when $T < 21$°C. As we will discuss below, this can be explained if the energy barrier for fiber growth is comparable to the thermal energy at $T \sim 37$°C.

The systematic change of collagen gel microstructure with respect to temperature is also evident from the nematic orders. As shown in Figure 2.4A-B, at higher temperature, the collagen fibers are shorter and more randomly oriented. As a result, the correlation in nematic field becomes shorter ranged (Figure 2.4C). Similar to the density correlations, the nematic fields do not systematically depend on the depth of focal plane (Figure 2.4C, inset), therefore we consider images taken at different depth as statistically independent.

When orientation of collagen fibers fluctuate strongly, we expect a small global nematic order $< \mathbf{s} > = \frac{1}{N} \sum_i \mathbf{s}(\mathbf{r}_i)$, where the average is taken over all subregions that contains a line. This is evident in Figure 2.4D, where the global nematic order decreases monotonically as a function of T. The result suggests that at fixed chemical composition and collagen concentration, the gel microstructure depends on the gelation temperature in a manner that resembles ferromagnetic phase transition.
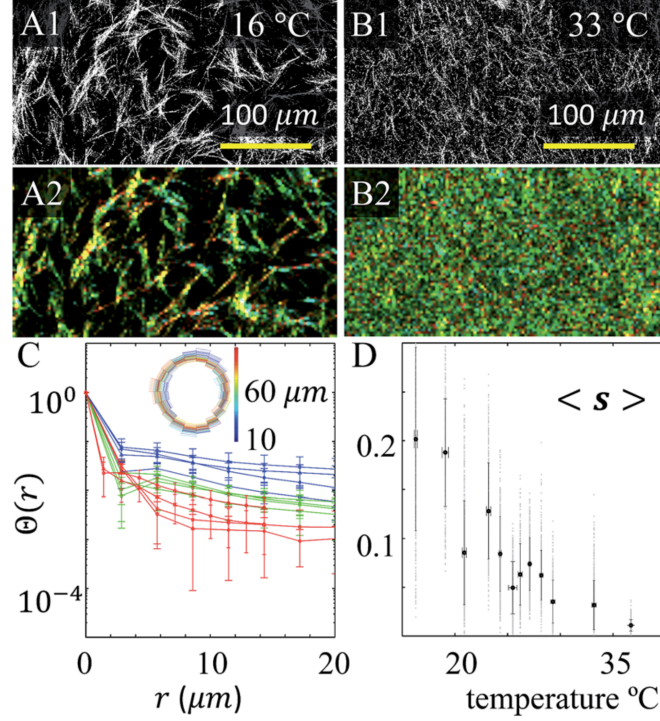
Figure 2.4: The temperature dependence of the collagen gel microstructure revealed by nematic correlation $\Theta(r)$. (A1) A typical confocal image of collagen gel formed at 16°C, converted to binary to enhance the contrast. (A2) The corresponding nematic field of the image in A1. The nematic field $\mathbf{s}$ is color coded in the HSV space: the hue is proportional to the complex angle of $\mathbf{s}$ and the value is proportional to the magnitude $|\mathbf{s}|$. (B1-B2) A typical confocal image and the associated nematic field of gel formed at 33° C. (C) (log scale) Mean and standard deviation of $\Theta(r)$ for gel formed at different temperatures and fixed concentration (2 mg/mL). Each data point is calculated by sampling $\approx$400 images from multiple gel samples made in the same condition. Legend: same as in Figure 2.3A. Inset: the angle distributions of a typical gel sampled at different focal depth (10 mm to 130 mm from the glass bottom in 1.7 mm steps). The histograms of the complex angles of $\mathbf{s}(r)$ for each slice are plotted in polar coordinate and are color coded by their relative distance from the glass bottom. (D) The magnitude of global nematic order parameter $< \mathbf{s} >$ as a function of temperature. Data presented here are the results from individual images (dotted scattering plot), their means and standard deviations (solid lines and error bars).

Indeed, as T increases, the order parameter $< \mathbf{s} >$ decreases and approaches zero continuously.

The above experiment measurements suggest that the self-assembly of collagen matrix is temperature sensitive. As the gelation temperature increases, the static microstructure of collagen gel evolves from clusters of long, aligned fibers to uniformly distributed short, and randomly oriented fibers. Interestingly, the same trend has been observed in connective tissues that are compromised by fibrosis [37]. To better understand the underlying physics that determines the self-assembled collagen ECM microstructures, we have developed a computational model to link the equilibrium gel configurations with the growth dynamics.

2.2.3   Kinetic Monte-Carlo Collagen Growth Model

To complement our experimental study of the effects of gelation temperature on the microstructure of the collagen network, we develop a kinetic Monte-Carlo method to simulate the gelation process. The goal of the kinetic MC method is not to simulate the full molecular details of each collagen fiber during the gelation process, but rather to understand, on a coarser scale, the effects of a number of controlling factors (e.g., gelation temperature) on the final structure of the collagen network. Specifically, we model each fiber as a spherocylinder, which is initially short and can grow in length due to polymerization at both ends. Two fibers can form a cross-link (corresponding to fiber entanglement in the collagen gel) if they are sufficiently close to one another. We consider the cross-linked fibers as a cluster.

Individual fibers and clusters of fibers can diffuse in the solution. The associated effective diffusion coefficients depend on the size of the fiber/cluster as well as the viscosity of the solution, which increases dramatically as the gelation proceeds [64]. We note the detailed physical interactions between the collagen monomers and the resulting complex kinetics of the association and disassociation processes are not incorporated, as they are in other first-principle and molecular dynamics models for biopolymer network self-assembly and dynamics [74, 75, 76, 77]. However, we emphasize that our meso-scale model is sufficient to reproduce the growth kinetics of the collagen gel, as we will show in the next section.

Two key parameters in our model are the nucleation rate n and fiber growth rate γ, both of which depend on the collagen concentration c and gelation temperature T. In particular, we consider that n and γ are monotonic increasing function of c and T. At low c and T, a small of number of fiber seeds have sufficient time to grow in size, diffuse around and interact with one another via hydrodynamic effects before they are cross-linked with one another. This leads to the heterogeneous "bundle" network structure. As c and T increase, more fiber seeds emerge simultaneously and grow fast, which results in a more homogeneous network structure with short fibers. For a given set of c and T, we can effectively estimate the corresponding n and γ by comparing the experimental data with simulation results.

Our simulation works as follows: Initially, n fibers seeds (short spherocylinders with aspect ratio 2) are placed in a periodic simulation box with random positions and orientations. We note that the initial aspect ratio of the fiber seed does not correspond to actual aspect ratio of a monomer, but rather makes it an anisotropic

structural unit effectively representing a fiber in the early stage of the gelation. During each discretized time (MC) step, the following events occur:

- Each fiber grows in length via elongation at the two ends of the spherocylinder. The magnitude of the elongation δL_i is given by $\delta L_i = \epsilon L_i$, where L_i is the current length of the fiber and ϵ is a random number uniformly distributed in $[0, \gamma]$.

- Each individual fiber has a translational and rotational motion, whose magnitudes are respectively denoted by $D_T^f(L_i)$ and $D_R^f(L_i)$ and are exponential functions of the fiber length L_i such that $D_T^f(L_i) \sim exp(-L_i/L_0)$ and $D_R^f(L_i) \sim exp(-L_i/L_0)$. For fibers with length $L_i < L^*$, the random translation and rotation are applied. For fibers with $L_i > L^*$, we consider that the fiber motions are biased such that two long fibers have the tendency to align with one another due to hydrodynamic effects. Specifically, the final orientation of the moved fiber is obtained by perturbing the orientation of the nearby reference long fiber.

- When two fibers are sufficiently close to one another, i.e., the distance d_f between the axis of spherocylinders is small than Δ, the fibers form a permanent cross-link with probability p_{cl}.

- A cluster of fibers can also have random translational and rotational motions, whose magnitudes D_T^c and D_R^c are generally much smaller than those of individual fibers.

The values of the simulated parameters, including the nucleation rate n and fiber growth rate γ, corresponding to various collagen concentrations and temperature values employed in experiments, will be discussed and provided in the following sections.

2.2.4 Simulated Collagen Growth Dynamics

To validate the kinetic MC method, we first employ it to simulate the growth dynamics of the collagen matrix with collagen concentration $c = 2$ mg/ml and maintained at $T = 23°$C. The model parameters are determined such that the simulated growth dynamics reproduces the experimental observations described in previous sections. In particular, we denote the edge length of the cubic simulation box by ℓ_0 and use it as the unit for length. We have used $n = 300/\ell_0^3$ for the nucleation rate, $\gamma = 0.05$ for the growth rate, $D_T^f = 0.05\ell_0$ and $D_R^f = 0.15\pi$ for fiber translation and rotation, $D_T^c = 0.001\ell_0$ and $D_R^c = 0.05\pi$ for cluster translation and rotation. The critical distance for cross-linking is $\Delta = 0.005\ell_0$ with the cross-linking probability $p_{cl} = 0.5$. The critical fiber length beyond which fiber rotations are biased due to hydrodynamics effects is chosen to be $L^* = 0.25\ell_0$.

Figure 2.5A shows the snapshots of simulated growing collagen network in three dimensions at different MC steps after initialization. The specific MC steps selected are to match the corresponding snapshots of the experimental system shown in Figure 2.2A. To make quantitative comparison with experimental data, we generate 2D gray scale images by convolving the 3D (binary) network with a
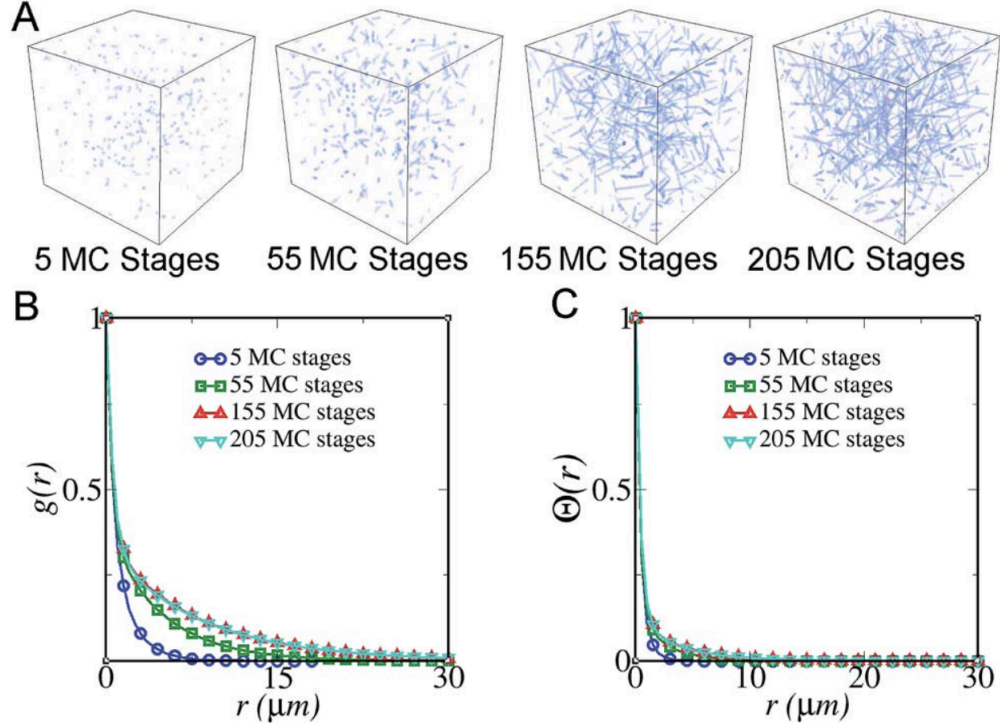
Figure 2.5: The simulated growth dynamics of the collagen matrix at gelation temperature $T = 23^oC$. (A) Snapshots of simulated 3D collage network at different MC stages. (B) Two-point intensity correlation function associated with the simulated collagen matrix at different MC stages. (C) Nematic correlation functions associated with the simulated collagen matrix at different MC stages

point spread function represented as a Gaussian kernel. The width of the kernel is chosen to be $\sigma = 1.0\mu$m, which produces reasonably smeared images that mimic the experimental data. It is well established in heterogeneous material theory [73] that if a system is statistically homogeneous and isotropic, the two-point statistics computed from 2D slices of the material are representative of the full 3D structure. On the other hand, although the nematic correlation functions $\Theta(r)$ have different definitions in 2D and 3D systems, they both represent the degree of alignment

between the fibers, and therefore will share the same trend as gelation temperature varies. Thus, it is valid to compare the 3D simulation results and 2D experimental data.

Figure 2.5B shows the two-point intensity correlation $g_{(}r)$ at different gelation times (i.e., MC stages). The simulated density correlation functions can also be fitted very well with double exponential functions, i.e., $f(r) = a_1 \exp(-r/l_1) + a_2 \exp(-r/l_2)$. Similar to the experimental data, both l_1 and l_2 increase as gelation proceeds. The simulated nematic correlation function $\Theta(r)$ also possesses a growing length scale, which again is consistent with the experimental data. The agreement between the simulation and experimental results clearly demonstrates the validity and utility of kinetic Monte-Carlo growth model in modeling the collagen matrix.

2.2.5 Simulated Collagen Temperature Dependence

After validating the kinetic MC method with experiments, we now apply the simulations to better understand the observed temperature dependence of collagen matrix. In particular, we propose the following scenario for the experimental observation: At low gelation temperature T, the fiber nucleation rate is low. Thus, a small of number of fiber seeds (small nucleation rate) have sufficient time to grow in size, diffuse around and interact with one another before they are cross-linked with one another. At the point of cross-linking, the near-neighbor long fibers have developed a high level of orientational correlation (i.e., the tendency to be aligned with one another) due to hydrodynamic effects. This will lead to a heterogeneous

network full of clusters of fibers. At high gelation temperature T, many fiber seeds emerge simultaneously due to the high nucleation rate. In addition, the growth rate is also higher. In this case, a percolating network quickly forms because cross-linking occurs before significant orientational ordering can be achieved. This results in a homogeneous network structure with short fibers.

In order to verify the proposed scenario, we employ kinetic Monte-Carlo simulations and use least mean square fittings to search for the optimized set of n and γ at each temperature so that the density correlation function $g(r)$ of simulated network best matches the corresponding experimental data. This allows us to obtain the temperature dependence of the nucleation rate and growth rate, which we will elaborate on below.

Figure 2.6A shows the snapshots of the 3D collagen network corresponding to different temperatures. It can be clearly seen that as the gelation temperature increases, the network structure becomes more homogeneous, composed of shorter fibers with less orientational correlation. Also shown are the intensity correlation function $g(r)$ (Figure 2.6B) and the nematic correlation function $\Theta(r)$ (Figure 2.6C).

The double-exponential fitting parameters (a_1, a_2, l_1 and l_2) and the global nematic order parameter $< \mathbf{s} >$ as a function of temperature are shown in Figure 2.7A-D. Similar to the experimental results, the length scales in g and Θ decrease as T increase, indicating a decrease in the degree of spatial and orientational correlation between the fibers in the network. In addition, for the intensity correlation function g, the weighting parameter a_1 increases with increasing T while a_2 de-
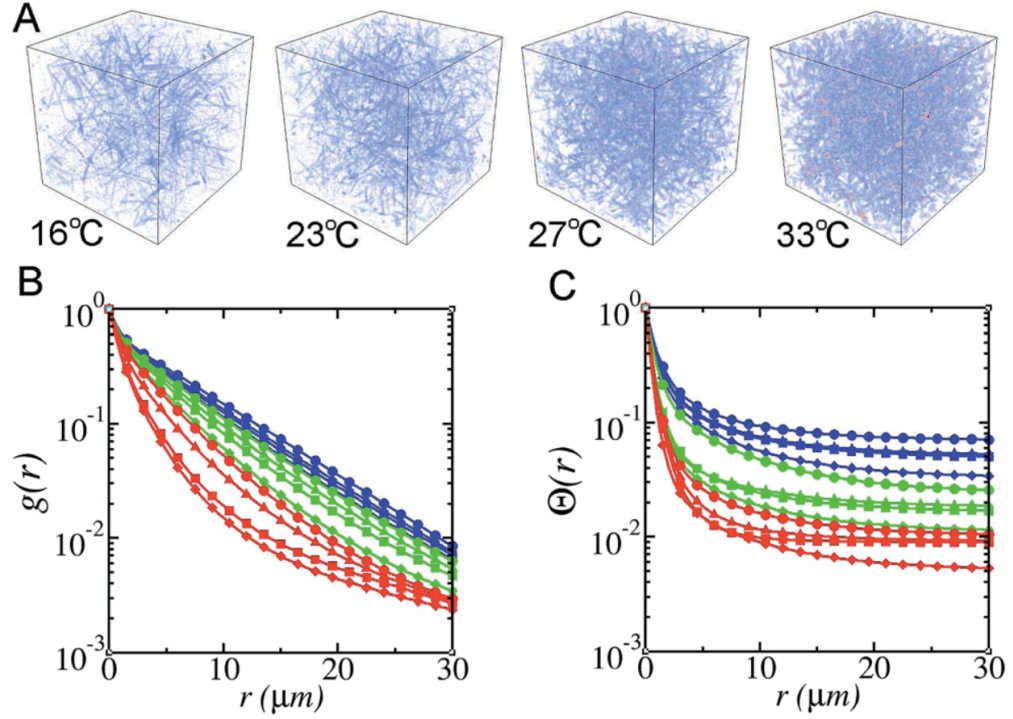
Figure 2.6: Effects of temperature on the collagen network via simulation. (A) Snapshots of simulated 3D collagen networks formed at different gelation temperatures. (B) Two-point intensity correlation functions corresponding to different collagen networks. (C) Nematic correlation functions corresponding to different collagen networks. The color scheme and symbols for different temperatures are the same as in Figure 2.3.

creases, indicating a decay of short-range correlation (e.g., that between bundles of fibers), which is consistent with experimental observations. Finally, the simulated nematic order parameter $< \mathbf{s} >$ decreases with temperature and almost vanishes at $36°C$, suggesting a continuous phase transition at the vicinity of this temperature. The good agreements between simulation and experimental results strongly support our proposed mechanisms for the temperature dependence of collagen network

microstructures.
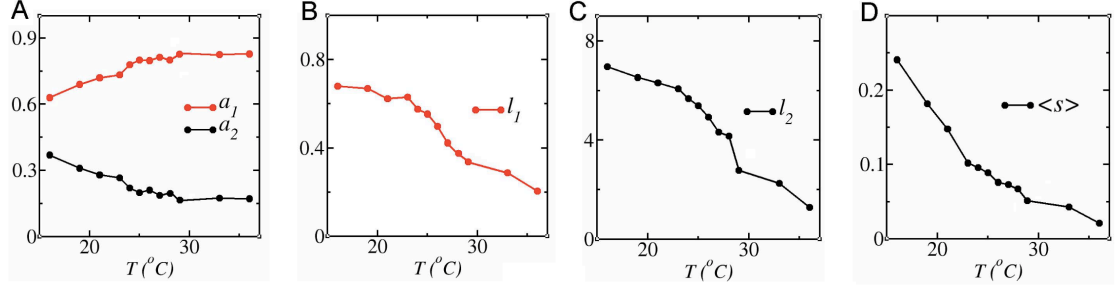
Figure 2.7: The effect of gelation temperature T on the simulated fitting parameters a_1, a_2, l_1 and l_2 for $g(r)$ as well as the global nematic order parameter $< \mathbf{s} >$.

Our kinetic MC model also provides further insights on the temperature dependence of the parameters n and γ, which govern the gelation kinetics as well as the static microstructure. As shown in Figure 2.8, the nucleation rate exhibits an exponential dependence on the gelation temperature,

$$n = A_1 exp[-A_2/(T - A_3)] \tag{2.3}$$

where $A_1 = 2223\ell^{-3}$ is a scaling parameter and $A_2 = 11.6°C$ is an effective nucleation barrier, which could depend on the chemical composition and concentration of the collagen, and $A_3 = 13.2°C$. This functional form is consistent with the prediction from classic nucleation theory [72]. Similarly, the growth rate also exhibits an exponential albeit weaker dependence on T, as shown in Figure 2.5B,

$$\gamma = B_1 exp[-B_2/(T - B_3)] \tag{2.4}$$

where $B_1 = 0.12$, $B_2 = 8.93°C$, and $B_3 = 10.6°C$. This suggests that it is energetically favorable to elongate an existing fiber rather than creating a new one. As a result, the microstructure of collagen based ECM is more heterogeneous when formed at lower temperature.
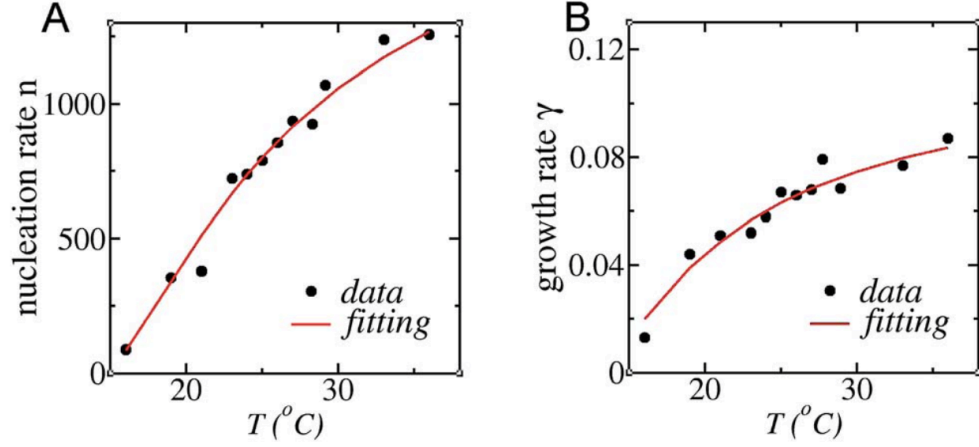
Figure 2.8: Effects of temperature on the nucleation rate n (A) and growth rate γ as obtained from simulation (B). Both parameters exhibit an exponential dependence on the gelation temperature.

2.3   Discussion

In this article, we report the correlation-based microstructure characterization of collagen gel over a broad range of gelation temperatures. The two point correlation function $g(r)$ characterizes the spatial fluctuation of collagen fiber density, and can be further parameterized to obtain fiber thickness as well as fiber cluster sizes. We have demonstrated that as temperature increases, collagen fibers become shorter and form smaller clusters, resulting in a faster decay of the density correlations.

The result is consistent with smaller pore sizes at higher temperature, which has also been observed for collagen gel formed at higher concentration [17, 43].

In order to obtain the orientations of collagen fibers, we have developed a template-matching algorithm to calculate the coarse-gained nematic field directly from confocal reflection images. We have demonstrated that as temperature increases, the global nematic order decreases and $\Theta(r)$, the spatial correlation of nematic field also decays faster. This means that increasing temperature will lead to be more randomly oriented fibers, and the local structure becomes more isotropic.

The correlation-based microstructure characterization presented here provides more detailed information than the global characterizations, such as pore size distribution [43]. However, neither the correlation functions, nor the pore size distribution uniquely determine the configuration of a collagen fiber network. Inspired by the close relation between growth dynamics and the equilibrium structures [18, 45, 78], we have developed a kinetic Monte-Carlo model based on the experiment measurements to simulate the growth dynamics of a collagen gel at specific gelation temperatures. Our model is validated by successfully reproducing the entire growth kinetics of collagen gel and suggests that the static structure of collagen gel is inherently connected with the growth kinetics. With our model, we showed that the nucleation rate, growth rate, and an effective hydrodynamic alignment of collagen fibers fully determines the spatiotemporal fluctuations of the density and orientational order of the collagen gel microstructure. Our model also enables us to determine the temperature dependence of the nucleation rate and growth rate, which are difficult to directly measure in experiments.

The structure of collagen gel determines the mechanical and transport properties of the fibrous ECM [16, 19], both of which are key to the collagen-based tissue engineering [61, 79]. It is therefore of great interest to study the quantitative relations between microstructure characterization, the permeability, and rheology properties of collagen gel. The microstructures of collagen ECM in physiological settings are also closely related with the disease states of connective tissue. For instance, the shorter and less oriented fibers we observed at higher temperature resembles the collagen contracture in fibrosis [37]; longer and oriented collagen fibers have been recently shown to promote invasive transition of mammary acini [34]. These observations suggest an interesting future direction to apply our experiment characterization and simulation model to *in vivo* systems. In addition, our combined experimental and numerical study suggests that the gel microstructure can be tuned in a controllable fashion by varying a few environmental parameters. This would enable one to produce engineered gel structures for guided cellular behaviors.

2.4   Materials and Methods

2.4.1   Preparing Collagen Gel

Gels were prepared from high-concentration rat tail collagen I in acetic acid (Corning, 10.08 mg/ml). The collagen was diluted with dH$_2$O, 10×PBS (phosphate buffered saline), and 0.1 N NaOH to a final concentration of 2 mg/ml and a pH of

7.4. The temperature at which the collagen gel formed was regulated using a stage top incubator (ibidi Heating System, Universal Fit) equipped with an external temperature sensor (themo-couple type K). The temperature was set 30-60 minutes prior to the addition of collagen to allow the incubator to equilibrate. Preparation of the collagen solution was carried out on ice to prevent early gelation and two different methods were used to add the solution to the incubator.

The first method was used for experiments on the collagen growth dynamics in which imaging must begin immediately after the addition of collagen. Less than 60 seconds after neutralizing the collagen, the solution was injected through plastic tubing (Tygon S-54-HL, 0.04" ID) onto a glass bottom dish (ibidi μ-dish 35 mm) positioned above the microscope objective. Use of the plastic tube allows the collagen to be placed in the incubator without removing the lid and preserves the thermal equilibrium.

The second method was used for experiments on the temperature dependence of gel formation in which multiple gel samples were prepared at the same temperature from the same collagen solution. An 8 well μ-slide (ibidi) was placed in the incubator during equilibration with one of the wells containing the external temperature sensor. For gel formation below 23° C, the incubator was placed in a 4° C refrigerator, and for temperatures of 23° and above, the incubator was located on the lab bench at room temperature. After neutralizing the collagen solution, the lid of the incubator was removed and the remaining 7 wells were filled with collagen. The time elapsed between neutralization and replacement of the incubator lid varied between samples but was always less than 3 minutes. Removal of

the lid and addition of a larger total volume of collagen temporarly disrupts the thermal equilibrium of the system so the temperature was monitored closely via a thermo sensor in contact with the microwells next to the gel sample. Typical temperature versus time curves for these experiments are provided in Figure 2.9. After the initial temperature drop due to the storage temperature of reagents, our setup maintained the gelation temperature within $0.3°$ C. Collagen samples were given at least one hour to fully gel before imaging.
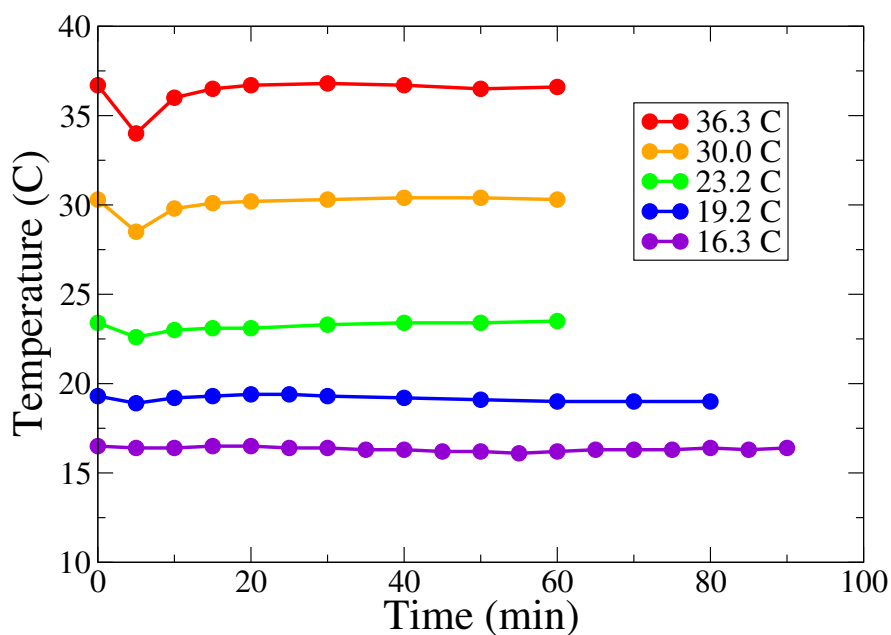
Figure 2.9: Typical temperature versus time recordings during gelation of collagen samples. For most samples there is an initial decrease in the temperature due to the brief removal of the incubator lid. Sample temperature returns to the initial value within 10-15 minutes and then fluctuates by less than $0.3°$ C.

2.4.2 Microscopy

Confocal reflection microscopy images of the collagen gels were taken using an inverted laser scanning confocal microscope (LSCM, Leica TCS SPE) with a 20× oil immersion objective. Samples were illuminated with a 532 nm laser and reflected light passed through a 30/70 RT filter and confocal pinhole before being collected by a photomultiplier tube detector (PMT). The scan size was 1024×1024 pixels (367μm×367μm) and reflected light intensity was collected as 8-bit gray scale images.

For imaging collagen growth dynamics, the microscope was equipped with an on stage incubator and the system was allowed at least 30 minutes for the temperature to equilibrate. Prior to the adding the collagen, the focal plane was set to the top surface of the glass μ-dish. The collagen was then injected into the incubator through a plastic tube such that the solution filled the area of the μ-dish directly above the objective. Immediately after addition of the collagen, the focal plane was moved approximately 50 μm into the sample and images were taken at one scan per second for 40-60 minutes. The time elapsed between collagen neutralization and the first scan was less than 1 minute 30 seconds. For multi-well collagen samples, one confocal z-stack was taken for each well with the first scan ≈10 μm above the glass to avoid reflection interference. 100 scans were taken per well with a 1 μm z-step size between each scan.

2.4.3 Calculating Nematic Field by Template-Matching Method

To calculate the nematic order of a test image, we have developed a template-matching method which includes three consecutive steps:

First, a series of template images with the same pixel resolution as the test image are generated. Each template image contains one line described by the equation $x \sin \theta - y \cos \theta = b$ where the origin of coordinate system is set at the center of the template image. For a pixel whose distance is d from the line $x \sin \theta - y \cos \theta = b$, the intensity is set to be $e^{-\frac{d^2}{\sigma^2}}$, where $\sigma = 0.5$ pixel. For the 8 x 8 test images used in this study, we have generated 1800 templates $D_{b,\theta}(i,j)$ for $b \in [-2, 2]$ (in step of 0.5 pixel) and $\theta \in [0, 180)$ (in step of 1 degree).

Next, we calculate the similarity score $R(b, \theta)$ between the test image $T(i, j)$ and the template images $D_{b,\theta}(i,j)$ as

$$R(b, \theta) = \frac{\sum_{i,j} T(i,j) * D_{b,\theta}(i,j)}{I(i,j) * D_{b,\theta}(i,j)} \tag{2.5}$$

here $I(i, j)$ is a matrix whose elements are all ones'.

Finally, the nematic order $\mathbf{s}$ for the test image is calculated as

$$\mathbf{s} = \sum_{\theta} R(b, \theta) e^{2i\theta} \tag{2.6}$$

For a typical confocal image with pixel resolution 1024 x 1024, we divide it into 128 x 128 subregions, with each subregion being a 8 x 8 test image. The template-matching is applied to each subregion and collected to construct the coarse-gained

nematic field $\mathbf{s}(\mathbf{r})$.

3 Micromechanics of Cellularized Biopolymer Networks

In this chapter we study the mechanics of type I collagen on the scale of tens to hundreds of microns by using holographic optical tweezers (HOT). We demonstrate that contracting cells remodel the micromechanics of their surrounding extracellular matrix and have constructed a computational model which reproduces the main experimental findings.

This work was published in the *Proceedings of the National Academy of Sciences* [80]. Christopher Jones contributed to the experimental portion of this work by preparing all samples, collecting, and analyzing data. Matt Cibula, in Professor David McIntyre's lab, developed the HOT system and contributed equally to micromechanical data acquisition and analysis. Emma Krnacik aided actin staining and confocal microscopy. Jingchen Feng in Professor Herbert Levines group at Rice University developed the computational models.

3.1 Introduction

The mechanical properties of the extracellular matrix (ECM) play a central role in developmental biology [81], tissue homeostasis and remodeling [61]. Alteration of the ECM elasticity is a signature of many diseases such as pulmonary and atrial fibrosis, Ehlers-Danlos syndrome, and infantile cortical hyperostosis [36, 59]. The

mechanical cues from the ECM also strongly correlate with the clinical prognosis of various types of cancers [31].

In recent years, many studies have shown that to mimic the physiological conditions *in vitro*, mechanical cues from a truly 3D ECM are necessary [82]. Type I collagen gel has gained popularity as arguably the most employed *in vitro* model of a 3D ECM [61]. As the most abundant protein in animal tissue, and accounting for 25% of the human whole-body protein content [58], type I collagen is a major component of the ECM in skin, tendon and organs. Despite its lack of biochemical complexity compared with live tissue, reconstituted type I collagen gel has been successfully employed to provide mechanistic insights into processes such as morphogenesis [83], wound repair [84] and cell migration [85]. In particular, the rheology and especially the rigidity of collagen gel have been shown to tune the growth and migratory phenotypes of cancer cells *in vitro* [26, 32].

Structurally, collagen gels are formed by fibrous networks, and typically have pore sizes of a few to tens of microns [17, 40, 43]. The typical size of these structural discontinuities is comparable to the size of cells and is much larger than cell-ECM adhesion complexes [86, 87]. It is therefore expected that a cell senses the micromechanical properties of its surrounding matrix, rather than the macroscopic rheology of the ECM [29, 87]. While many studies have focused on the (nonlinear) bulk rheology of empty and cellularized collagen ECM [20, 44, 69, 70], the micromechanics of the porous biopolymer network is largely unexplored, presumably due to the lack of direct experimental measurements.

In this chapter, we report direct experimental measurements and computational

models on the mechanical response of empty and cellularized type I collagen gel of different architectures. Previously we have demonstrated that as the gelation temperature increases, the resulting collagen gel experiences a phase transition from highly heterogeneous long fiber clusters to homogeneously distributed short fiber mesh [57]. As we demonstrate, the microscopic architecture strongly affects the micromechanics of the collagen gel. Furthermore, we study the effects of embedded fibroblast cells and breast cancer cells on the micromechanics of collagen fiber networks. These experimental measurements have led us to develop a computational model of realistic biopolymer networks. Our results provide a largely overlooked perspective on the studies of 3D cell-ECM mechanical interactions.

3.2   Results

3.2.1   Micromechanics of Collagen Gel

To measure the micromechanical response of the collagen gel, we apply optical forces to 3-μm-diameter polystyrene beads embedded in the gel and record the resulting motion with holographic video microscopy. We use a computer-controlled spatial light modulator to manipulate the laser beam (1064 nm wavelength) and displace the optical trap away from the equilibrium position of the embedded particle [88]. We turn the optical trap on and off using an external shutter while recording video microscopy of the bead's motion. The beads are illuminated with a partially coherent light source at 625 nm, which generates concentric diffraction

patterns that allow us to track the particle trajectories at high resolution [89, 90].

Figure 3.1A shows a confocal reflection microscopy (CRM [38, 57]) image of a bead embedded in a collagen gel (prepared at room temperature, see Material and Methods) and the inset shows one frame of the transmitted light video microscopy for the same bead. We analyze each video frame to obtain a time series of the bead's mechanical response in two dimensions, as shown in Figure 3.1B. In this case, the particle is manipulated by displacing the optical trap 0.725 μm in the $+x$ direction relative to the equilibrium position of the particle. This time series illustrates several features of our system and of the collagen mechanical response: particle displacements are determined with sub 10-nm resolution, particle displacement has components parallel and perpendicular to the direction of the trap displacement, and the residual motion during the displaced (trap on) times is smaller than the residual motion during the equilibrium (trap off) times, indicating that the trap suppresses the particle's Brownian motion.

To complete our characterization of the micromechanical response of an embedded bead, we repeat the above measurements with the optical trap displaced in the $-x$, $+y$, and $-y$ directions in the image plane. The collected results for the four directions are shown in Figure 3.1C, where each dot represents data from one video frame. Most frames correspond to either the displaced case (trap on) or the equilibrium case (trap off), but some frames do record transition states in between. By fitting the time series to a pulse function, we reduce the influence of these transition states with the result that each video yields one data point representing the mean displacement of the particle from its equilibrium position.
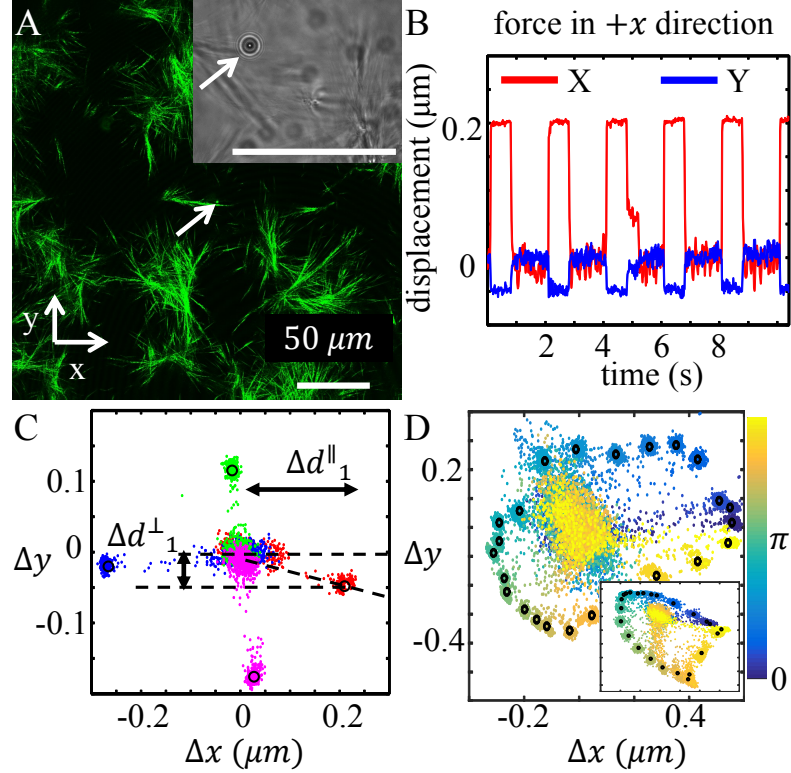
Figure 3.1: A typical micromechanical measurement of collagen gel. (A) Confocal reflectance image of a 3-μm-diameter particle embedded in a collagen matrix. The collagen gel was formed at 21 °C and featured distinct fiber clusters dispersed in a fluid medium. The inset shows one frame of the video used to track the particle displacement. (B) Time series showing the particle displacement in response to a pulsed 22 pN/μm optical trap placed 0.725 μm away from the particle equilibrium position in the +x-direction. (C) 2D trajectory map of the particle response to optical traps positioned 0.725 μm away (from the particle equilibrium position) in the +x (red), +y (green), −x (blue), and −y (pink) directions. The circles represent the mean displacements determined by fits of the time series to a pulse function. (D) 2D trajectory map of a particle response to optical traps positioned in 24 evenly distributed orientations. Inset: 2D trajectory map of another particle in the same sample. These measurements are done in the same way as in (C) except for more directions probed instead of only four. Colors of the particle trajectories represent the orientations of the trap positions.

The displacement $\Delta\mathbf{d}$ includes components both parallel and perpendicular to the trap displacement. The data for this particle illustrate that the response of the collagen gel is off-axis, anisotropic, and asymmetric. As shown in Figure 3.1D, these features are not a result of particular choice of measurement axis, but indeed represent the complex micromechanical properties of the collagen network.

We repeat the measurements described in Figure 3.1A-C for $\approx$100 particles in each collagen gel sample. The particles are seeded at a density of $\approx 2 \times 10^5 mm^{-3}$ and all measured particles are within a 200 x 150 x 20 μm^3 volume. The particle density is chosen to minimize particle aggregation and disruption of the native gel structure, while still offering high resolution of the spatial variations of the network micromechanics.

To characterize the distribution of micromechanical properties in each gel sample, we define three quantities that summarize the results. For a given particle and trap location, we define the compliance J_i as

$$J_i = 6\pi a \frac{\Delta d_i^{\parallel}}{F_i^{\parallel}} \qquad (3.1)$$

where $i = 1 - 4$ refers to one of the four trap locations, $a = 1.5$ μm is the particle radius, $\Delta d_i^{\parallel}$ is the component of the particle displacement along the direction of the trap displacement, $F_i^{\parallel} = k_t(d_t - \Delta d_i^{\parallel})$ is the parallel component of the applied force, $k_t \approx 22$ pN/μm is the harmonic optical trap stiffness, and $d_t = 0.725$ μm is the distance of the trap from the particle's equilibrium position. The average of

the four measurements gives the local compliance:

$$J = \frac{1}{4} \sum_i J_i \tag{3.2}$$

For a linear elastic material, this definition reduces to the standard definition of compliance, which is the inverse of the shear modulus.

To quantify the anisotropic response, we define the anisotropy A as the dimensionless quantity

$$A = \frac{1}{4J}(\text{Max}[J_i] - \text{Min}[J_i]). \tag{3.3}$$

To quantify the off-axis response of the particles to the applied forces, we define the directional off-axis angle

$$\theta_i = tan^{-1}\left(\frac{\Delta d_i^{\perp}}{\Delta d_i^{\parallel}}\right) \tag{3.4}$$

where positive angles are measured counterclockwise from the trap displacement to the particle displacement. We also define the off-axis angle for a given particle to be the maximum of its directional off-axis angles.

$$\theta = \text{Max}[|\theta_i|] \tag{3.5}$$

In order to investigate the effect of network architecture on collagen gel micromechanics, we examine two types of collagen gels prepared under different con-

ditions: one with collagen concentration of 1.5 mg/ml and grown at 37°C, the other with the same concentration but grown at 21°C with increased ionic strength. Figure 3.2 shows the representative results for one gel of each type. Sample to sample variations do not change the qualitative behaviors reported below. Consistent with our previous results [57], different gelation temperatures lead to visible differences in the microstructure of the collagen fiber network, as seen in Figure 3.2A. At 37°C, the collagen network is composed of short and thin fibers that form a nearly homogeneous mesh with a typical pore size of $\sim 1\mu$m. At 21°C, the collagen gel contains thick fiber clusters and the gaps between fiber clusters are on the order of tens of microns.

These structural differences cause the two gels to have significantly different micromechanical properties. Figure 3.2B shows normalized histograms (probability distribution) for the local compliance J of the two gels. The gel formed at 37°C has a compliance J that is narrowly distributed around the average value. The gel formed at 21°C, in contrast, has a broadly distributed local compliance.

In addition to the compliance J, the anisotropy of the local mechanical response also exhibits a systematic dependence on the collagen network architecture. As shown in Figure 3.2C, the distribution of the anisotropy A peaks at 0.1 for gels formed at 37°C. For 21°C gels, the anisotropy peaks around 0.18, and may take extreme values as high as 0.5. For both gels, the directions of maximum (or minimum) compliance are evenly distributed among $\pm\hat{\mathbf{x}}$, $\pm\hat{\mathbf{y}}$, suggesting that the gels are macroscopically isotropic random networks. Note that in our definition, an anisotropy of 0.5 means the compliance measured locally along different directions
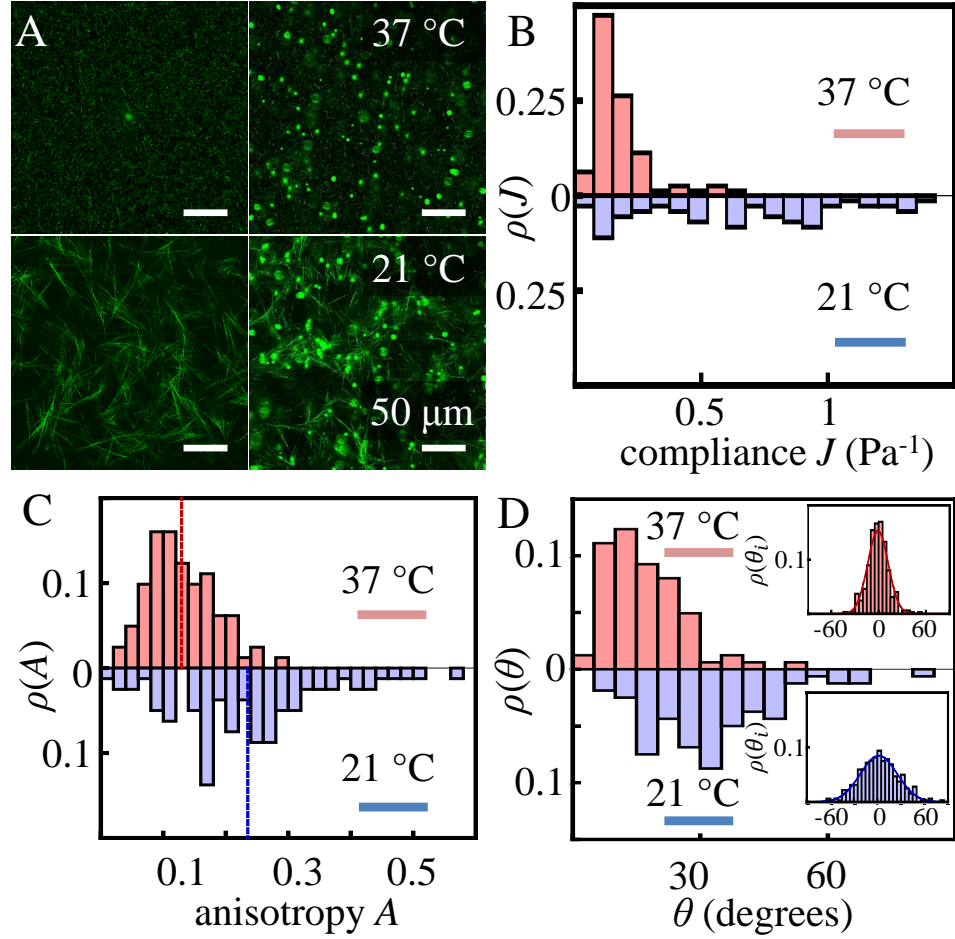
Figure 3.2: Statistical distributions of micromechanical properties. (A) Confocal reflection images of 1.5 mg/mL collagen gels grown at 37°C and 21°C, with (right) and without (left) the embedded probing particles. (B) Normalized histograms $\rho(J)$ of compliance J for collagen gels grown at 37°C (upper panel, red) and 21°C (lower panel, blue). (C) Normalized histograms $\rho(A)$ of anisotropy A for collagen gels grown at 37°C and 21°C. Gels formed at 37°C are more isotropic (D) Normalized histograms $\rho(\theta)$ of off-axis angles θ for collagen gels grown at 37°C and 21°C. The inset shows normalized histograms $\rho(\theta_i)$ of directional off-axis angles θ_i. $\rho(\theta_i)$ are fit well by a normal distributions (mean and standard deviation: $\mu_{37}^\theta = -1.39°$, $\sigma_{37}^\theta = 11.2°$; $\mu_{21}^\theta = 0.64°$, $\sigma_{21}^\theta = 23.6°$).

may differ by twice as much as the average. Also note that because we are measuring displacement in only four directions, A is a lower bound of the compliance anisotropy. As a result, the large discrepancies between compliances measured in different directions further demonstrate the rich micromechanical properties beyond the expectations for a continuous elastic medium.

When probing an isotropic random biopolymer network at scales much larger than its structure discontinuity, we expect the mechanical response to be parallel to the probing force, or $\theta = 0$. This is no longer true in the case of micromechanics. As shown in Figure 3.2D, for gels formed at 37°C, the off-axis angles tend to be smaller, the distribution peaks around 10 degrees and has a tail extending to more than 30 degrees. For gels formed at 21°C, the off-axis angles tend to be greater. The distribution peaks at 30 degrees and broadly covers the range from 0 to extreme values as high as 70 degrees. Unlike θ, the probability distributions of θ_i are symmetric and well approximated by normal distributions, as shown in the inset of Figure 3.2D. A surprising observation revealed by Figure 3.2D is that there is a significant fraction of probes with off-axis displacements larger than on-axis displacements ($\theta > 45$ degrees), suggesting that the ECM may be locally auxetic. Since many types of cells have mechanosensitive membrane receptors that are sensitive to shear stress [91], a large off-axis angle means the cellular contraction force in the normal direction may activate these shear-sensing receptors as well. To our knowledge this is a new type of mechano-feedback between cells and their ECM. Further investigation is necessary to uncover its implications to the 3D cellular dynamics. Another interesting observation by comparing Figure

3.2C and Figure 3.2D is that the shapes of the distribution functions for A and θ are similar. The normalized correlation coefficients between A and θ are higher than 0.4 for both types of gels, suggesting that micromechanical anisotropy and off-axis response in collagen are closely related. On the other hand, neither A nor θ is strongly correlated with the local compliance J (correlation coefficients <0.1 for both types of gels). These results suggest that A and θ are good measures of the geometric configuration of the ECM network, while J is mainly determined by the elastic modulus of fibers and their cross-links.

In addition, we also test gels formed with growth medium at 37°C which lead to structural and mechanical properties different from either of the conditions described previously. The characterization of these conditions are particularly relevant because all cell-populated collagen samples are prepared with growth medium at 37°C. Figure 3.3A shows confocal reflection images of two gels, one with and one without particles. Structurally, the collagen network has longer fibers than the high temperature DI water samples, but the fibers are still much shorter and more homogeneous than the low temperature gels. Figure 3.3B-D show the results of micromechanical measurements, and again the properties are in between those of the previously described collagen samples. We see broader distributions and overall higher compliance, anisotropy, and off-axis angle than for the DI water sample. It has been shown that in addition to temperature and pH, ionic strength during gelation also has a large effect on the structural and bulk mechanical properties of collagen gel [92]. Our results show higher similarity between gels prepared with growth medium at different temperature than those prepared at the same temper-
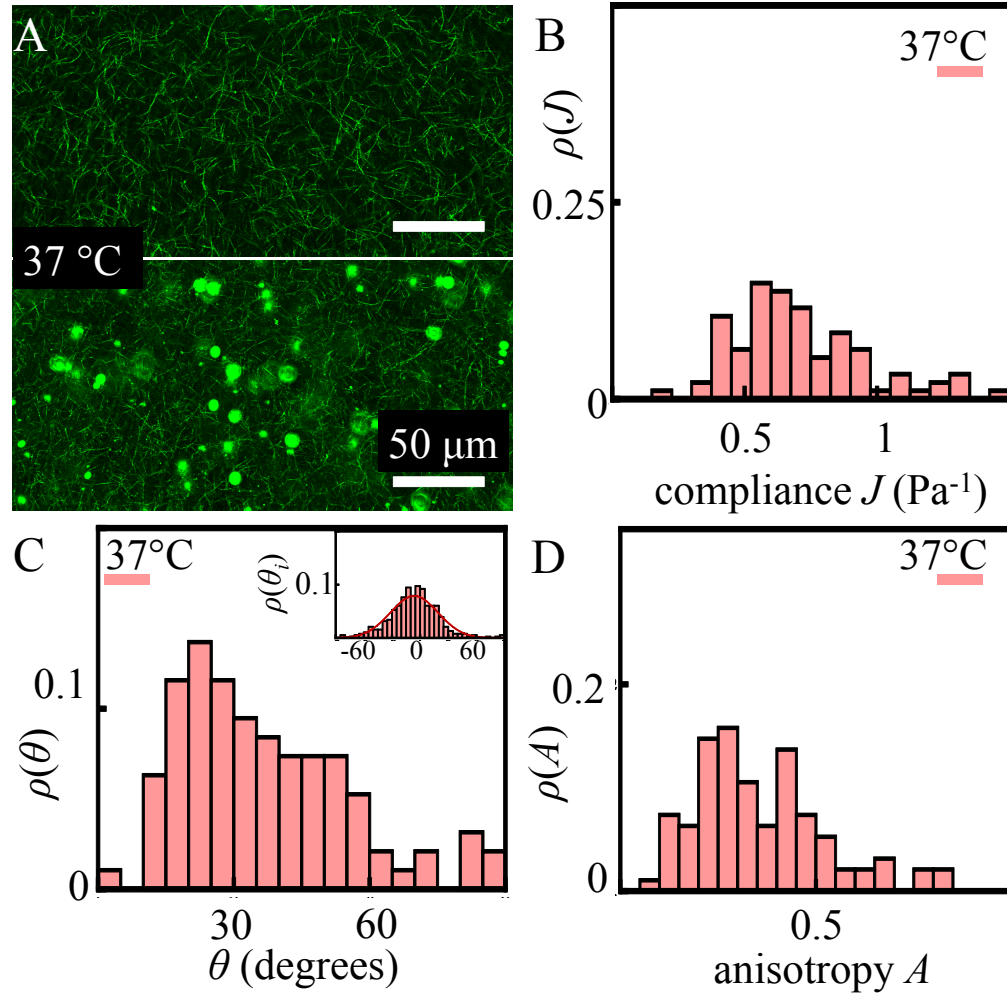
Figure 3.3: A typical micromechanical measurement of collagen gel prepared at 37°C in growth medium at a concentration of 1.5 mg/ml. (A) Confocal reflectance image of two gels. Top gel is prepared without particles, bottom is prepared with 3 μm diameter particles. (B) Normalized histogram for compliance J. (C) Normalized histogram for maximum off-axis angle θ. Inset shows histogram of directional off-axis angles θ_i for measurements in all four directions. (D) Normalized histogram for anisotropy A.

ature with different solvents. This suggests that ionic strength during gelation also has a strong effect on the local micromechanics of collagen gel.

To further investigate the spatial fluctuations of the micromechanical properties of collagen gel, we generate spatial maps of J, A, and θ with a Gaussian kernel. For each gel, we use particles within a 10 μm range in z direction to generate spatial maps using Gaussian weighted averages:

$$U(x,y) = < exp(-\frac{(x-x^i)^2 + (y-y^i)^2}{2\sigma^2} U^i >$$

(3.6)

where x^i, y^i represent the position of probing particle i, U^i represents one of the micromechanical properties (J, A or θ) measured for particle i, and $\sigma = 10\mu$m. Fig. 3.4 compares the spatial maps for gels formed at 37°C and 21°C. Due to the finite density of probing particles, these maps are low-pass-filtered representations of the spatial distributions. Nonetheless, it is evident that gels formed at lower temperature have greater spatial variations compared with gels formed at higher temperature. Also note that the anisotropy A and the off-axis angle θ are spatially correlated.

3.2.2   Cell Traction Forces Alter ECM Micromechanics

When the collagen matrix is populated by cells, the cellular traction forces may deform the local network microstructures. Therefore we expect the micromechanical properties of a cellularized collagen gel to be remodeled by embedded cells
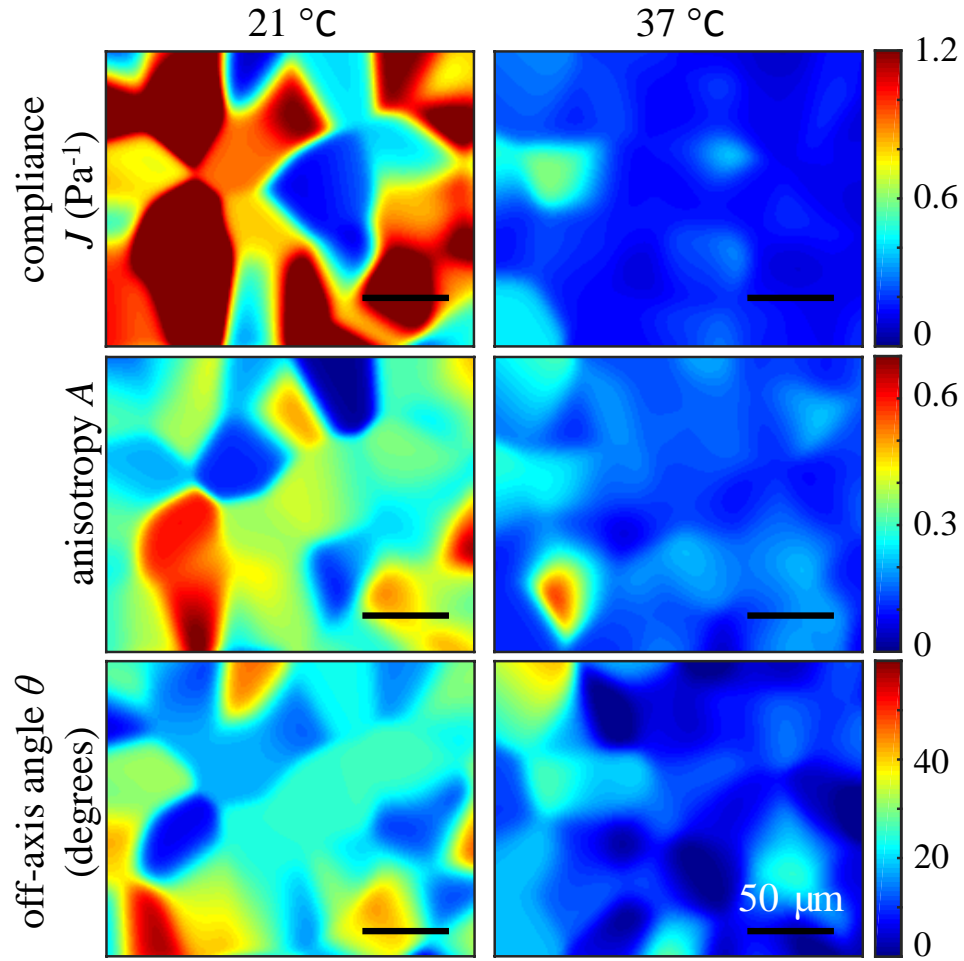
Figure 3.4: Spatial maps of compliance (top), anisotropy (middle), and off-axis angle (bottom) of collagen networks grown at 21°C (left side) and 37°C (right side). Scale bar is 50 μm. The value at the location of each particle is fixed and the region between particles is interpolated using a Gaussian kernel as a function of the distance from each particle. Gels formed at 21°C network demonstrate greater spatial fluctuations of all three micromechanical properties.

[54, 93, 94]. To test this hypothesis, we seed strongly contracting mesenchymal cells (mouse fibroblast cells NIH 3T3 and human breast cancer cells MDA-MB-231) in the collagen matrix at low density and measure the micromechanical response around a single isolated cell. Figure 3.5A shows the actin cytoskeleton of a MDA-MB-231 cell in a 3D collagen matrix. Unlike in 2D cultures, stress fibers are not apparent and polymerized actin (as labeled by phallotoxins) is concentrated at the cell membrane. The cell exhibits small membrane protrusions that are actin-rich and presumably stabilized by cell-ECM adhesions (Figure 3.5A arrows). We measure the displacement of probing particles around each cell when perturbed by HOT as described above. To further elucidate the role of the cell contraction forces, we measure the mechanical response of each particle before and after we biochemically disrupt the cell actin cytoskeleton with cytochalasin D, which suppresses the contraction forces and restores the collagen network to a stress-free state. From these measurements, we calculate the local compliance J_{cell} and J_{free} before and after cytochalasin D treatment, as well as A_{cell}, A_{free}, θ_{cell}, θ_{free}. We have repeated the experiment on 7 samples (3 NIH 3T3 and 4 MDA-MB-231) with more than 100 probing particles in total.

We find that the effect of cells on the local compliance is spatially dependent. Figure 3.5B shows the spatial variation of the change of local compliance $\frac{|\Delta J|}{J_{free}}(r)$, where $\Delta J = J_{cell} - J_{free}$ and r is the distance between the probing particle and cell membrane as determined from confocal image stacks. The change of compliance gradually decrease as r increases, and remains significant ($\sim 20\%$) as far as 80 μm away from the cell. When r is small ($r < 10$ μm), the change of local compliance
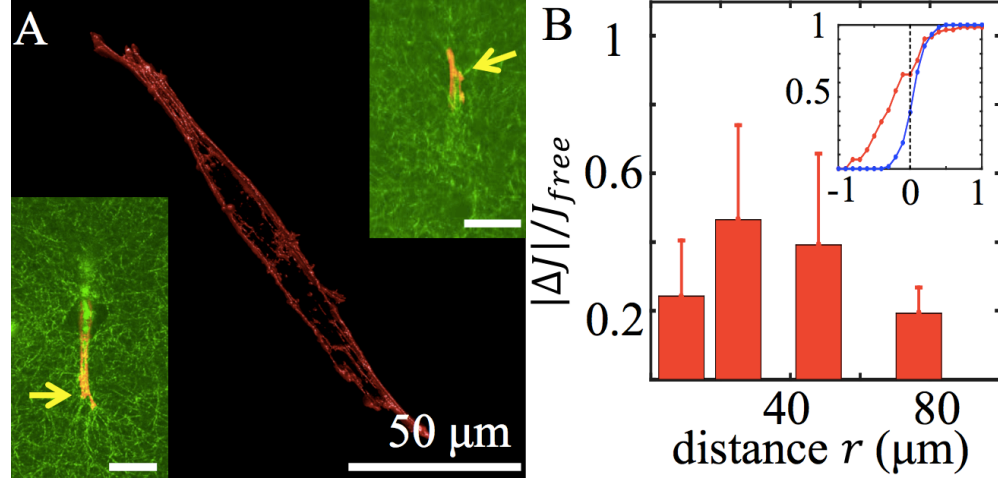
Figure 3.5: ECM micromechanical properties are remodeled by cell contraction forces. (A) 3D reconstruction of a MDA-MB-231 cell embedded in a collagen matrix based on its F-actin immunofluorescence. Insets show the confocal slices with simultaneous imaging of actin (red) and collagen fibers (green) of the same cell. Scale bars: 50 μm. (B) Relative change of local compliance ($\frac{|\Delta J|}{J_{free}}$) as a function of probe-to-cell distance (r). Inset: cumulative probability of $\frac{\Delta J}{J_{free}}$ (red), and ΔA (blue). A vertical line intersects the two curves at $\frac{|\Delta J|}{J_{free}} = 0$ and $\Delta A = 0$. Error bars are standard deviations.

is suppressed by the mechanical property of the cell itself, which is more rigid than the local collagen matrix. This explains the non-monotonic trend shown in Figure 3.5B, and is also confirmed by numerical simulations below. We have also obtained statistics of changes in the local mechanical properties. As shown in the inset of Figure 3.5B, from the cumulative probability of $\frac{\Delta J}{J_{free}}$ (red), and ΔA (blue), we find that the cells tend to stiffen their local ECM (>65% probes), and increase ECM anisotropy (>62% probes).

To further elucidate the role of cell contraction forces in remodeling the local mechanics of the ECM, we have measured the strain field generated by the cells

embedded in collagen gels with 3D particle tracking velocimetry (see Materials and Methods below). A typical result is shown in Figure 3.6A. Two confocal slices at different depths are plotted with (2D projections) contours of strain magnitude and arrows of deformation field. To facilitate imaging, we have fluorescently labeled the cells as shown in the top slice. The strain field is not symmetric, and is strongly correlated with the cell morphology [95]. The magnitude of the strain field represents the change of microstructure, and we expect that larger strain correlates with more significant changes of micromechanical properties. Indeed, as shown in Figure 3.6B, the relative change of compliance $\frac{|\Delta J|}{J_{free}}$ increases monotonically with strain magnitude. At the same time, larger strain also increases the micromechanical anisotropy (Figure 3.6B inset). From these results, it is evident that cells actively remodel the micromechanics of their 3D ECM. These effects propagate as far as $\sim 80 \ \mu$m away from the cell, mediated by the strain fields generated by cellular contraction forces.

3.2.3   Simulated Biopolymer Network Micromechanics

In order to provide fundamental understanding of the micromechanical measurements, we have developed a 2D lattice-based computational model. Our model is constructed on a triangular lattice. As described previously [55, 96, 69], triangular lattice models have successfully reproduced many bulk mechanical features of biopolymer networks, such as strain stiffening, the bending-stretching transition and shear-induced fiber alignment. However, the utility of triangular lattice models
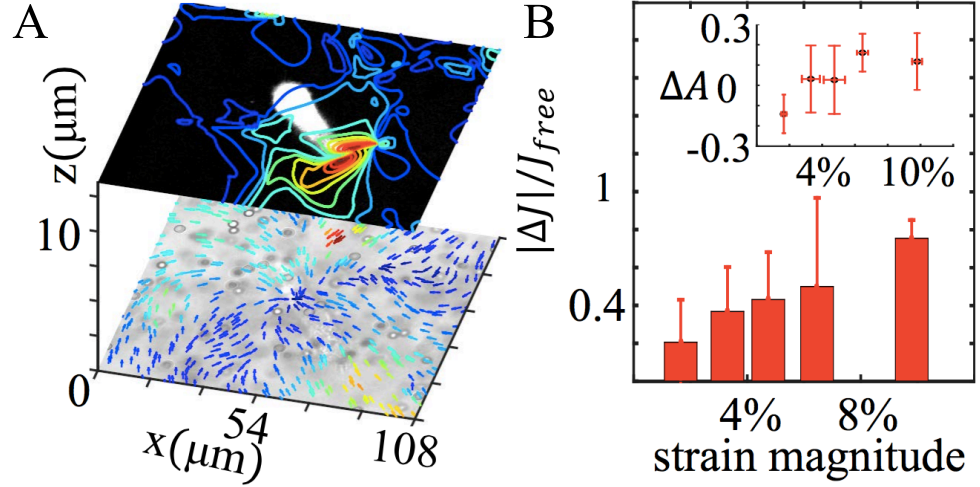
Figure 3.6: Cell remodeling of ECM micromechanical properties is modulated by local strain magnitude. (A) Two confocal slices of a typical sample. The slices are separate by 12.5 μm apart along the optical axis. The top slice shows the fluorescently labeled cell (white on black background) and the strain magnitude contours. The bottom slice shows the bright-field (non-descanned channel) image of the same cell (outlined in black curve) and the deformation field caused by cell contraction forces. The color of the contours and the arrows are scaled linearly (blue to yellow) with the magnitude of strain field (0 to 11%) and the deformation field (0 to 3 μm). (B) Relative change of the local compliance ($\frac{|\Delta J|}{J_{free}}$) as a function of local strain magnitude. Inset: ΔA as a function of local strain magnitude. Error bars are standard deviations.

in understanding ECM micromechanics has not been reported to our knowledge.

The network construction has been described in detail previously [96, 97]. Briefly, on a regular triangular lattice, each bond is of length a and is present with probability p. Straight lines in this lattice, which have average length $(1-p)^{-1}$, are identified as fibers with stretching stiffness k and bending stiffness κ. The lattice

sites are freely rotating crosslinks. The Hamiltonian of the entire network is:

$$E_{elastic} = \frac{k}{2a} \sum_{\langle ij \rangle} g_{ij}(|\mathbf{R}_{ij}| - a)^2 + \frac{\kappa}{2a} \sum_{\langle ijk \rangle} g_{ij}g_{jk}\Delta\theta_{ijk}^2 \qquad (3.7)$$

where $g_{ij} = 1$ for bonds that are present and 0 for removed ones. The first term is the stretching energy; $|\mathbf{R}_{ij}|$ is the distance between sites i and j in the deformed state. The second term is the bending energy; $\langle ijk \rangle$ labels three consecutive sites along a straight line in the reference state, and $\Delta\theta_{ijk}$ is the change of angle along the fiber. We vary the value of the relative bending stiffness $\kappa/(ka^2)$, ranging from 10^{-4} to 10^{-2}. This is consistent with what is expected for actual collagen fibers, because the ratio $\kappa/(ka^2)$ is of the order of $(d/a)^2$, where d and a are the diameter and mesh size obtained when modeling the fibers as simple elastic rods [70]. Previous studies report an average connectivity (number of fiber segments meeting at a junction) of $z \approx 3.4$; therefore, we set $p = 0.55 \approx 3.4/6$ in our model [16, 48]. To simulate collagen networks of qualitatively different microstructures, following the above construction, we apply the Metropolis-Hastings algorithm , which controls network heterogeneity through an effective temperature T_{eff}. Consistent with our previous experimental results [57], at higher effective temperature, the network consists of short and thin fibers. At low effective temperatures, the network contains thick fiber clusters. Generally, the heterogeneity of the network monotonically decreases as T_{eff} increases.

We model a probing particle as a circular hole in the lattice network with its boundary connecting to neighboring bonds (Figure 3.7A), and the optical trap as a
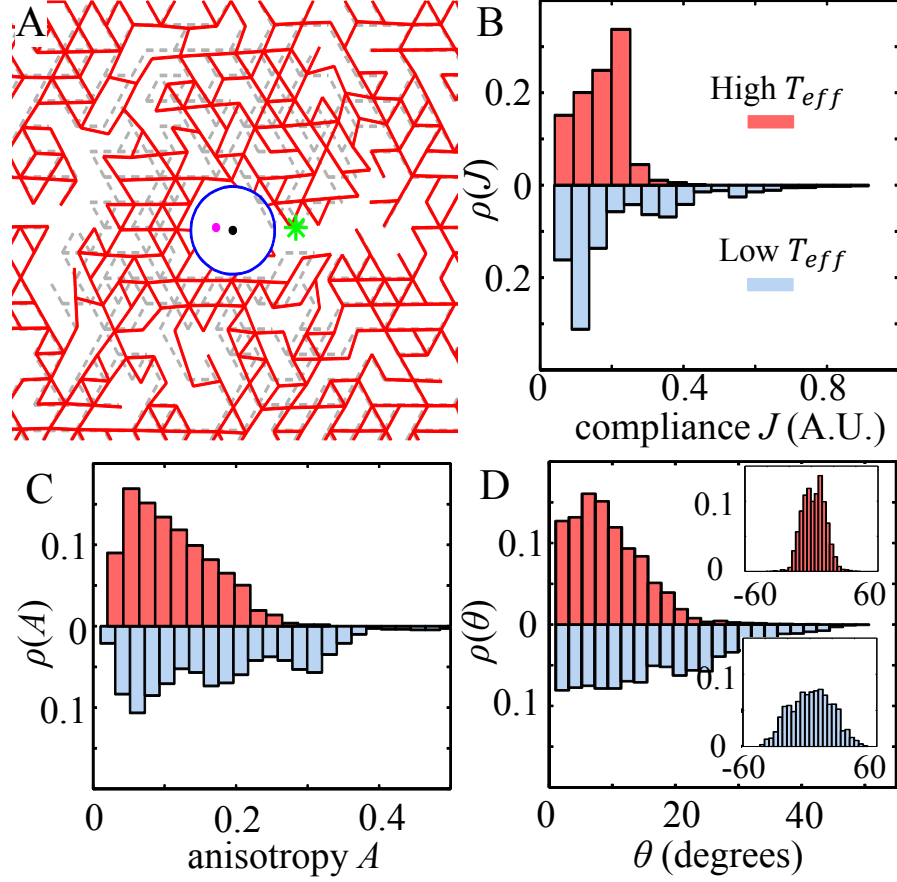
Figure 3.7: Simulation results of the micromechanics of biopolymer networks. (A) The micromechanical response of the network. Whole simulation network is 150 × 150 bound length. A probing particle (centered at the pink dot) embedded in a stress-free network (gray dash lines) moves to a new equilibrium position (black dot and blue circle) and deforms its surrounding matrix (red lines) in response to the force of an optical trap (centered at green star). (B) Normalized histogram of compliance J for lattice network grown at high effective temperature ($T_{eff} = 50$, upper panel) and at low effective temperature ($T_{eff} = 10$, lower panel). (C) Normalized histogram of anisotropy A for a lattice network grown at $T_{eff} = 50$ (upper panel) and $T_{eff} = 10$ (lower panel). (D) Normalized histogram of off-axis angles θ for a lattice network grown at $T_{eff} = 50$ (upper panel) and $T_{eff} = 10$ (lower panel).

quadratic potential well: $E_{trap} = \frac{1}{2}k_p \cdot \Delta L^2$. Thus the total Hamiltonian becomes: $E_{total} = E_{elastic} + E_{trap}$. The equilibrium state of the network is calculated by applying the conjugate gradient (CG) method, which allows us to extract particle displacements analogous to those measured directly in the experiments. As shown in Figure 3.7B-D, the distributions of compliance J, anisotropy A and off-axis angle θ for networks formed at two different effective temperatures demonstrate the same trends as the experimental results, and to some extent agree quantitatively with Figure 3.2B-D. Moreover, we find in our simulations that networks formed at lower T_{eff} have greater spatial variations in their micromechanical properties, which is consistent with the experimental measurements.

To simulate a cellularized collagen network, we model a contracting cell as an ellipse (aspect ratio 5:1 as obtained from typical cell morphology in experiments) embedded in the network and shorten the bond lengths isotropically of any bonds inside the ellipse [33, 98] (Figure 3.8A). Similar to our experimental measurements, we have compared the micromechanical compliance with (J_{cell}) and without cell contraction (J_{free}). As shown in Figure 3.8B, the relative change of compliance $\frac{|\Delta J|}{J_{free}}$ measured at varying distances from the cell agrees well with the experimental results. This non-monotonic behavior can be explained by the intrinsic rigidity of the cell, which exists even in the absence of contractive forces. Employing our computational model, we have further examined the directional dependence of $\frac{|\Delta J|}{J_{free}}$. As shown in Figure 3.8C-D, similar trends are observed along both the long and short axes. However, the magnitudes differ by as much as 50%. This difference explains the relatively large error bar in Figure 3.8B.
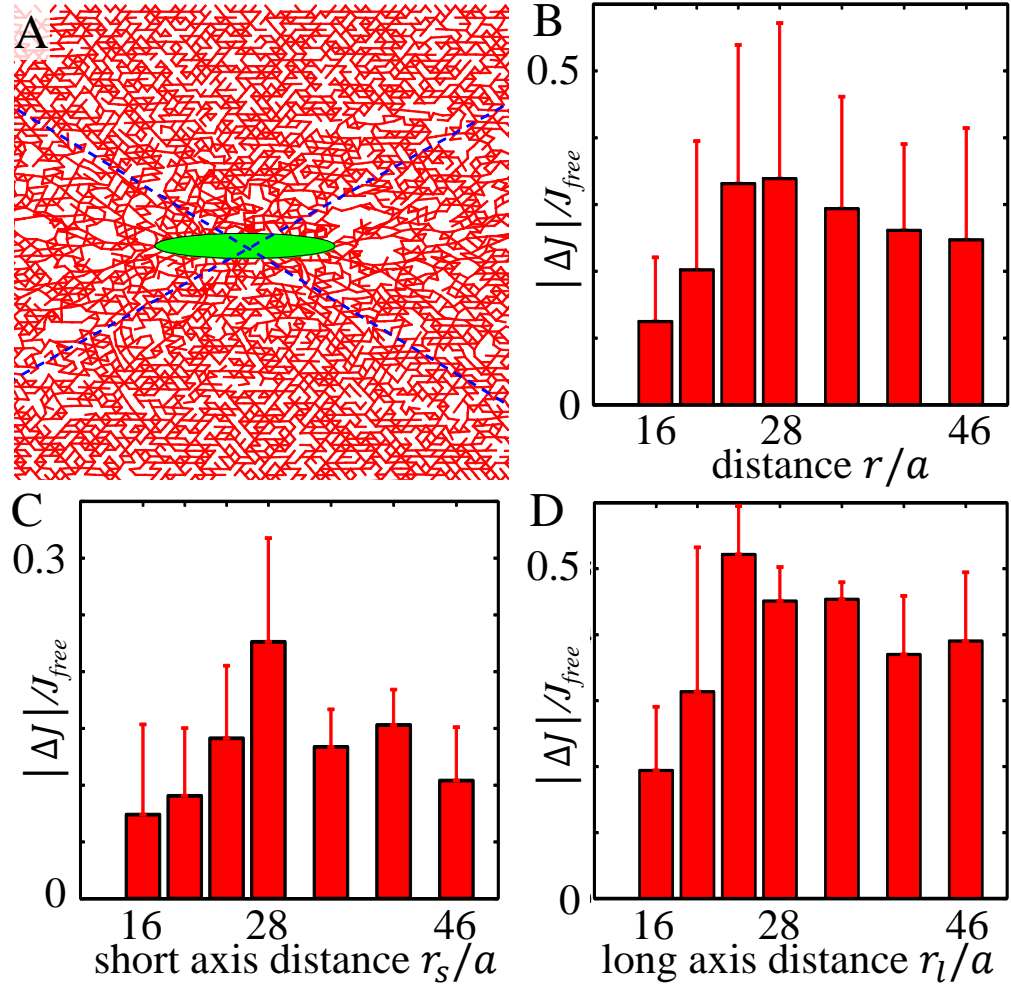
Figure 3.8: Simulation results of the cellularized collagen network micromechanics. (A) The equilibrium configuration of a cellularized network. The green ellipse in the center stands for a contractive cell. The blue dashed lines divide the whole space into four parts. Top and bottom parts are in the short axis direction, left and right parts are in the long axis direction. (B) Relative change of compliance J, $\frac{|\Delta J|}{J_{free}}$ as a function of distance r (in units of bond length a) from the cell. (C) $\frac{|\Delta J|}{J_{free}}$ as a function of distance in the short axis direction (r_s/a). (D) $\frac{|\Delta J|}{J_{free}}$ as a function of distance in the long axis direction (r_l/a).

The above results demonstrate that triangular lattice models and their extensions capture the main features of the micromechanics of cellularized collagen gel. The rich micromechanical properties are intrinsically tied to the microstructure of the fiber network, as well as the stress states determined by the dynamic cell-ECM interactions.

3.3   Discussion

We have reported on the experimental and computational studies to elucidate the micromechanics of cellularized collagen networks. We have demonstrated that when probing scales smaller than the structure discreteness, rich mechanical properties are observed beyond the predictions of micro or bulk rheology. Although these properties are microscopic measurables, they are determined by the network configuration on a larger scale ($\sim$20 times the mesh size determined from simulation). Therefore, the ECM microstructure has a significant effect on ECM micromechanical characteristics, as we have confirmed both experimentally and by simulation. In particular, the sharply distributed micromechanical compliance J for collagen gels grown at 37 °C agrees with the value measured from bulk rheology (such as in [48]). In these cases, gel pore sizes are typically smaller than the probing particles, and we expect the continuous medium assumption together with equation (3.1) to be a good approximation. However, for collagen gels which have large spatial heterogeneities and pore sizes, the bulk rheology becomes a poor predictor of micromechanics. Indeed, while gels grown at 21 °C typically have a

smaller bulk compliance compared with 37 °C gels [20, 48], the average of microme-chanical compliance shows the opposite. The breakdown of continuum assumption is evident from the broad distribution of J shown in Figure 3.2. In this case, we expect that bulk rheology and micromechanics probe different physical properties of the collagen network.

We have shown that a relatively simple model of collagen gels can capture many features of the experimental data. The model is based on a two-dimensional lattice and is not meant to be a precise match to the three-dimensional sample. Instead, it serves as a way to make sense of the general properties of fiber-based bending-dominated elastic systems. These systems have well-understood macro-scopic properties such as strain stiffening and nonlinear differential Poisson ratios that emerge from this model class, and we show here for the first time that the micromechanical properties can also be successfully modeled, both with and with-out embedded cells. Of particular interest is the difference between high and low temperature gels, seen both in the data and in our simulations; there is a pro-nounced increase in local mechanical variability for the gels that are created at low temperature, connected to their increased structural variability. We should note that the model underpredicts the extent of this variability for the compliance data. This may be due to the fact that in our model the bonds have a fixed elastic response independent of temperature, which results in a temperature-independent average compliance, as opposed to the net change in mean compliance seen in the data. Our focus here is on the variance for which the model does reflect the correct physics resulting from the differing network heterogeneity.

We have applied a 2D model rather than 3D in this study for computational complexity consideration. It is worth noting that continuum elasticity in 2D allows mechanical perturbation to propagate longer range than its counterpart in 3D. This possibly suggests an overestimation of the range of the effects shown in Figure 3.8. However, previous studies on the break-down of continuum elasticity in fiber matrices have shown anomalous, long-range deviations from continuum elasticity in 2D matrices [99, 100]. Therefore it is natural to expect the fiber nature could also result in long-range non-continuum effects in 3D. In this sense, our 2D model is enlightening to understand micromechanics of real 3D biopolymer networks.

When collagen gels are populated by contractive cells, the micromechanical properties are significantly altered locally. For NIH 3T3 and MDA-MB-231 cells, the effects can be seen as far as 100 μm away for gels at collagen density of 2 mg/ml. This is consistent with the observation that bulk rheology of collagen gels is modified at high embedding cell densities [44]. The micromechanical remodeling is highly correlated with the strain field created by the cellular contraction forces, thus further illustrating the close structure-property relation at microscopic scales. Reciprocally, micromechanics, more directly than the bulk rheology of ECM, regulates the morphology, migration, proliferation and differentiation of embedded cells [101, 102]. Therefore we expect that micromechanical heterogeneity is a key factor that contributes to the heterogeneous cellular behaviors observed even in the same 3D culture environment [103, 104]. Our experimental and computational approaches provide a novel way of further investigating these effects.

3.4 Materials and Methods

3.4.1 Preparing and imaging collagen gel

Collagen gels are prepared from high-concentration rat tail collagen I in acetic acid (Corning, 10-11 mg/ml). The collagen is diluted with dH_2O (for 21 °C gel) or DMEM growth medium (for 37 °C gel), $10\times$PBS, and 0.1 N NaOH to a final concentration of 1.5 mg/ml and a pH of 7.4. Confocal reflection microscopy images of the collagen gels are taken using an inverted laser scanning confocal microscope (LSCM, Leica TCS SPE) with either a $20\times$ or $40\times$ oil immersion objective.

3.4.2 3D cell culture and staining

NIH 3T3 mouse fibroblast and MBA-MB-231 human breast cancer cells are suspended at very low density in neutralized collagen solutions. The suspension is then immediately transfered to gridded glass bottom dishes (ibidi μ-dish Grid-50) and incubated in a tissue culture incubator (37 °C, 5% CO2) for at least 24 hours before staining or micromechanical measurements. Actin staining is done using Alexa Fluor 488 phalloidin dye (Life Technologies) on fixed samples. For cellularized collagen gel, micromechanical measurements with active cell traction forces are followed by staining the cell using CellTracker Green dye (Life Technologies). We then perform confocal imaging before and after cytochalasin D (Sigma Aldrich, 10 μg/ml in PBS) treatment for 1-2 hours. Micromechanical measurements are then conducted again with the same probing particles.

3.4.3   Holographic optical tweezers calibration

A holographic optical tweezers system with a 1064-nm trapping laser and a 100X, 1.6 NA, oil-immersion objective is used for micromechanical measurements [88]. Video microscopy measurements are taken with the sample illuminated by a red LED and recorded at 60 fps, while the displaced trap is pulsed at 0.7 Hz by a mechanical shutter. To determine the location of the particle, the video microscopy images are analyzed with a tracking algorithm based on the radial symmetry of the particle's image [90]. The particle trajectories are then fitted using a built in pulse fitting function in MATLAB (MathWorks, Inc.) to obtain the mean displacements.

The micromechanical measurements described in the main text require precise control over the magnitude and direction of the applied trapping force. For small trap displacements, the force is approximated as linearly proportional to the displacement of the trap relative to the particle. We calculate the force in the direction of the trap as $F = k_t(d_t - \Delta d^{\parallel})$, where k_t is the stiffness of the trap, d_t is the displacement of the trap from the equilibrium position of the particle, and $\Delta d^{\parallel}$ is the displacement of the particle in the direction of the trap displacement. We carry out three calibration experiments, one to determine the stiffness of the trap, another to determine the appropriate trap displacement, and the final to test the precision of the direction of applied forces.

The stiffness of the trap is determined using the Equipartition method [105]. We trap a 3 μm particle in water and observe the Brownian motion due to thermal fluctuations. A video of the trapped particle is recorded at 60 frames per second for
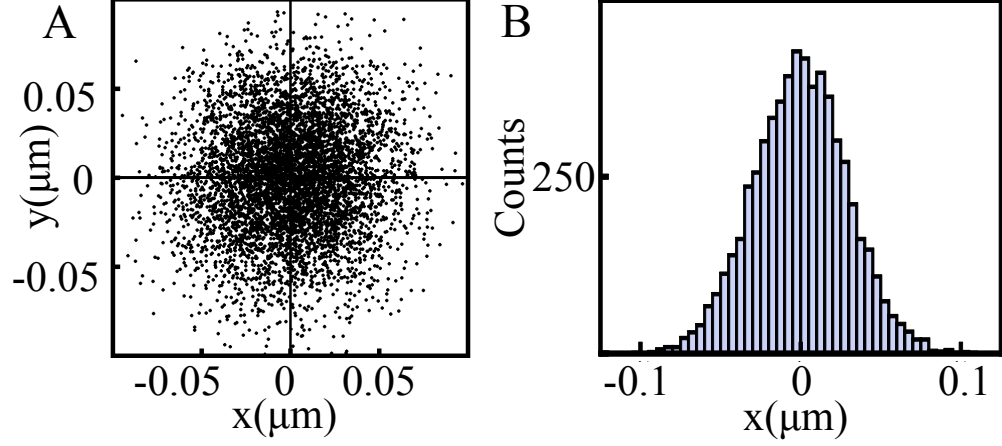
Figure 3.9: Calibration of holographic optical trap stiffness. (A) XY trajectory of the Brownian motion of a 3 μm diameter sphere trapped in water at 35% laser power. (B) Histogram of the x position of the particle showing a Gaussian distribution with a standard deviation of $\sigma_x = 0.0313\mu m$.

approximately 1 minute 30 seconds (roughly 5000 total frames). Figure 3.9A shows the Brownian motion of a typical particle. According the Equipartition theorem, the thermal energy is equal to the average potential energy of the particle with $\frac{1}{2}k_bT$ for each degree of freedom in the motion. Treating the optical trap as a harmonic potential well, we get $\frac{1}{2}k_bT = \frac{1}{2}k_t\langle x^2\rangle$, where k_b is the Boltzmann constant, T is the absolute temperature of the water, and $\langle x^2\rangle$ is the variance, or square of the standard deviation σ_x, of the spatial fluctuations ($\langle x\rangle = 0$). We seperate the Brownian motion into the x and y components and fit each with a Gaussian distribution to find the standard deviation. Figure 3.9B shows a histogram of fluctuations in the x direction for a typical particle. The standard deviations for both directions are $\sigma_x = 31.3\ nm$ and $\sigma_y = 33.1\ nm$. Using an absolute temperature of 294 K, this gives stiffnesses of $k_x = 4.159\ pN/\mu m$ and $k_y = 3.72\ pN/\mu m$. Finally,

although micromechanical measurements were carried out at 60% laser power, this calibration was done at 35% power to increase the observed Brownian motion. This increase in power increases the intensity of the beam by a factor of 5.348, so rescaling the stiffnesses we get $k_x = 22.24 \ pN/\mu m$ and $k_y = 19.98 \ pN/\mu m$.

While the calibration was done in water, the micromechanical measurements were done in collagen gels. For the gels used in our experiments, collagen only makes less than 2% of the total mass while the rest is mainly water. Therefore we expect the trap stiffness in water and in collagen gels are very close. Indeed, from the recent turbidity data of collagen gel ($\sim 1 \ cm^{-1}$[18]), we estimate that the scattering of light at 50 μm depth will cause less than 1% reduction in the trap stiffness in collagen gel.

To determine the appropriate trap displacement, we perform a calibration on particles embedded in a homogeneous collagen gel. We center the trap on the particle, then increase the trap displacement in the $+x$ direction in increments of 0.096 μm. The particle displacement as a function of trap displacement is plotted in Figure 3.10A. The particle response increases roughly linearly until it reaches a maximum at a trap displacement of 1.35 μm. For our linear model of the trapping force to be valid, we chose a trap displacement of 0.725 μm for all micromechanical measurements, safely within the approximately linear region and represented by the vertical dashed line in Figure 3.10A. Also, note that y displacements were minimal as a highly isotropic particle was chosen for this calibration.

Next we focus on the linear region of trap displacements to explore the linearity of collagen response. Figure 3.10B shows particle displacement in the x direction

85
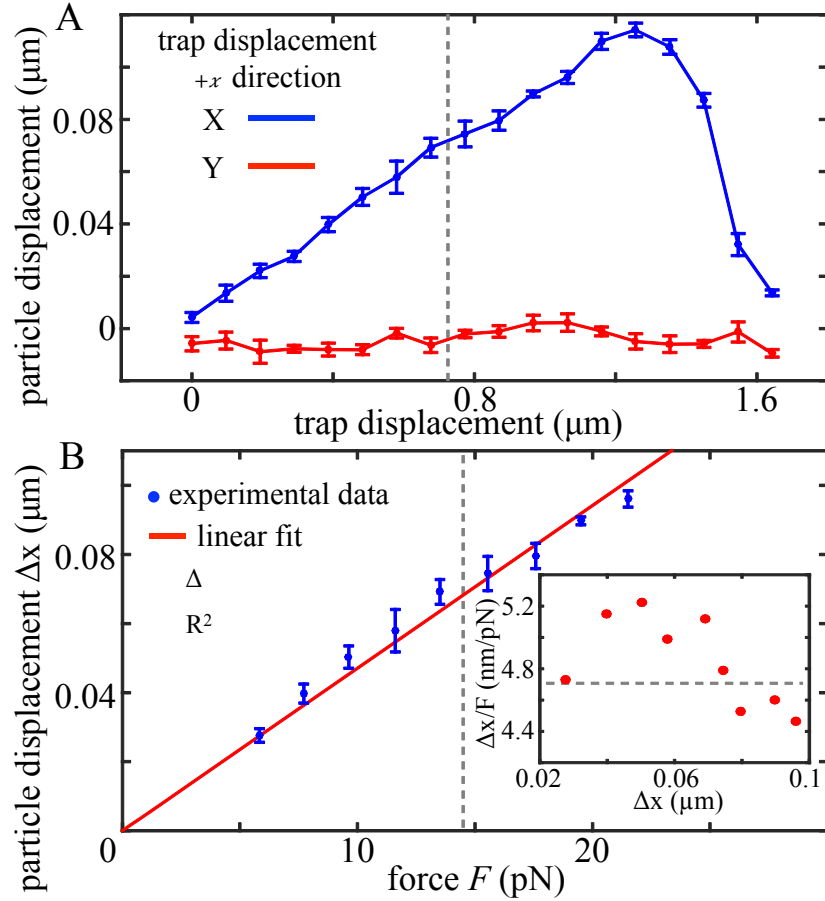
Figure 3.10: Calibration of holographic optical trap stiffness. (A) Plot of particle dispacement vs. trap displacement for a 3 μm particle embedded in a homogeneous 1.5 mg/ml collagen gel. Trap is displaced in the $+x$ direction and the particle response is seperated into x and y displacement. The vertical dashed line represents a trap displacement of 0.725 μm which is the trap displacement used for all micromechanical measurements. (B) Plot of particle displacement vs. force with a linear fit passing through the origin. The vertical dashed line is at 14.5 pN, corresponding to a trap displacement of 0.725 μm. Inset: Plot of $\Delta x/F$ (inverse spring constant) vs. particle displacement. The horizontal line represents 4.71 $nm/\mu m$, the slope of the linear fit to the experimental data. Error bars in C and D represent standard deviation of particle displacements.

Δx vs force F for trap displacements in the range 0.288 μm to 1.056 μm. F represents both the trapping force and the elastic force from the collagen which are equal in magnitude once the particle reaches its displaced position. We see that the particle displacement is quite linear with respect to force in this region and a linear fit to the experimental data is performed in MATLAB. The fit is restricted to pass through the origin and has a slope of 4.71 nm/pN ($R^2 = 0.9712$) which is the apparent inverse spring constant $\Delta x/F$ of the collagen around this particle. The dashed vertical line shows a force of 14.5 pN corresponding to a trap displacement of 0.725 μm. The inset of Figure 3.10B shows $\Delta x/F$ for each different particle displacement with the horizontal line representing 4.71 nm/pN, the value obtained from the linear fit. The average difference between the individual $\Delta x/F$ and the fitted value is less than 5%. The results suggest that for the range of particle displacements we used in our experiments, the micromechanics is not dependent on the probing force.

Finally, we calibrate the directional precision with which we can apply forces to particles embedded in collagen. Our holographic optical tweezers use a computer-controlled spatial light modulator to control the location of optical traps. The holograms are calculated in LabView using software based on 'Blue Tweezers' from the University of Glasgow [106] and allow precise control of trap position in real time. We carry out the calibration in water by calculating trap positions displaced by 0.725 μm from the center location at various angles. The trap position relative to the center is calculated using polar coordinates with $\rho = 0.725$ μm and φ defined as the angle counter clockwise from the $+x$ direction. We increase φ
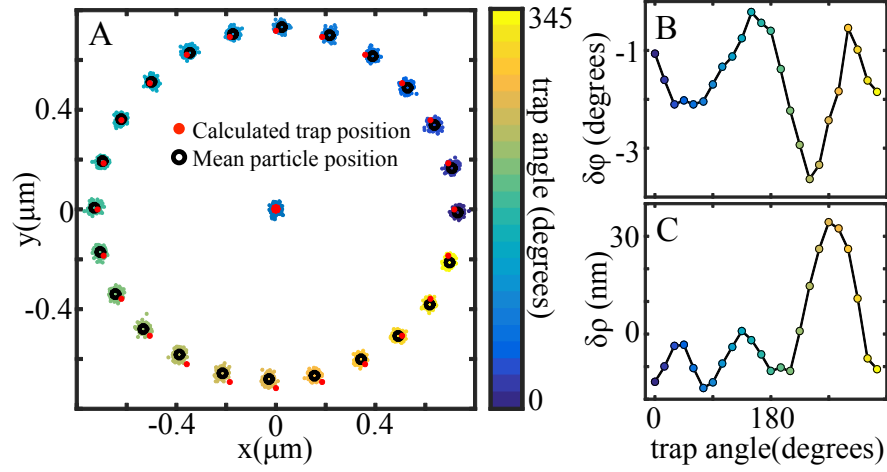
Figure 3.11: Calibration of angular and radial precision of trap displacement with holographic optical tweezers. (A) XY trajectories of a particle trapped in water, with the center spot representing the undisplaced trap position and outer spots representing the trap displaced holographically at different angles around the center spot. The trap displacement angle φ is defined as the angle couterclockwise from the $+x$ direction. The trap angle is increased by 15° steps and the radial trap displacement ρ is 0.7250 μm. (B) Difference between trap angle and expected angle. (C) Difference between trap displacement and expected displacement.

in 15° increments and compare the actual mean position of the particle with the calculated trap location. Figure 3.11A compares the calculated and actual trap positions for all angles. Figure 3.11B shows the difference $\delta\varphi$ between the actual trap angle and the expected angle. Overall, there is an average angular shift of -1.6° with a maximum difference of -3.6°. In addition, we compare the measured displacement ρ with the expected value of 0.725 μm and find a maximum difference of 35 nm. The difference $\delta\rho$ is plotted in Figure 3.11C. Overall, we expect these small errors in the spatial precision of the trap location have a negligable effect on micromechanical measurement.

3.4.4   Three-Dimensional Particle Tracking

In order to measure the 3D strain field caused by the cell contraction forces, we obtain confocal image stacks before and after cells are treated by cytochalasin D and utilize the non-descanned (NDS) channel (Figure 3.12A). To determine the 3D particle centers, we first determine the 2-D particle centers in all image slices, together with the integrated intensity associated with each 2-D particle center (Figure 3.12B, [107]). The result of this step can be labeled as $S_i = [x_i, y_i, z_i, I_i]$, where z_i is an integer number (slice number) times the scanning step (0.5 μm). x_i, y_i, I_i are the coordinates and integrated intensity of 2D particle centers [108] which are detected in the slice corresponding to z_i, and i is the index of all 2D particle centers in all z-slices. Fig. S3.12B shows a typical image slice with its corresponding 2D centers labeled with blue circles. Since the same particle will appear in several consecutive slices, we then search in the collection $\{S_i\}$ that belong to the same particle. To do this, we notice that 2D projection of particle-to-particle distance is more than 10 pixels (1.7 μm) in all our samples, while the errors in 2-D particle locations is less than 0.5 pixels [108]. Therefore we consider S_i and S_j belong to the same group if

$$\sqrt{(x_i - x_j)^2 + (y_i - y_j)^2} < 0.34 \ \mu\text{m}, |z_i - z_j| < 0.4 \ \mu\text{m} \qquad (3.8)$$

We have checked the effectiveness of these criteria by visually inspecting the image slices. We have confirmed that each group of $\{S_i\}$ corresponds to exactly one particle in the gel. Now to determine the actual 3D center $[X_\alpha, Y_\alpha, Z_\alpha]$ of particle
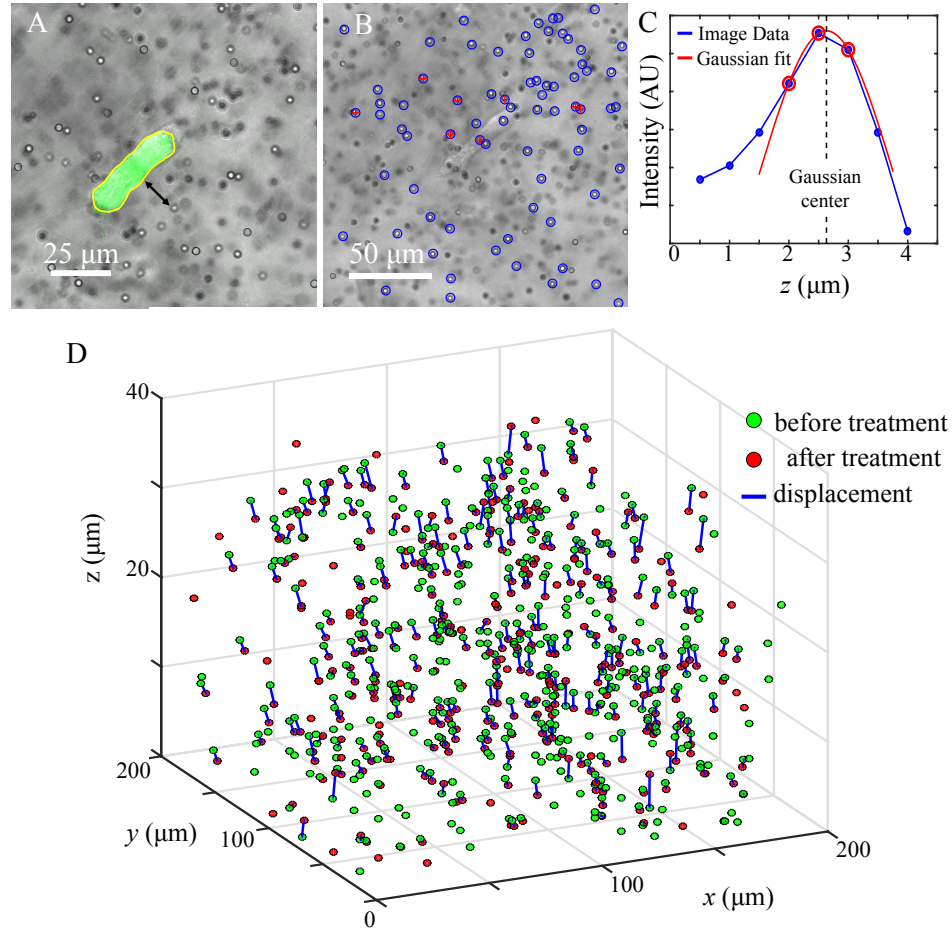
Figure 3.12: 3D particle tracking to measure the strain field. (A) Overlay of non-descanned (NDS) and fluorescent channels of a confocal slice. The arrowed line represents the distance between a probe particle to the cell. (B-C) Example of 3D particle localization from the confocal image stack. (B) X-Y positions are first determined at subpixel resolution (blue circles). (C) The z position of a particle is determined by fitting the particle intensity profile $I(z)$ (blue curve) with a Gaussian function (red). Only three points around the maximum of $I(z)$ are included in the fitting, and z position of the particle is defined as the center of the Gaussian function. Red crosses in (B) indicate particles whose rounded z-position is in the shown confocal slice. (D) Deformation field obtained by associating 3D particle centers before and after cytochalasin D treatment.

α, consider its corresponding group $\{S_i\}$, $i \in \alpha$. We use the weighted average to calculate $X_\alpha = \frac{\sum_{i \in \alpha} x_i I_i}{\sum_{i \in \alpha} I_i}$, $Y_\alpha = \frac{\sum_{i \in \alpha} y_i I_i}{\sum_{i \in \alpha} I_i}$. To determine Z_α, note that the intensity profile along z direction $I(z) = I_i(z_i)$, $i \in \alpha$ has a characteristic bell shape (Figure 3.12C). We fit the three points around the maximum of the intensity profile $I(z)$ with a Gaussian function and determine Z_α to be the center of the Gaussian fitting (Figure 3.12D). Such three-point Gaussian fitting has been widely used in particle image velocimetry to obtain sub-pixel (less than 0.5 μm in our case) resolutions [109].

Using the above method, we determine the 3D particle centers before and after cytochalasin D treatment. We then apply the Crocker-Grier algorithm [108], which associates the 3D particle centers before and after cytochalasin D treatment (Figure 3.12D), therefore obtaining the deformation field $\mathbf{D}(\mathbf{r})$ sampled at all the 3D particle centers. To further calculate the strain field ϵ_{ij}, we will need to calculate the numerical derivatives $\epsilon_{ij} = \frac{1}{2}(\frac{\partial \mathbf{D}i}{\partial r_j} + \frac{\partial \mathbf{D}j}{\partial r_i})$, where i, j label 3D spatial dimensions. To this end, we first interpolated the deformation field onto a fine regular grid lattice (grid spacing 0.17 μm) using natural neighbor interpolation [110], which provides a C^1 smooth approximation of $\mathbf{D}(\mathbf{r})$. We then take direct numeric derivatives on the regular grid to obtain the approximated ϵ_{ij}.

4 Stress-Induced Plasticity of Dynamic Biopolymer Networks

In this chapter we show that 3D collagen gels are significantly and irreversibly remodeled by cellular traction forces, as well as by macroscopic strains. To understand this ECM plasticity, we present a computational model that takes into account the sliding and merging of ECM fibers.

This work is currently in preparation for publication in *Nature Communications*. Christopher Jones performed and analyzed all bulk rheology experiments and contributed to micromechanical data collection and performed micromechanical data analysis. Jihan Kim prepared all collagen bundle samples, carried out confocal imaging, developed microstretcher and contributed to micromechanical data collection. Jingchen Feng and Prof. Herbert Levine at Rice University developed the computational model in collaboration with Prof. Xiaming Mao and Prof. Leonard Sander at the University of Michigan.

4.1 Introduction

Interactions between cells and the extracellular matrix (ECM) are crucial to maintain the integrity of our living tissues [111]. The main structural component of ECM in connective tissue is a matrix of collagen fibers [58], and this matrix is constantly remodeled by the cells living within it [112, 113]. Tissue homeostasis is

a continuous process in which new collagen fibers are synthesized [23] and existing fibers are degraded [24]. This can be due to a regular process of tissue homeostasis, or as a response to inflammation and wounding,

Cells also interact with the collagen matrix physically and probe the nonlinear elasticity [50, 114] and viscoelasticity [115, 116] of the ECM. These physical interactions are generally considered to cause small deformations, and therefore to be completely reversible. For example, a fundamental assumption of the widely employed 3D traction force microscopy is that once cell-generated forces are released, the matrix will bounce back to its non-stressed configuration [117, 118]. In this paper we will show that the assumptions of small and reversible deformations are not always valid when studying cells in collagen ECM.

As an example, recent experiments have reported densified, aligned collagen fibers between clusters of cancer cells [34, 119]. These observations suggest that collective contraction between cell clusters may cause large deformations in the ECM. While these experiment dealt with clusters composed of multiple cells, we find mechanical interactions between a single pair of breast cancer cells alone can significantly increase the local fiber density and alignment of reconstituted collagen matrices. Other workers [120] have also demonstrated the irreversible alignment of fibers near contracting cells. We will show that these large deformations are irreversible, history dependent, and significantly change the ECM micromechanics. The observed ECM remodeling is purely mechanical, without the creation or degradation of ECM fibers by cells.

We present a computational model, based on the dynamics of cross-links and

fiber entanglement. We allow cross-links to *slide* if there is sufficient force on the node. This allows irreversible remodeling. Our approach is similar to that of Nam et. al [49]. However, in that work, a mean-field approach was used for the network remodeling. Instead we take a different approach of fully capturing the complex disordered network structure, because biopolymer networks are strongly disordered networks and the disorder is important in many phenomena. We dynamically update the network locally and characterize the geometry of a pair of interacting cells in the disordered fiber network. Our model gives agreement with cellular experiments, elucidates microscopic details of force and energy distributions in disordered plastic networks.

We also used a parallel plate rheometer to apply macroscopic shear strain and find rich bulk rheology beyond the widely accepted viscoelasticity of a collagen matrix [121, 64, 122]. Specifically, we find that the bulk relaxation kinetics of collagen depend on both the magnitude and duration of the applied shear strain.

Agreement between the model predictions and experiments suggests a novel mechanism that contributes to a dynamic, reconfigurable ECM without the need for chemical modifications.

4.2   Results

4.2.1   Cell Traction Forces Irreversibly Remodel ECM

Traction forces exerted by live cells lead to irreversible remodeling of the surrounding ECM. Figure 4.1A shows an example where two breast cancer cells (MDA-MB-231) are embedded in a type-I collagen gel. Immediately after the gelation process completes, the cells start to generate traction forces which deform the local ECM. Using confocal reflectance imaging, we find that the matrix microstructure is most significantly remodeled between the cells, a region we will refer to as a collagen bundle. A collagen bundle consists of aligned, and densified collagen fibers (Figure 4.1A) connecting the cell pair. Collagen bundles can also form between larger groups of cells as shown in Figure 4.1B. In fact, bundles are generally present between all cell pairs which are within $\sim$80 μm distance.

A common assumption in cell mechanics is that once a traction force is released, the matrix will relax to its original stress-free state. Indeed, when the cell traction forces are released by Cytochalasin-D treatment, the density (quantified by relative intensity in confocal images) of the collagen bundles decreases. However, removing the mechanical stress does not fully remove the collagen bundles. Instead, a significant amount of residual strain remains in the regions of collagen bundles.

To further investigate the mechanical origin of collagen bundles, we have developed a microstretching device, which generates local mechanical deformation in 3D collagen matrix similar to a cell pair (Figure 4.2A). When extensional stress
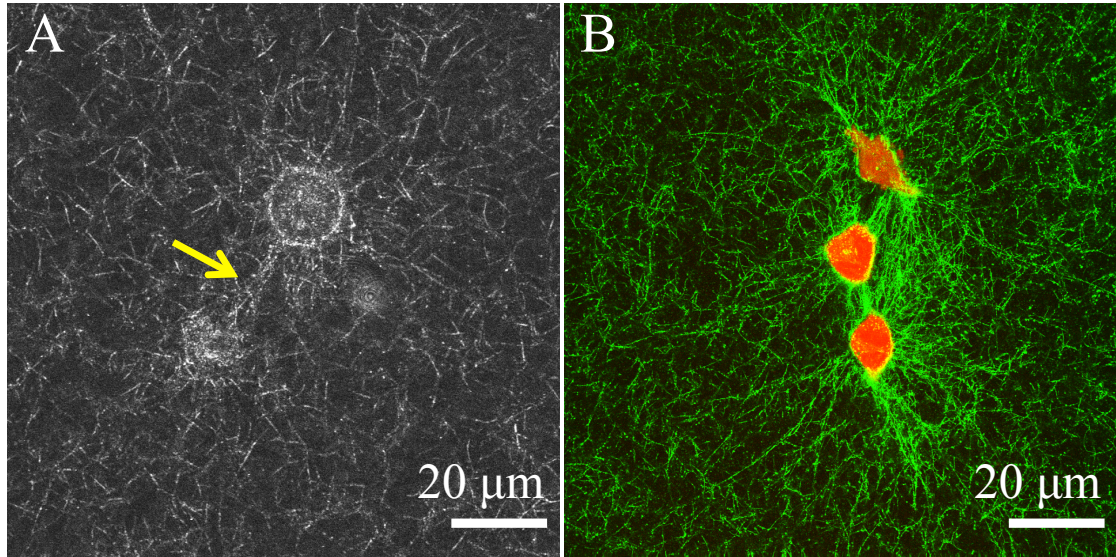
Figure 4.1: Cell traction forces irreversibly induce the formation of collagen bundles. (A) Confocal reflection image of the collagen matrix showing a collagen bundle (arrow) between two MDA-MB-231 cells. (B) Collagen bundles simultaneously form between multiple cell pairs. Red: GFP-labeled MDA-MB-231 cells. Green: reflectance image of collagen fibers.

is applied for a short period of time, the matrix will almost fully recover to its original configuration (Figure 4.2B). When the dwell time of the applied stress is increased, regions of densified fibers persist even after the stress is released (Figure 4.2C). These observations suggest that formation of collagen bundles and the history-dependent plastic ECM remodeling have a purely mechanical origin.

4.2.2 Computational Model of Cell-Induced ECM Remodeling

We hypothesize that the observed plasticity of the collagen matrix is a result of the irreversible dynamics of cross-links and fiber entanglement. To test the hypothesis,
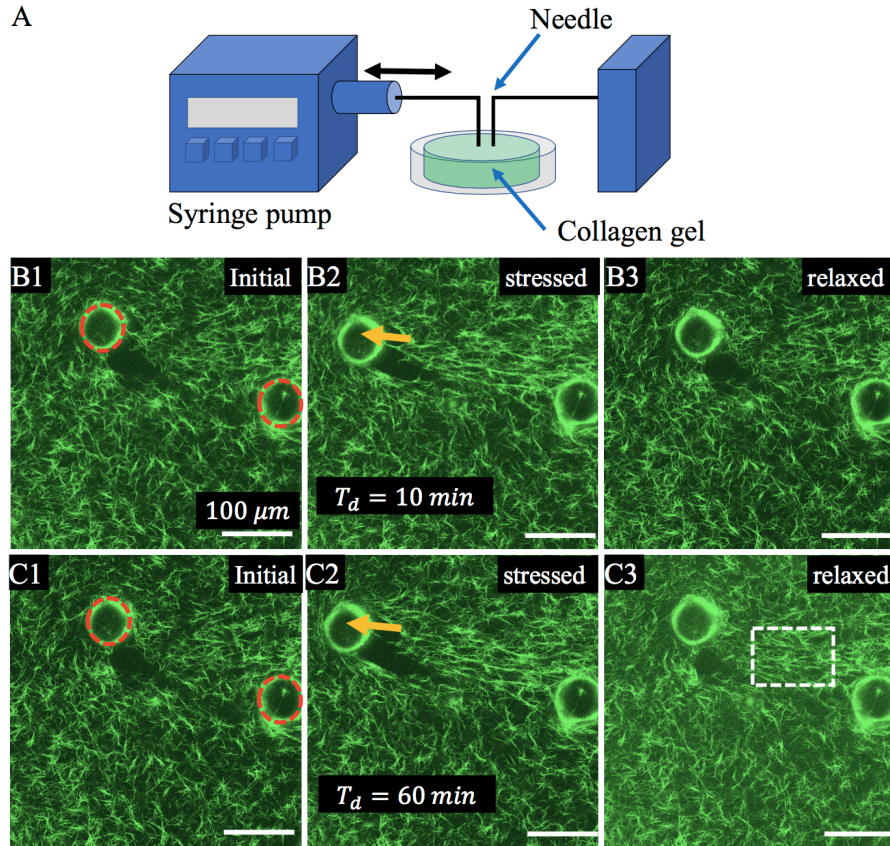
Figure 4.2: (A) Micro-stetcher uses a programmable syringe pump (New Era). Two needle tips are submerged simultaneously in a collagen gel while the gel is formed. One metal needle is connected to the syringe pump which can be controlled by submicron range and the other needle tip is fixed. CellTak (Corning) is used to treat all contact surfaces. (B1,C1) show the unstressed configurations, where initial positions of two needle tips are indicated with red dashed circles. (B2,C2) The configurations of the matrix deformed by moving one of the needles along the direction shown by the yellow arrows. After dwell time T_d of 10 and 60 minutes, the needles are moved back to their original positions. (B3) Short dwell time (10 min) allows the matrix to almost fully return to the initial configuration. (C3) Longer dwell time (60 min) leads to irreversible reorganization of collagen fibers as highlighted in the white rectangle.

we have developed a computational model based on a diluted triangular lattice. We treat the collagen matrix as an athermal network of fibers that resist bending and stretching [69, 123, 124]. Using experimentally derived stretching and bending moduli of fibers [48], and the coordination number of the network [16], we construct a minimal representation of the matrix. The linear and nonlinear elasticity of this model has been extensively studied. It is known that in the linear regime, the elastic energy is dominated by bending energy of the fibers, because the network has lower connectivity than at the central-force isostatic point [123, 124]. As the model is deformed beyond the linear elasticity regime, the elastic energy becomes stretching dominated, and the shear modulus increases by more than an order of magnitude (strain-stiffening), in good agreement with observations of various biopolymer gels [48, 56, 70, 124].

In contrast to previous models that assume static network connections, we consider the cross-links between fibers to be dynamic: when the force loaded on a cross-link exceeds a threshold, two fibers will have a probability to detach and reconnect to lower the elastic energy, or a branching fiber has a probability to peel apart further at the branching point, which we call "sliding". In addition, we consider the merging of adjacent fibers within a critical distance, which can be either due to fiber entanglement or chemical bond formation. Both "sliding" events and "merging" events are intrinsically irreversible and contribute to the plasticity of the model network.

We first test if the model reproduces the observed properties of our collagen bundles. Because experiments observe mostly rounded cells, we model contractive

cells as circles embedded in the network and isotropically shorten all fibers inside the circle by the fraction β. The contracted cell size a in proportion to the matrix pore size has been chosen to be consistent with experimental measured cell radius ($17.2\pm2.6\mu$m) and pore size (3.0 ± 0.7 μm).

At $T = 0$ (immediately after cell contraction), the network configuration is determined by minimizing the elastic energy and no sliding or merging events are allowed to occur (Figure 4.3A). Every half-minute thereafter we allow all possible sliding events to occur deterministically and all merging events to occur with probability $P_{merging}$. This approach is based on the assumption that the time scale of sliding events is much faster than that of merging events. After roughly 15 minutes of maturation time, sliding causes the fibers to continuously flow into the central region between the cells, as we observe in the formation of collagen bundles (Figure 4.3B). Sliding events significantly increase the fiber density in the bundle as compared with purely elastic deformations.

Our model also allows us to examine the irreversibility of the collagen bundles. To this end, we have varied the contractility (β) and maturation time T_m, and measured the density increase in the bundle region. We find that the irreversibility of ECM builds up as a function of maturation time T_m. Intriguingly, the sliding events and merging events play separate roles. The former mainly contributes to the enhanced fiber concentration before releasing cell traction forces, and the later mainly contributes to the irreversibility of collagen bundle formation.
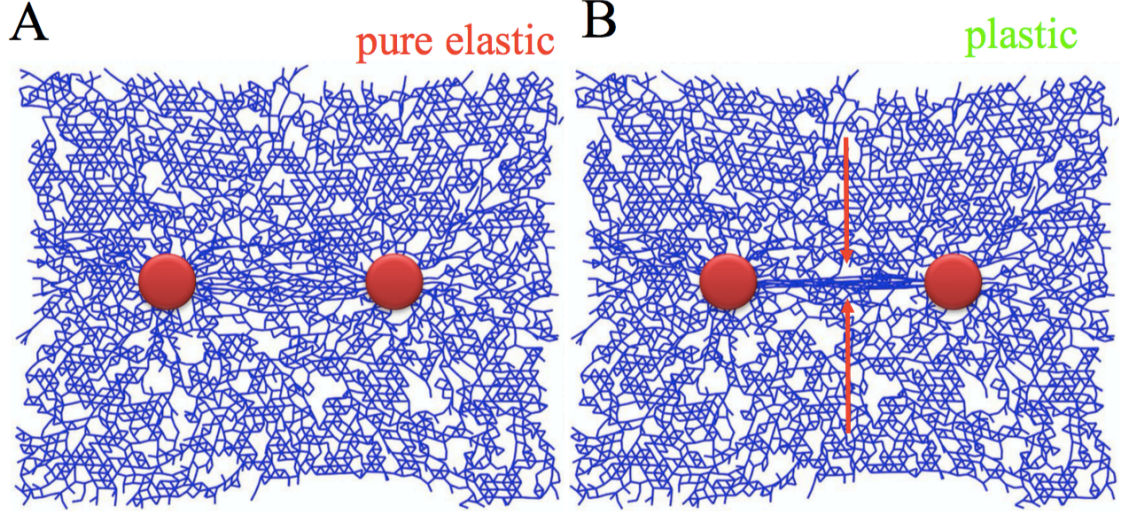
Figure 4.3: Simulation of collagen bundle formation by contracting cell pairs. (A) The network configuration in an elastic model (without any sliding or merging events.) (B) The network configuration predicted by our plastic model.

4.2.3 Macroscopic Remodeling and Relaxation of Collagen

Although the collagen bundles are localized structural features in the fibrous network, we expect their mechanistic origin, namely the sliding and merging events may have a profound impact on the bulk properties of the collagen matrix. To examine this effect, we studied the history-dependence of the relaxation dynamics of the model networks under macroscopic shear deformation using a parallel plate rheometer. We held the matrix at an initial shear strain for a dwell time of T_d to allow plastic reconfiguration. We then released the boundary stress and monitored the strain relaxation as a function of time $\varepsilon(t)$ (see Materials and Methods 4.4.2 and 4.4.3).

Since both viscoelastic and plastic dynamics are present, we begin by studying
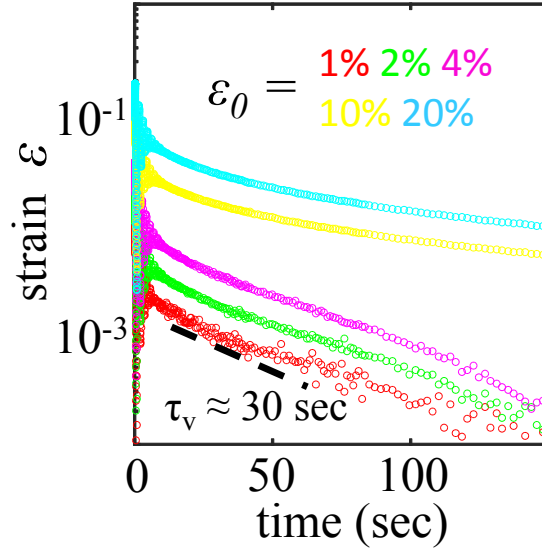
Figure 4.4: Bulk relaxation experiments show strain relaxation kinetics $\varepsilon(t) - \varepsilon(\infty)$ depend on the initial strain, and at small initial strains, the relaxation follows a single exponential function. $\varepsilon(\infty)$ is the residual strain after relaxation.

the relaxation from small initial strains. In this case stress is also small and we expect few sliding events and mostly viscoelastic relaxation. Indeed, we find that up to $\varepsilon_0 < 5\%$, the strain kinetics can be well characterized by a single exponential function with a time scale $\tau_v \approx 30$ seconds, presumably determined by viscoelasticity of the matrix. This is shown in Figure 4.4 by plotting $\varepsilon(t)$ in log scale. However, when the initial strain approaches a threshold ($\approx 10\%$) of linear elasticity, or beyond, a single exponential is no longer sufficient. Under such conditions we expect the relaxation to be dominated by viscoelasticity at short time scales and plasticity at longer time scales.

Indeed, as shown in Figure 4.5A, when collagen matrices relax from 20% initial strain, the relaxation kinetics fit well with double-exponential functions $\varepsilon(t) =$

$a \exp(-t/\tau_v) + b \exp(-t/\tau_p) + \varepsilon_r$. Here $\tau_v =$ 29.6 sec is independent of the dwell time T_d (see Materials and Methods 4.4.4), and matches well with the viscoelastic time scale obtained from small strain relaxation kinetics in Figure 4.4. Consistent with our model assumption, τ_p is well separated from τ_v by an order of magnitude.

We also use our microscopic model, based on sliding and merging of fibers, to simulate the bulk relaxation. As in the experiment, a 20% strain is applied for some T_d. Once the network is released the shear strain drops from $\varepsilon_0 =$ 20% to a non-zero value $\varepsilon(0^+)$ due to purely elastic relaxation. Because we do not consider viscosity effects in our model, this initial drop happens instantaneously. In a real collagen matrix, viscoelasticity due to the collagen-solution interaction and filament entanglement necessarily exist. However it is known that the viscoelasticity time scale is below 1 min and much shorter than the plasticity time scale we discuss here [125, 126]. Thus we ignore viscoelasticity in our modeling and only focus on plastic events including sliding and merging.

We find the subsequent decay of strain follows a single exponential function $\varepsilon(t) = (\varepsilon(0^+) - \varepsilon_r) \exp(-t/\tau_p) + \varepsilon_r$ for $t > 0$ and that the decay is slower with increasing dwell time, T_d, (Figure 4.5B). Because longer dwell time, T_d, allows the network to reduce the number of high-stress bonds through sliding events, we expect a negative correlation between T_d and $1/\tau_p$, the rate of plastic relaxation. Indeed, we have confirmed that both τ_p and ε_r increase monotonically with longer dwell time T_d (Figure 4.5C-D), as predicted by the model.

We also ran experiments in which a new sample was used for each dwell time so that no residual strain or alignment of fibers from previous strains will affect
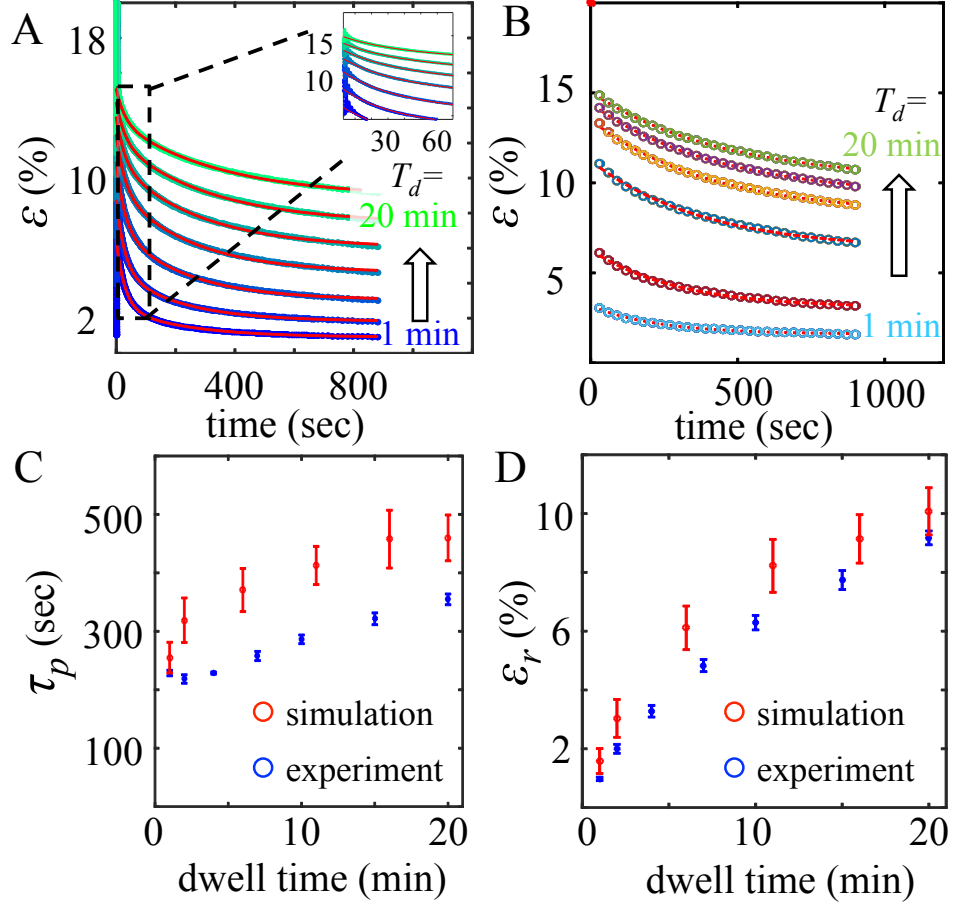
Figure 4.5: Bulk relaxation kinetics of collagen matrices. (A) Experiments show strain relaxation kinetics depends on the dwell time T_d. Colors of the symbols (blue to green) correspond to the increasing dwell time of 1, 2, 4, 7, 10, 15, 20 minutes. Red lines are fit to double exponential functions $\varepsilon(t) = a \exp(-t/\tau_v) + b \exp(-t/\tau_p) + \varepsilon_r$. Here τ_v is independent of dwell time T_d, τ_p and ε_r are allowed to vary with T_d. Inset: zoom-in to the initial phase of the relaxation. (B) Simulated strain decay kinetics with 20% initial strain and varying dwell times $T_d = 1, 2, 6, 10, 16, 20$ minutes. The dashed lines are fits to a single exponential. (C) The plastic time scale τ_p as a function of dwell time T_m. (F) The residual strain ε_r as a function of dwell time T_d. Errorbars in (C) and (D) are means and standard deviations from eight different samples, three experimental and five simulated.

the relaxation dynamics. Figure 4.6A shows the curves for relaxation from a 20% strain applied for five different dwell times from 1 to 20 minutes. No global τ_1 was used due to every experiment being run on a new sample. Instead, each recovery curve was independently fit for both time constants. The experiment was run on three independent samples for each dwell time. Figure 4.6B shows the second time constant τ_2, and Figure 4.6C shows the residual strain ε_r averaged over the three experiments. Error bars show the standard deviation. The results are qualitatively the same as Figure 4.5 in which a single sample was used for each dwell time, with the second time constant and the residual strain both increasing with dwell time.

Together, the experimental and computational results show that the collagen matrix exhibits history-dependent strain relaxation, and that the relaxed state is a permanent reconfiguration of the original matrix.

4.2.4 Plastic Deformation Alters ECM Micromechanics

After demonstrating the effects of microscopic plasticity on the structural remodeling of collagen ECM at both cellular and macroscopic scales, we have also examined the accompanying changes in the ECM micromechanical properties using similar methods as described in Chapter 3 [80]. To this end, we have embedded probe microparticles in collagen matrices together with MDA-MB-231 cells. After more than 3 hours of mauration time we released the cell traction forces with Cytocytochalasin-D, leaving only the plastic deformations. Using holographic optical tweezers [127], we measured the directional compliance $J(\theta)$ from probe par-
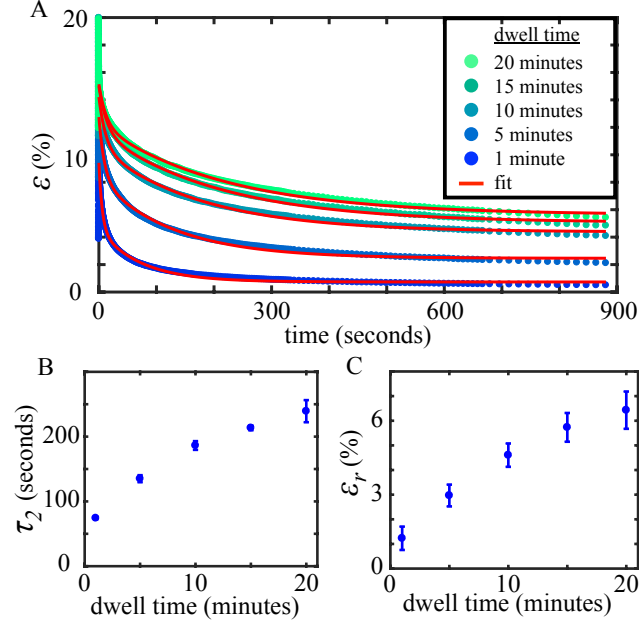
Figure 4.6: Characterization of relaxation dynamics when a new sample is used for every dwell time. (A) Strain recovery curves from 20% strain applied for 1, 5, 10, 15, and 20 minutes. All curves are from different samples which had not been previously strained. (B) Second time constant τ_2 versus dwell time. (C) Residual strain ε_r versus dwell time. Error bars show standard deviation of three independent experiments.

ticles within 80 μm of collagen bundles. Here θ represents the direction along which small optical forces ($\sim pN$) are applied. $J(\theta)$ is defined as $J(\theta) = 6\pi a \frac{\Delta d_\theta}{F_\theta}$, where a is the particle radius, Δd_θ and F_θ are the particle displacement and optical force in the θ direction respectively (Figure). For linear elastic materials, $J(\theta)$ is equal to the elastic compliance. Figure 4.7 illustrates the definition of a directional compliance based on the particle displacement caused by the optical trap.

For each probe particle around the collagen bundle, we measured the directional
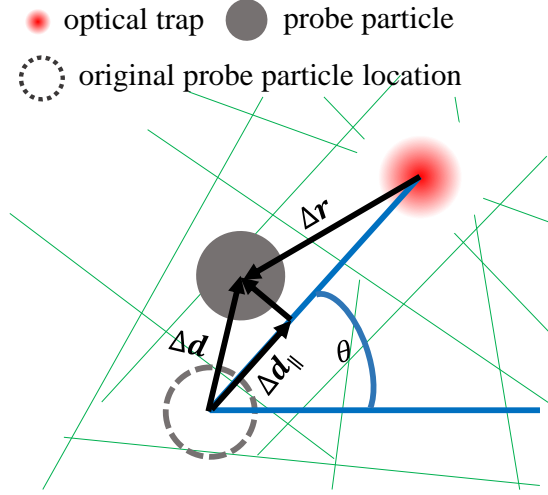
Figure 4.7: Illustration of directional compliance. The angle θ is the direction of the optical trap displacement. The directional complance is calculated using the component of the particle displacement in the direction of the trap ($\Delta d_{||} = \Delta d_{\theta}$).

compliance at 30 degree increments in θ, and the resulted directional compliance $J(\theta)$ was fitted with an ellipse (compliance ellipse) using J as a polar distance. The aspect ratio of the compliance ellipse quantifies the local mechanical anisotropy. Typical results for three different particles are shown in Figure 4.8.

The characteristics of $J(\theta)$ show that the presence of collagen bundles significantly contributes to the micromechanical heterogenity in the ECM. Figure 4.9A shows typical measurements around a collagen bundle (green line) between two MDA-MB-231 cells (white outlines). To better visualize the spatial pattern of the micromechanics, in Figure 4.9A we overlaid the confocal reflection image with the measured directional compliance (magenta dots) and their elliptical fits (red dashed lines). The compliance is scaled linearly into a closed curve centered around each probe particle (the scaling factor is indicated by the bottom right
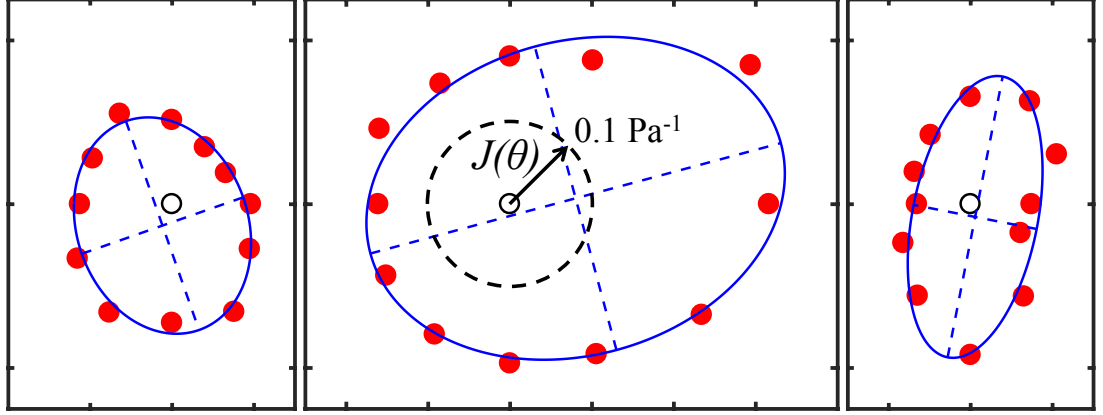
Figure 4.8: Polar compliance plots for three typical particles embedded around collagen bundles. The black circles represent the origin of the polar coordinate system for each particle. The red dots represent the directional compliance $J(\theta)$, with the polar angle giving the direction of the trap and the radial distance from the origin showing the magnitude of the compliance in that direction. Blue lines show the result of fitting $J(\theta)$ with an ellipse. Dashed blue lines are major and minor axes of the fitted ellipse.

circle). We find the particle on the collagen bundle gives a highly anisotropic local compliance, with approximately twice more compliance in the direction perpendicular to the bundle than parallel. This is expected because collagen bundles consist of aligned fibers whose bending elasticity is softer compared with stretching. Moving away from collagen bundle, the micromechanical compliance becomes increasingly isotropic. This is evident from Figure 4.9A, and is also confirmed by sampling multiple bundles. Fig. 4.9B shows the aspect ratios of the compliance ellipses at various particle-to-bundle distances d. Close to collagen bundles ($d < 25$ μm), the aspect ratio is significantly higher than the values measured further away ($25 \leq d < 50$ μm and $50 \leq d < 75$ μm) from the bundles.
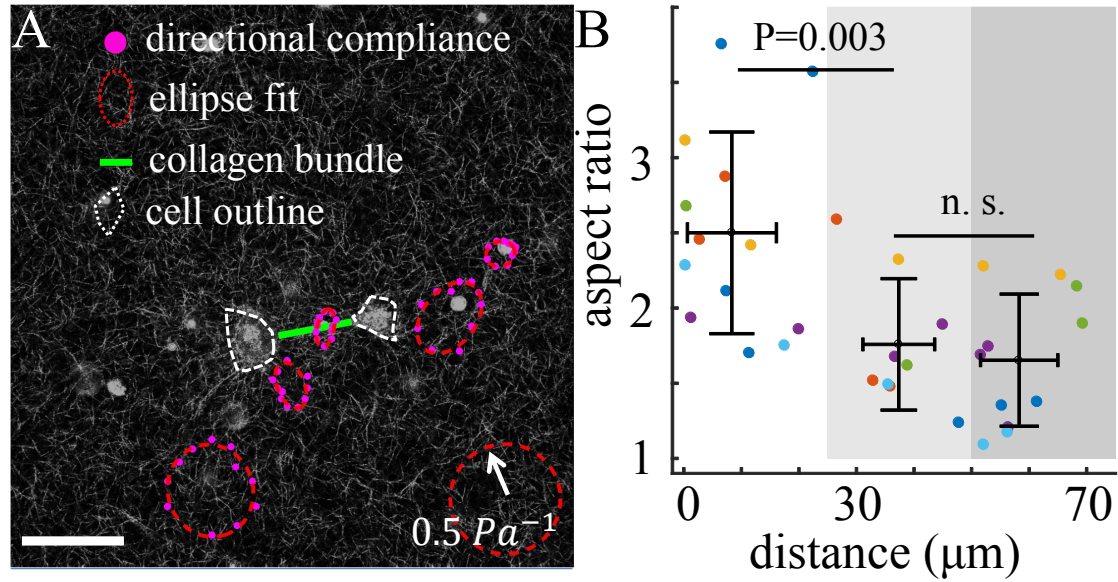
Figure 4.9: The micromechanics of collagen ECM in the vicinity of cell-induced collagen bundles after traction forces are released. (A) The confocal reflection image and directional compliance given by five probe particles around a collagen bundle in a typical experiment. The compliance is scaled linearly into real space such that an isotropic response of 0.5 Pa^{-1} would be plotted as a ring with the size of the bottom right circle. Magenta dots: experimentally measured directional compliance. Red circles: the compliance ellipse, i.e. the elliptical fit to the magenta dots. White dashed lines: outlines of MDA-MB-231 cells after Cytocytochalasin-D treatment. Green line: the location of collagen bundle. Scale bar: 50 μm. (B) The aspect ratios of the compliance ellipses at varying particle-to-bundle distances d. Symbols of different colors correspond to results measured around different bundles. We divide all the data into three groups $d < 25$ μm, $25 \leq d < 50$ μm, and $50 \leq d < 75$ μm. Errorbars represent the means and standard deviations of each group. ANOVA analysis shows that the aspect ratios close to the collagen bundles ($d < 25$ μm) are significantly higher than the values further away.

4.3   Discussion

We have demonstrated that traction forces from cell pairs are capable of locally remodeling 3D collagen ECM into densified, aligned fiber bundles. Rather than being small perturbations to the ECM, as typically assumed for the cell traction forces, fiber density in the bundle region increases dramatically (by as much as 150 %), which is comparable with previous observations of ECM remodeling by clusters of cells [34, 119]. The micromechanics of the ECM is also significantly modified, with greater mechanical anisotropy close to the collagen bundles. These results suggest that collagen ECM is highly susceptible to mechanical remodeling by the cells.

While the formation of collagen bundles would occur for reversible elastic deformations, either linear or non-linear [70], we find that collagen bundles persist even after cell traction forces are removed. Therefore the collagen bundles are cell-induced permanent deformations of the ECM, which is only possible if the collagen matrix is plastic. To understand the implications of ECM plasticity, we devised a computational model based on irreversible sliding and merging of fibers under stress in a model network. Our model not only reproduces the irreversible structural remodeling by cell traction forces, but also agrees with bulk rheological measurements on collagen gels.

While sliding and merging events produce good agreement with experiment, we could also consider other sources of ECM plasticity. Each collagen fiber consists of several weakly bound parallel fibrils. Stretching of fibers causes sliding between

fibrils, which permanently lengthen the fiber. Intrafibrillar sliding has been shown to contribute the history-dependent elasticity of collagen gels, particularly when the gels are probed under repeated stress-relaxation cycles [47]. Although fiber lengthening is likely to occur in our experiments, it does not explain the densified and aligned collagen bundles between cells, nor would it lead to residual strains after bulk shearing. However, the collagen matrix used in our study is a network of fibers that interact noncovalently. Weak interactions, such as hydrogen bonds and electrostatic interactions allow force-dependent unbinding and rebinding between collagen fibers [49], which is similar to the sliding events we have proposed here. These dynamic bonds have been shown to contribute to the plasticity of collagen matrix *in vitro*, as well as for isolated mouse tissues [120]. Interestingly, while it was found that higher strain magnitude leads to faster stress relaxation in collagen matrix [49], we show that the strain relaxation is slowed down by longer dwell time. This apparent contrast highlights the complex strain-stress relation of collagen matrices, a very direct consequence of plasticity.

As the major component of connective tissues, and a semiflexible, subisostatic polymer network, the collagen matrix demonstrates nonlinear elasticity which can be controlled by external stress or strain [124]. This mechanical reconfigurability is further expanded by the stress-activated plasticity reported here. We expect future studies will take advantage of these effects to establish collagen matrix as a mechanically programmable material which has excellent biocompatibility [61, 128]. The plasticity of collagen matrix also implies a new mode of 3D cell-cell interaction in tissues: the collagen bundle from a pair of cells poses microstructural

guidance to nearby cells through contact guidance [129, 130, 131]; and at the same time creates micromechanical guidance to nearby cells through durotaxis [132, 133]. Such interactions are nonlocal and long-lasting, and we expect them to have direct impact on the multicellular dynamics in various physiological processes such as cancer metastasis, wound healing and embryo development [134].

4.4   Materials and Methods

4.4.1   Sample preparation and imaging

Cell-embedded collagen gels are prepared by diluting and neutralizing high concentration type-I collagen solution (10 mg/ml, Corning) with NaOH, cell suspension, growth medium, and 10X PBS into 1.5 mg/ml. The neutralized solution is immediately placed in a tissue culture incubator (NuAire) to polymerize at 37 °C for 40 minutes.

To image the fluorescently-labeled MDA-MB-231 cells cultured in collagen gel, we use a laser point-scanning confocal microscope (Leica SPE) equipped with an stage-top incubator (ibidi). Both fluorescent and reflection channels are imaged with either 20X or 40X oil immersion lenses as described previously [135]. The samples are kept in the tissue culture incubator until the time to image. It usually takes less than 10 minutes to locate the collagen bundles under the microscope.

To release cell traction force, we dilute Cytochalasin-D (Sigma-Aldrich) with PBS to a 1:1000 ratio and add directly to the 3D culture samples. We allow 2

hours to complete the treatment before washing the sample with growth medium.

4.4.2   Collagen Rheology

We prepare the gel between the two parallel plates of an AR-2000 or AR-G2 stress-controlled rheometer (TA Instruments) at 37 °C and concentration of 1.5 mg/ml. A Peltier plate with solvent trap is used and the edges of the sample are sealed with silicone oil to prevent evaporation. The plates are stainless-steel, and surface treated with CellTak (Corning) to ensure binding to the collagen.

We monitor the gelation of each sample by measuring the shear modulus once per minute using a small amplitude oscillatory shear strain. We begin taking data immediately after the neutralized collagen solution is added to the pre-heated plates of the rheometer, and each sample gels for at least 90 minutes total. Figure 4.10A shows the shear modulus vs time during gelation for a typical collagen sample.

To characterize the nonlinear elasticity of a collagen gel, we measure the shear modulus versus strain amplitude for strains up to 100% (Figure 4.10B). All measurements were taken at a frequency of 1 Hz. Strain stiffening begins around 10% strain shown by an increase in the modulus. The modulus continuously increases with strain amplitude until around 60% strain. At this point the modulus suddenly decreases indicating network yield. The vertical dashed line if Figure 4.10B shows 20% strain, the magnitude used for the experiments on recovery versus dwell time described in the main text. This strain is just inside the beginning of the nonlinear
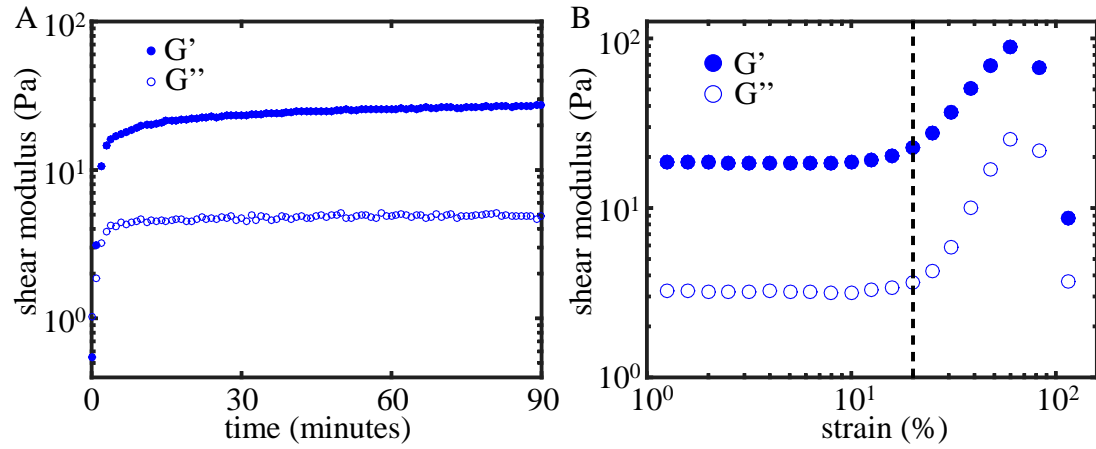
Figure 4.10: (A) Temporal characterization of the gelation process for a typical collagen gel. The complex shear modulus is measured once per minute using a 0.5% oscillatory strain with a frequency of 1 Hz and the total gelation time is 90 minutes. (B) Shear modulus versus strain amplitude. Strain stiffening begins to appear around 10% strain and the sample yield is around 60%. The vertical dashed line shows 20% strain.

elastic region.

4.4.3   Measurement of the Bulk Relaxation Kinetics

To explore the effects of collagen plasticity on the relaxation dynamics of collagen gel, we designed in experiment in which we apply a fixed strain for some dwell time T_d. After this dwell time, the stress σ is set to zero and the strain ε is recorded for the recovery of the gel. Figure 4.11A shows a single strain, dwell, and recovery cycle for a typical experiment. To measure the dependence of strain relaxation on dwell time, these cycles are repeated on the same sample for various dwell times. Figure 4.11B shows a typical experiment in which the strain is applied
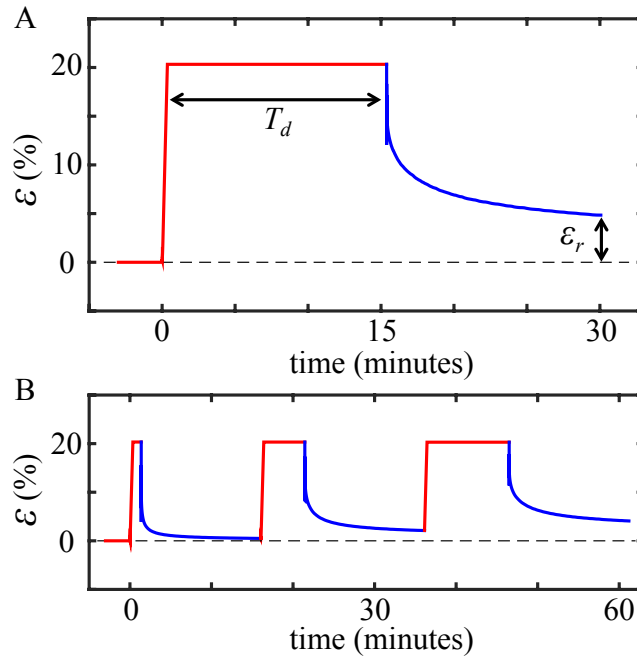
Figure 4.11: Strain versus time for typical history-dependent relaxation experiments. (A) Single strain, dwell, recovery cycle showing the recovery time T_d and the residual strain ε_r. (B) Repeated strain, dwell, recovery cycles with increasing dwell time. Red lines indicate parts when a fixed strain is applied, and blue lines indicate when stress is set to zero ($\sigma = 0$) and the recovery strain is measured.

repeatedly. Typically, the dwell time starts from 1 minute and gradually increases to 20 minutes for each given sample. The initial strains are applied by shearing the sample at 1% per second, until reaching the desired strain magnitudes. For each dwell time, we allow 15 minutes of relaxation before bringing the sample back to the desired strain.

4.4.4 Fitting Bulk Relaxation Kinetics

To fit the relaxation kinetics, we use the Matlab nonlinear curve fitting package to fit the strain versus time to a double exponential function $\varepsilon(t) = a \exp(-t/\tau_v) + b \exp(-t/\tau_p) + \varepsilon_r$.

Of the two time constants characterizing the strain recovery of collagen gel, only the larger time constant, τ_2 should depend on the dwell time. The smaller time constant, τ_1, should be the same for all recovery curves. To find a single τ_1 which best fits the data, we fix τ_1 to be the same for all dwell times, fit each recovery curve for the remaining parameters, and then calculate the total mean squared error. We define the total mean squared error (MSE_{tot}) as the sum of the individual mean squared error for each dwell time. So $MSE_{tot} = \sum MSE_{T_d}$ and $MSE_{T_d} = \frac{1}{n} \sum_{i=1}^{n} (\hat{\varepsilon}_i - \varepsilon_i)^2$, where T_d is the dwell time, ε is the data and $\hat{\varepsilon}$ is the fit. By repeating this for many different τ_1, we find a single global τ_1 which best fits all the data. Figure 4.12 shows the total mean squared error versus τ_1 for a typical experiment. The red circle in the figure shows the chosen τ_1, which does indeed give a global minimum for the error.
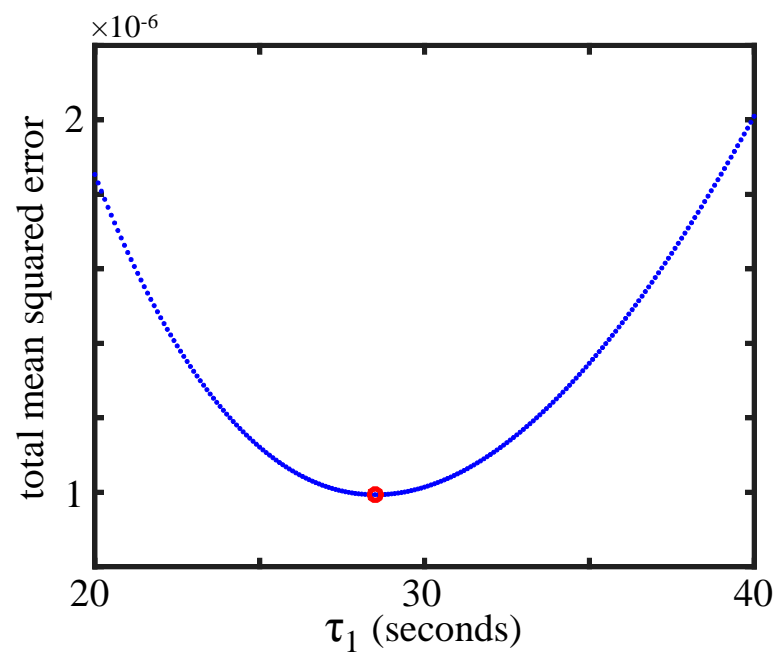
Figure 4.12: Total mean squared error (MSE_{tot}) verses global τ_1. The red circles shows the final τ_1 gives a minimum in MSE_{tot}.

5   Conclusion

We have presented new experimental and computational results on the structure and mechanics of the extracellular matrix (ECM) at the microsopic scale. Mechanical cues from the ECM have a large effect on many important cell processes such as growth and migration. Cells directly probe the local properties of the collagen fiber network, thus micromechanics of the ECM have a more direct effect on cell behavior than bulk averaged properties of the matrix. The results of this research contribute to the fundamental understanding of cell-ECM interactions and also provide techniques that can be used for further studies.

In Chapter 2 we used confocal reflection microscopy along with image analysis based on spatial correlations to characterize the structure of type I collagen gels. Using the density and nematic order correlation functions we were able to quantify geometric properties of the matrix as well as how they fluctuate spatially. The double exponential decay of the density correlation function revealed two length scales, the shorter corresponding to the thickness of individual collagen fibers and the longer corresponding to the size of fiber clusters. The nematic order provided a means of quantifying the degree of alignment between nearby fibers. These properties are not revealed in collagen characterizations based on pore size or turbidity. We studied the effect of gelation temperature on the final structure of the collagen gel and find that collagen formed at high temperature has short thin

fibers, small clusters distributed relatively homogeneously, and a very small degree of local alignment. However, fiber networks formed at low temperature are very heterogeneous with large aligned fiber clusters.

We presented a computational model for collagen growth to explain these results. The model is based on the nucleation of small fiber seeds, which diffuse around and grow, until they bind with other fibers into clusters. These clusters in turn diffuse, grow, and bind with one another until the final network structure is achieved. In addition, nearby collagen fibers have a tendency to align with one another due to hydrodynamic effects. The nucleation and growth rates both monotonically increase with temperature, meaning that at higher temperature many seeds form and grow quickly and do not have as much time to align or cluster together. At low temperature, fibers form and grow slowly, meaning they have more time to diffuse around and interact to form larger aligned clusters.

These results demonstrate the effect of environmental conditions during gelation on the final network structure and may suggest the possibility of tuning the properties of collagen gels. By varying temperature during gelation, one is able to control the microstructure of the ECM. These changes would in turn affect cell behaviors, like migration. In addition, pH also has an effect on the growth of the collagen network. This was not studied in our characterization, but could be a topic for further investigation. Also, flow within the collagen solution during gelation has also been shown to produce aligned collagen fibers. Through the combined control of collagen concentration, temperature, pH, and flow, one may be able to engineer collagen gels capable of guiding cell behavior.

In Chapter 3 we extended our study of collagen-based ECM from purely structural to mechanical. We used holographic optical tweezers (HOT) to probe microscopic particles embedded in the collagen gel and revealed rich mechanics beyond the typical rheological measurements. Specifically, we find a directional dependence to the local compliance that is anisotropic and asymmetric. This mechanical response is due to the discrete fibers that make up the collagen matrix and is highly dependent on the network microstructure.

We characterized gels made at different temperatures to show that ECM microstructure has a strong effect on the micromechanical response. High temperature gels, which are relatively homogeneous and have a small pore size, show a tight distribution of local compliance and a smaller variance in anisotropy. In this case, the approximation of a continuous linearly elastic material does fairly well to represent the local mechanics. However, in low temperature gels which are very heterogeneous and have a large pore size, we get a very broad distribution of micromechanical responses. This means that any bulk measurement would be a poor predictor for the local mechanics. The variablility of the cell microenvironment means that each cell may experience a very different network compliance and could lead to diverse cell behavior within the same 3D collagen matrix.

We showed that active cell traction forces altered the local micromechanics, and these effects can be detected as far away as $\sim100\mu$m from the cell. This means that cells could detect changes in the environment due to nearby cells, providing a means of mechanical communication. The change in micromechanics was closely correlated with the local cell-induced strain, again highlighting the

close relationship between network structure and mechanics. We also presented a simple 2D lattice based model for collagen gel which is able to reproduce the experimental results for both cell free and cell-populated collagen gels.

In Chapter 4 we extended our mechanical characterization of biopolymer networks to study the plasiticity of collagen-based ECM. We showed that single pairs of cells are able to pull collagen into densified and aligned bundles. While purely elastic effects could account for an increase in density and fiber alignment between contracting cells, it cannot account for the fact that the collagen bundles are permanent, meaning they remain even after removing cell traction forces. Nor could elastic effects alone account for the magnitude of increase in density (as much as 150%) as collagen appears to flow into the region between the cells. We have used the HOT system described in Chapter 3 to measure the micromechanics around the collagen bundles and found that the plastic deformations significantly alter the micromechanics. Specifically, we find a higher degree of anisotropy close to the bundles, consistent with a higher degree of alignment of the collagen fibers.

We have shown that plastic deformation of collagen is purely mechanical, and can occur even in the absense of cells. To further investigate the mechanical nature of collagen plasticity, we performed macroscopic shear experiments using a parallel plate rheometer. By applying a shear strain above the linear elastic limit of the collagen gel we were able to show that macroscopic strain does lead to irreversible deformation. In addition, we showed that the bulk relaxation of collagen is history-dependent such that the residual strain and the relaxation dynamics depend on the dwell time for which the strain was applied.

To explain ECM plasticity, we presented a model based on the sliding and merging of fibers within the collagen matrix. Weak bonds between fibers, such as hydrogen bonds and electrostatic interactions, are able to break when under enough stress, allowing the fibers to slide to a lower stress state. At a longer time scale, merging of fibers occurs as bonds reform. This microscopic model for biopolymer plasticity was able to reproduce the results of both cell-induced formation of collagen bundles and the relaxation kinetics of bulk collagen under shear strain. The model explains why the relaxation rate decreases with dwell time. When the strain is applied for longer periods, more of the high stress bonds will break. When the external stress is removed and the collagen is free to relax, there are fewer stressed bonds wanting to restore it to the original equilibrium position. Thus, the rate of relaxation is slower. In addition, some of the bonds that broke under stress will be able to form new bonds, meaning that the new equilibrium configuration of the network will change. This causes the residual strain.

The above results show that the structure and mechanics of biopolymer networks can be significantly and irreversibly affected by external stress and strain. Together with the environmental factors previously mentioned, stress-induces plasticity opens new possibilities for engineering cell microenvironments. In addition to having excellent biocompatibility, collagen material properties can be tuned by mechanical means, even after the gel has fully polymerized.

Finally, collagen plasticity has huge implication for 3D cell communication and migration. The formation of permanent collagen bundles can form a direct line for mechanical interactions between cells. For example, the increase in fiber density in

the collagen bundles may be able to direct cell migration through durotaxis, and the fiber alignment may direct cells through contact guidance. Future studies will be needed to investigate the effects of ECM remodeling on cell behavior.

Mechanical interactions between cells and their microenvironments are both complex and dynamic. At the same time that cells are sensing and responding to their surroundings, they are actively remodeling the structure and mechanics of the extracellular matrix. This continual process is critical for tissue homeostasis and collective cell behaviors. Future research into the fundamental mechanics of cell adhesion and migration is critical if we are to better understand biological processes like cancer progression and metastasis.

Bibliography

[1] J. D. Humphrey, E. R. Dufresne, and M. A. Schwartz. Mechanotransduction and extracellular matrix homeostasis. *Nat. Rev. Mol. Cell. Biol.*, 15:802–812, 2014.

[2] D. A. Fletcher and R. D. Mullins. Cell mechanics and the cytoskeleton. *Nature*, 463(7280):485–492, 2010.

[3] Jr. R. J. Pelham and Y. Wang. Cell locomotion and focal adhesions are regulated by substrate flexibility. *Proc. Nat. Acad. Sci.*, 94(25):13661–13665, 1997.

[4] T. Yeung, P. C. Georges, L. A. Flannagan, B. Marg, M. Ortiz, M. Funaki andN. Zahir, W. Ming, V. Weaver, and P. A. Janmey. Effects of substrate stiffness on cell morphology, cytoskeletal structure, and adhesion. *Cell Motil. Cytoskeleton*, 60(1):24–34, 2005.

[5] A. J. Engler, S. Sen, H. L. Sweeney, and D. E. Discher. Matrix elasticity directs stem cell lineage specification. *Cell*, 126(4):677–689, 2006.

[6] K. R. Levental, H. Yu, L. Kass, J. N. Lakins, M. Egeblad, J. T. Erler, S. F. T. Fong, K. Csiszar, A. Giaccia, W. Weninger, M. Yamauchi, D. L. Gasser, and V. M. Weaver. Matrix crosslinking forces tumor progression by enhancing integrin signaling. *Cell*, 139:891–906, 2009.

[7] R. W. Tilghman, C. R. Cowan, J. D. Mih, Y. Koryakina, D. Gioeli, J. K. Slack-Davis, B. R. Blackman, D. J. Tschumperlin, and J. T. Parsons. Matrix rigidity regulates cancer cell growth and cellular phenotype. *PLos ONE*, 5(9):e12905, 2010.

[8] E. Hadjipanyi, V. Mudera, and R. A. Brown. Guided cell migration in 3D: A collagen matrix with graded directional stiffness. *Cell Motil. Cytoskeleton*, 66:121–128, 2009.

[9] S. Guido and R. T. Tranquillo. A methodology for the systematic and quantitative study of cell contact guidance in oriented collagen gels: Correlation of fibroblast orientation and gel birefringence. *J. Cell Sci.*, 105:317–331, 1993.

[10] P. P. Provenzano, D. R. Inman, K. W. Eliceiri, S. M. Trier, and P. J. Keely. Contact guidance mediated three-dimensional cell migration is regulated by rho/rock-dependent matrix reorganization. *Biophys. J.*, 95:5374–5384, 2008.

[11] C. Bonnans, J. Chou, and Z. Werb. Remodelling the extracellular matrix in development and disease. *Nat. Rev. Mol. Cell Biol.*, 15:786–801, 2014.

[12] X. Ma, M. E. Schickel, M. D. Stevenson, A. L. Sarang-Sieminski, K. J. Gooch, S. N. Ghadiali, and R. T. Hart. Fibers in the extracellular matrix enable long-range stress transmission between cells. *Biophys. J.*, 104:1410–1418, 2013.

[13] T. Lecuit, P. Lenne, and E. Munro. Force generation, transmission and integration during cell and tissue morphogenesis. *Annu. Rev. Cell Dev. Biol.*, 27:157–184, 2011.

[14] G. Totsukawa, Y. Wu, Y. Sasaki, D. J. Hartshorne, Y. Yamakita, S. Yamashiro, and F. Matsumura. Distinct roles of MLCK and ROCK in the regulation of membrane protrusions and focal adhesion dynamics during cell migration of fibroblasts. *J. Cell Biol.*, 164:427–439, 2004.

[15] P. Friedl and D. Gilmour. Collective cell migration in morphogenesis, regeneration and cancer. *Nat. Rev. Mol. Cell Biol.*, 10:445, 2009.

[16] S. B. Lindström, D. A. Vader, A. Kulachenko, and D. A. Weitz. Biopolymer network geometries: Characterization, regeneration and elastic properties. *Phys. Rev. E*, 82:051905, 2010.

[17] Y. L. Yang, S. Motte, and L. J. Kaufman. Pore size variable type I collagen gels and their interaction with glioma cells. *Biomaterials*, 31(21):5678–5688, 2010.

[18] J. Zhu and L. J. Kaufman. Collagen I self-assembly: Revealing the developing structures that generate turbidity. *Biophys. J.*, 106:1822–1831, 2014.

[19] Y. Jiao and S. Torquato. Quantiative characterization of the microstructure and transport properties of biopolymer networks. *Phys. Biol.*, 9:036009, 2012.

[20] Y. Yang, L.M. Leone, and L. J. Kaufman. Elastic moduli of collagen gels can be predicted from two-dimensional confocal microscopy. *Biophys. J.*, 97:2051–2060, 2009.

[21] P. Ronceray, C. P. Broedersz, and M. Lenz. Fiber networks amplify active stress. *Proc. Natl. Acad. Sci.*, 113(11):2827–2832, 2016.

[22] PubMedHealth. Connectivetissue.

[23] A. S. Narayanan, R. C. Page, and J. Swanson. Collagen synthesis by human fibroblasts. Regulation by transforming growth factor-β in the presence of other inflammatory mediators. *Biochemical Journal*, 260:463, 1989.

[24] J. D. Mott and Z. Werb. Regulation of matrix biology by matrix metallo-proteinases. *Curr. Opin. Cell Biol.*, 16:558, 2004.

[25] A. J. Ridley, M. A. Schwartz, K. Burridge, Richard A. Firtel, M H. Ginsberg, G. Borisy, J. T. Parsons, and A. R. Horwitz. Cell migration: Integrating signals from front to back. *Science*, 302:1704–1709, 2003.

[26] R. J. Petrie and K. M. Yamada. At the leading edge of three-dimensional cell migration. *J. Cell Sci.*, 125:1–10, 2013.

[27] R. Fernandez-Gonzalez, M. S. Simoes, J. C. Röper, S. Eaton, and J. A. Zallen. Myosin II dynamics are regulated by tension in intercalating cells. *Dev. Cell*, 17:736–743, 2009.

[28] M. A. Wozniak and C. S. Chen. Mechanotransduction in development: a growing role for contractility. *Nat. Rev. Mol. Cell Biol.*, 10(1):34–43, 2009.

[29] S. Wong, W. Guo, and Y. Wang. Fibroblasts probe substrate rigidity with filopodia extensions before occupying an area. *Proc. Nat. Acad. Sci.*, 111(48):17176–17181, 2014.

[30] D. E. Jaalouk and J. Lammerding. Mechanotransduction gone awry. *Nat. Rev. Mol. Cell Biol.*, 10:63–73, 2009.

[31] M. W. Pickup, J. K. Mouw, and V. M. Weaver. The extracellular matrix modulates the hallmarks of cancer. *EMBO Rep.*, 15:1243–1253, 2014.

[32] M. J. Paszek, N. Zahir, K. R. Johnson, J. N. Lakins, G. I. Rozeneberg, A. Gefena, C. A. Reinhart-King, S. S. Marqulies, M. Dembo, D. Boettiger, D. A. Hammer, and V. M. Weaver. Tensional homeostasis and the malignant phenotype. *Cancer Cell*, 8(3):241–254, 2005.

[33] H. Wang, A. S. Abhilash, C. S. Chen, R. G. Wells, and V. B. Shenoy. Long-range force transmission in fibrous matrices enabled by tension-driven alignment of fibers. *Biophysical journal*, 107(11):2592–2603, 2014.

[34] Q. Shi, R. P. Ghosh, H. Engelke, C. H. Rycroft, L. Cassereau, J. A. Sethian, V. M. Seaver, and J. T. Liphardt. Rapid disorganization of mechanically interacting systems of mammary acini. *Proc. Nat. Acad. Sci.*, 111(2):658–663, 2014.

[35] A. Kurtz and S. Oh. Age related changes of the extracellular matrix and stem cell maintenance. *Preventive Medicine*, 54:S50–56, 2012.

[36] T. R. Cox and J. T. Erler. Remodeling and homeostasis of the extracellular matrix: Implications for fibrotic diseases and cancer. *Dis. Model Mech.*, 4(2):165–178, 2011.

[37] J. J. Tomasek, G. Gabbiani, B. Hinz, C. Chaponnier, and R. A. Brown. Myofibroblasts and mechano-regulation of connective tissue remodelling. *Nat. Rev. Mol. Cell Biol.*, 3(5):349–363, 2002.

[38] A. O. Brightman, B. P. Rajwa, J. E. Sturgis, M. E. McCallister, J. P. Robinson, and S. L. Voytik-Harbin. Time-lapse confocal reection microscopy of collagen fibrillogenesis and extracellular matrix assembly in vitro. *Biopolymers*, 54:222–234, 2000.

[39] D. Vader, A. Kabla, D. Weitz, and L. Mahadevan. Strain-induced alignment in collagen gels. *PLos ONE*, 4(6):e5902, 2009.

[40] F. J. O'Brien, B. A. Harley, M. A. Waller, I. V. Yannas, L. J. Gibson, and P. J. Prendergast. The effect of pore size on permeability and cell attachment in collagen scaffolds for tissue engineering. *Tech. Health Care*, 15(1):3–17, 2007.

[41] A. Takahashi, R. Kita, T. Shinozaki, K. Kubota, and M. Kaibara. Real space observation of three-dimensional network structure of hydrated fibrin gel. *Colloid Polym. Sci.*, 281:832–838, 2003.

[42] W. Mickel, S. Münster, L. M. Jawerth, D. A. Vader, D. A. Weitz, A. P. Sheppard, K. Mecke, B. Fabry, and G. E. Schröder-Turk. Robust pore size analysis of filamentous networks from three-dimensional confocal microscopy. *Biophys. J.*, 95:6072–6080, 2008.

[43] N. R. Lang, S. Münster, C. Metzner, P. Krauss, S. Schürmann, J. Lange, K. E. Aifantis, O. Friedrich, and B. Fabry. Estimating the 3D pore size distribution of biopolymer networks from directionally biased data. *Biophys. J.*, 105:1967–1975, 2013.

[44] C. B. Raub, A. J. Putnama, B. J. Tromberg, and S. C. George. Predicting bulk mechanical properties of cellularized collagen gels using multiphoton microscopy. *Acta Biomater.*, 6:4657–4665, 2010.

[45] G. Forgacs, S. A. Newman, B. Hinner, C. W. Maier, and E. Sackmann. Assembly of collagen matrices as a phase transition revealed by structural and rheologic studies. *Biophys. J.*, 84:1272–1280, 2003.

[46] S. Motte and L. J. Kaufman. Strain stiffening in collagen I networks. *Biopolymers*, 99(1):35–46, 2012.

[47] S. Münster, L. M. Jawerth, B. A. Leslie, J. I. Weitz, B. Fabry, and D. A. Weitz. Strain history dependence of the nonlinear stress response of fibrin and collagen networks. *Proc. Natl. Acad. Sci.*, 10:12197, 2013.

[48] A. J. Licup, S. Münster, A. Sharma, M. Sheinman, L. M. Jawerth, B. Fabry, D. A. Weitz, and F. C. MacKintosh. Stress controls the mechanics of collagen networks. *Proceedings of the National Academy of Sciences*, 112(31):9573–9578, 2015.

[49] S. Nam, K. H. Hu, M. J. Butte, and O. Chaudhuri. Strain-enhanced stress relaxation impacts nonlinear elasticity in collagen gels. *Proc. Natl. Acad. Sci.*, 113:5492, 2016.

[50] Q. Wen and P. A. Janmey. Effects of nonlinearity on cell-ECM interactions. *Exp. Cell Res.*, 319:2481, 2013.

[51] T. G. Mason, K. Ganesan, J. H. van Zanten, D. Wirtz, and S. C. Kuo. Particle tracking microrheology of complex fluids. *Phys. Rev. Lett.*, 79(17):3282–3285, 1997.

[52] F. Gittes, B. Schnurr, P. D. Olmsted, F. C. MacKintosh, and C. F. Schmidt. Microscopic viscoelasticity: Shear moduli of soft materials determined from thermal fluctuations. *Phys. Rev. Lett.*, 79(17):3286–3289, 1997.

[53] D. Mizuno, D. A. Head, F. C. MacKintosh, and C. F. Schmidt. Active and passive microrheology in equilibrium and nonequilibrium systems. *Macromolecules*, 41:7194–7202, 2008.

[54] M. A. Kotlarchyk, S. G. Shreim, M. B. Alvarez-Elizondo, L. C. Estrada, R. Singh, L. Valdevit, E. Kniazeva, E. Gratton, A. J. Putnam, and E. L. Botvinick. Concentration independent modulation of local micromechanics in a fibrin gel. *PLoS ONE*, 6(5):e20201, 2011.

[55] C. P. Broedersz and F. C. MacKintosh. Modeling semiflexible polymer networks. *Reviews of Modern Physics*, 86(3):995, 2014.

[56] J. Feng, H. Levine, X. Mao, and L. M. Sander. Nonlinear elasticity of disordered fiber networks. *Soft Matter*, 12(5):1419–1424, 2016.

[57] C. Jones, L. Liang, D. Lin, Y. Jiao, and B. Sun. The spatial-temporal characteristics of type I collagen-based extracellular matrix. *Soft Matter*, 10(44):8855–8863, 2014.

[58] H. Lodish, A. Berk, S. L. Zipursky, P. Matsudaira, D. Baltimore, and J. Darnell. *Molecular Cell Biology, 4th Edition*. W. H. Freeman, 2000.

[59] W. J. Matheson and M. Markham. Infantile cortical hyperostosis. *British Medical Journal*, pages 742–744, 1952.

[60] T. Elsdale and J. Bard. Collagen substrata for studies on cell behaviour. *J. Cell Biol.*, 54:626–637, 1972.

[61] R. A. Brown. In the beginning there were soft collagen-cell gels: Towards better 3D connective tissue models? *Exp. Cell Res.*, 319:2460–2469, 2013.

[62] M. Djabourov, J. P. Lechaire, and F. Gaill. Structure and rheology of gelatin and collagen gels. *Biorheology*, 30:191–205, 1993.

[63] C. G. Bellow, A. H. Melcher, and J. E. Aubin. Contraction and organization of collagen gels by cells cultured from periodontal ligament, gingiva and bone suggest functional differences between cell types. *J. Cell Sci.*, 50:299–314, 1981.

[64] Y. Yang and L. J. Kaufman. Rheology and confocal reflectance microscopy as probes of mechanical properties and structure during collagen and collagen/hyaluronan self-assembly. *Biophys. J.*, 96:1566–1585, 2009.

[65] G. Cox, E. Kable, A. Jones, I. Fraser, F. Manconi, and M. D. Gorrell. 3-Dimensional imaging of collagen using second harmonic generation. *J. Struc. Biol.*, 141:53–62, 2003.

[66] R. M. Williams, W. R. Zipfel, and W. W. Webb. Interpreting second-harmonic generation images of collagen I fibrils. *Biophys. J.*, 88(2):1377–1386, 2005.

[67] H. A. Leddy, M. A. Haider, and F. Guilak. Diffusion anisotropy in collagenous tissues: Fluorescence imaging of continuous point photobleaching. *Biophys. J.*, 91:311–316, 2006.

[68] T. Stylianopoulos, B Diop-Frimpong, L. L. Munn, and R. K. Jain. Diffusion anisotropy in collagen gels and tumors: The effect of fiber network orientation. *Biophys. J.*, 99:3119–3128, 2010.

[69] C. P. Broedersz, X. Mao, T. C. Lubensky, and F. C. MacKintosh. Criticality and isostaticity in fiber networks. *Nat. Phys.*, 7:983–8, 2011.

[70] J. Feng, H. Levine, X. Mao, and L. M. Sander. Alignment and nonlinear elasticity in biopolymer gels. *Physical Review E*, 91(4):042710, 2015.

[71] A. P. Chatterjee. A simple model for the pore size distribution in random fibre networks. *J. Phys.: Condens. Matter*, 24(375106), 2012.

[72] P. M. Chaikin and T. C. Lubensky. *Principles of Condensed Matter Physics*. Cambridge University Press, 1995.

[73] S. Torquato. *Random Heterogeneous Materials: Microstructure and Macroscopic Properties*. Springer-Verlag, New York, 2002.

[74] A. Vaziri and A. Gopinath. Cell and biomolecular mechanics in silico. *Nature Materials*, 7:15–23, 2008.

[75] D. Shao, W. J. Rappel, and H. Levine. Computational model for cell morphodynamics. *Phys. Rev. Lett.*, 105:108104, 2010.

[76] D. Shao, H. Levine, and W. J. Rappel. Coupling actin flow, adhesion, and morphology in a computational cell motility model. *Proc. Natl. Acad. Sci. USA*, 109(18):6851–6856, 2012.

[77] D. Gordon, A. Bernheim-Groswasser, C. Keasar, and O. Farago. Hierarchical self-organization of cytoskeletal active networks. *Phys. Biol.*, 9:026005, 2012.

[78] R. M. Ziff and G. Stell. Kinetics of polymer gelation. *J. Chem. Phys.*, 73(7):3492, 1980.

[79] U. A. Stock and J. P. Vacanti. Tissue engineering: Current state and prospects. *Ann. Rev. Med.*, 52:443–451, 2001.

[80] C. A. R. Jones, M. Cibula, J. Feng, E. A. Krnacik, D. H. McIntyre, H. Levine, and B. Sun. Micromechanics of cellularized biopolymer networks. *Proceedings of the National Academy of Sciences*, 112(37):E5117, 2015.

[81] T. Mammoto and D. E. Ingber. Mechanical control of tissue and organ development. *Development*, 137:1407–1420, 2010.

[82] L. G. Griffith and M. A. Swartz. Capturing complex 3D tissue physiology in vitro. *Nat. Rev. Mol. Cell Biol.*, 7:211, 2006.

[83] K. Hotary, E. Allen, A. Punturieri, I. Yana, and S. J. Weiss. Regulation of cell invasion and morphogenesis in a three-dimensional type I collagen matrix by membrane-type matrix metalloproteinases 1, 2, and 3. *J. Cell Biol.*, 149(6):1309–1323, 2000.

[84] F. Grinnell. Fibroblast biology in three-dimensional collagen matrices. *Trends Cell Biol.*, 13(5):264–269, 2003.

[85] RR. J. Petrie, N. Gavara, R. S. Chadwick, and K. M. Yamada. Nonpolarized signaling reveals two distinct modes of 3D cell migration. *J. Cell Biol.*, 197(3):439, 2012.

[86] F. J. O'Brien, B. A. Harley, I. V. Yannas, and L. J. Gibson. The effect of pore size on cell adhesion in collagen-GAG scaffolds. *Biomaterials*, 26(4):433–441, 2005.

[87] B. M. Baker and C. S. Chen. Deconstructing the third dimension - how 3D culture microenvironments alter cellular cues. *J. Cell Sci.*, 125(13):3015–3024, 2012.

[88] Matthew Cibula. *Applications of holographic optical tweezers: Multiplexed fluorescence spectroscopy and the micromechanics of type-I collagen*. PhD thesis, Oregon State University, 2015.

[89] F. C. Cheong, B. Sun, R. Dreyfus, K. Xiao, L. Dixon, and D. G. Grier. Flow visualization and flow cytometry with holographic video microscopy. *Optics Express*, 17:13071–13079, 2009.

[90] R. Parthasarathy. Rapid, accurate particle tracking by calculation of radial symmetry centers. *Nat. Methods*, 9(7):724–726, 2012.

[91] C. R. White and J. A. Frangos. The shear stress of it all: the cell membrane and mechanochemical transduction. *Philos. Trans. R. Soc. Lond. B Biol. Sci.*, 362(14):1459–1467, 2007.

[92] M. Achilli and D. Mantovani. Tailoring mechanical properties of collagen-based scaffolds for vascular tissue engineering: The effects of pH, temperature and ionic strength on gelation. *Polymers*, 2(4):664–680, 2010.

[93] E. Kniazeva, J. W. Weidling, R. Singh, E. L. Botvinick, M. A. Digman, E. Gratton, and A. J. Putnam. Quantification of local matrix deformations and mechanical properties during capillary morphogenesis in 3D. *Integr. Biol.*, 4(4):431–439, 2013.

[94] N. Gjorevski and C. M. Nelson. Mapping of mechanical strains and stresses around quiescent engineered three-dimensional epithelial tissues. *Biophysical Journal*, 103:152–162, 2012.

[95] T. M. Koch, S. Münster, N. Bonakdar, J. P. Butler, and B. Fabry. 3D traction forces in cancer cell invasion. *PLoS ONE*, 7(3):e33476, 2012.

[96] M. Das, F. C. MacKintosh, and A. J. Levine. Effective medium theory of semiflexible filamentous networks. *Physical review letters*, 99(3):038101, 2007.

[97] X. Mao, O. Stenull, and T. C. Lubensky. Effective-medium theory of a filamentous triangular lattice. *Physical Review E*, 87(4):042601, 2013.

[98] A. S. Abhilash, B. M. Baker, B. Trappmann, C. S. Chen, and V. B. Shenoy. Remodeling of fibrous extracellular matrices by contractile cells: predictions from discrete fiber network simulations. *Biophysical Journal*, 107(8):1829–1840, 2014.

[99] D. A. Head, A. J. Levine, and F. C. MacKintosh. Mechanical response of semiflexible networks to localized perturbations. *Physical Review E*, 72:061914, 2005.

[100] C. Heussinger and E. Frey. Force distributions and force chains in random stiff fiber networks. *European Physical Journal E*, 24(1):47–53, 2007.

[101] F. Rehfeldt, A. J. Engler, A. Eckhardt, F. Ahmed, and D. E. Discher. Cell responses to the mechanochemical microenvironment - Implications for regenerative medicine and drug delivery. *Adv. Drug Deliv. Rev.*, 59(13):1329–1339, 2007.

[102] C. M. Cuerrier and A. E. Pelling. *Cells, Forces, and the Microenvironment.* CRC Press, 2015.

[103] H. Baharvand, S. M. Hashemi, S. K. Ashtiani, and A. Farrokhi. Differentiation of human embryonic stem cells into hepatocytes in 2D and 3D culture systems in vitro. *Int. J. Dev. Biol.*, 50:645–652, 2006.

[104] P. A. Kenny, G. Y. Lee, C. A. Myers, R. M. Neve, J. R. Semeiks, P. T. Spellman, K. Lorenz, E. H. Lee, M. H. Barcellos-Hoff, O. W. Petersen, J. W. Gray, and M. J. Bissell. The morphologies of breast cancer cell lines in three-dimensional assays correlate with their profiles of gene expression. *Mol. Oncol.*, 1(1):84–96, 2007.

[105] G. Brouhard, H. Schek, and A. Hunt. Advanced optical tweezers for the study of cellular and molecular biomechanics. *IEEE Trans. Biomed. Eng.*, 50(1):121–125, 2003.

[106] J. Leach et. al. Interactive approach to optical tweezers control. *Applied Optics*, 45(5):897–903, 2006.

[107] V. Pelletier, N. Gal, P. Fournier, and M. L. Kilfoil. Microrheology of microtubule solutions and actin-microtubule composite networks. *Phys. Rev. Lett.*, 102:188303–188306, 2009.

[108] J. C. Crocker and D. G. Grier. Methods of digital microscopy for colloidal studies. *J. Colloid Interface Sci.*, 179:298–310, 1996.

[109] W. Thielicke and E. J. Stambuis. PIVlab - Towards user-friendly, affordable, and accurate digital particle image velocimetry in MATLAB. *J. Open Res. Software*, 2(1):e30, 2014.

[110] V. Barnett. *Interpreting Multivariate Data.* Wiley, 1981.

[111] M. Egeblad, M. G. Rasch, and V. M. Weaver. Dynamic interplay between the collagen scaffold and tumor evolution. *Curr. Opin. Cell Biol.*, 22:697, 2010.

[112] C. Frantz, K. M. Stewart, and V. M. Weaver. The extracellula matrix at a glance. *J. Cell Sci.*, 123:4195, 2010.

[113] P. Lu, V. M. Weaver, and Z. Werb. The extracellular matrix: A dynamic niche in cancer progression. *J. Cell Biology*, 196:395, 2012.

[114] J. P. Winer, S. Oake, and P. A. Janmey. Non-linear elasticity of extracellular matrices enables contractile cells to communicate local position and orientation. *PLoS ONE*, 4(7):e6382, 2009.

[115] T. Ebihara, N. Venkatesan, R. Tanaka, and M. S. Ludwig. Changes in extracellular matrix and tissue viscoelasticity in bleomycin-induced lung fibrosis. *Am. J. Respir. Crit. Care Med.*, 162:1569, 2000.

[116] O. Chaudhuri, L. Gu, M. Darnell, D. Klumpers, S. A. Bencherif, J. C. Weaver, N. Huebsch, and D. Mooney. Substrate stress relaxation regulates cell spreading. *Nat. Comm.*, 6(6365), 2015.

[117] J. Notbohm, A. Lesman, D. A. Tirrell, and G. Ravichandran. Quantifying cell-induced matrix deformation in three dimensions based on imaging matrix fibers. *Integr. Biol.*, 7:1186, 2015.

[118] J. Steinwachs, C. Metzner, K. Skodzek, N.Lang, I. Thievessen, C. Mark, S. Münster, K. E. Aifantis, and B. Fabry. Three-dimensional force microscopy of cells in biopolymer networks. *Nat. Methods*, 13:171, 2016.

[119] N. Gjorevski, A. S. Piotrowski, V. D. Varner, and C. M. Nelson. Dynamic tensile forces drive collective cell migration through three-dimensional extracellular matrices. *Scientific Reports*, 5:11458, 2015.

[120] S. Nam, J. Lee, D. G. Brownfield, and O. Chaudhuri. Viscoplasticity enables mechanical remodeling of matrix by cells. *Biophys. J.*, 111:2296, 2016.

[121] K. Yoo, L. R. Petzold, and R. T. Tranquillo. Rheology of reconstituted type I collagen gel in confined compression. *J. Rheol.*, 41:971, 1997.

[122] R. C. Arevalo, J. S. Urbach, and D. L. Blair. Size-dependent rheology of type-I collagen networks. *Biophys. J.*, 99(8):L65, 2010.

[123] X. Mao, O. Stenull, and T. C. Lubensky. Effective-medium theory of a filamentous triangular lattice. *Phys. Rev. E*, 87:042601, 2013.

[124] A. Sharma, A. J. Licup, K. A. Jansen, R. Rens, M. Sheinman, and G. H. Koenderink. Strain-controlled criticality governs the nonlinear mechanics of fibre networks. *Nat. Phys.*, 12:584, 2016.

[125] M. Sheu, J. Huang, G. Yeh, and H. Ho. Characterization of collagen gel solutions and collagen matrices for cell culture. *Biomaterials*, 22(13):1713–1719, 2001.

[126] B. Xu, H. Li, and Y. Zhang. Understanding the viscoelastic behavior of collagen matrices through relaxation time distribution spectrum. *Biomatter*, 3(3):e24651, 2013.

[127] E. R. Dufresne and D. G. Grier. Optical tweezer arrays and optical substrates created with diffractive optical elements. *Rev. Sci. Instr.*, 69:1974, 1998.

[128] D. G. Wallace and J. Rosenblatt. Collagen gel systems for sustained delivery and tissue engineering. *Advanced Drug Delivery Reviews*, 55(12), 2003.

[129] P. P. Provenzano, K. W. Eliceiri, J. M. Campbell, D. R. Inman, J. G. White, and P. J. Keely. Collagen reorganization at the tumor-stromal interface facilitates local invasion. *BMC Medicine*, 4(1):38, 2006.

[130] M. W. Conklin, J. C. Eickhoff, K. M. Riching, C. A. Pehlke, K. W. Eliceiri, P. P. Provenzano, A. Friedl, and P. J. Keely. Aligned collagen is a prognostic signature for survival in human breast carcinoma. *Am. J. Path.*, 178(3):1221, 2011.

[131] L. M. Sander. Modeling contact guidance and invasion by cancer cells. *Cancer research*, 74(17):4588–4596, 2014.

[132] R. De and S. Safran. Dynamical theory of active cellular response to external stress. *Physical Review E*, 78(3):031923, 2008.

[133] A. D. Doyle, N. Carvajal, A. Jin, K. Matsumoto, and K. M. Yamada. Local 3D matrix microenvironment regulates cell migration through spatiotemporal dynamics of contractility-dependent adhesions. *Nat. Comm.*, 6:8720, 2015.

[134] P. Friedl, J. Locker, E. Sahai, and J. E. Segall. Classifying collective cancer cell invasion. *Nat. Cell Biol.*, 14(7):777–783, 2012.

[135] J. Kim, C. A. R. Jones, N. Groves, and B. Sun. Three-dimensional reflectance traction microscopy. *PLoS ONE*, 11(6):e0156797, 2016.